

Maria Nikolayevna Drozdovskaya

# CO Emission in C-Type Shocks

Master Research Project (Minor), 5 July, 2011

Supervisors: Dr. Lars Kristensen, Dr. Ruud Visser,  
Professor Dr. Ewine van Dishoeck



Leiden Observatory, Leiden University

# 1. Introduction

## 1.1. Context and Motivation

Shock waves are common phenomena in the interstellar medium (ISM). Astrophysical environments feature different shock waves from the most gentle ones that just push the ambient gas without altering it in any way, to some of the most energetic events in the Universe, where molecules dissociate and their constituent atoms get fully ionized. Their origins are just as diverse, ranging from the interaction of the Earth's magnetic field with the solar wind (Burlaga et al. 2008), to molecular outflows during star formation (Bachiller & Tafalla 1998), to supernova blasts (McKee & Cowie 1975) and even to galaxies colliding with each other (Haas et al. 2005). Understanding and quantifying the detailed physics of heating and subsequent cooling mechanisms in shock waves requires sophisticated and complex models, even for the case of 1D shocks. A tremendous amount of work has gone into developing such models since the 1980s and the field has only grown since (Hartigan et al. 1987, Peredo et al. 1995, Flower & Pineau des Forêts 2003, Kristensen 2007).

CO is one of the most abundant molecules in the ISM after  $\text{H}_2$  with an  $\text{H}_2/\text{CO}$  ratio of  $10^4 - 10^5$ . As a result of its permanent dipole moment, CO has several rotational transitions in the submillimeter wavelength range accessible from ground-based telescopes. Furthermore, the CO chemistry in the ISM is much better understood than that of  $\text{H}_2\text{O}$ , for example. These are just some of the facts that make CO an excellent shock tracer.

The presence of shock waves has been established by observations of various transitions of CO. One case study is that of young stellar objects (YSOs). Tracing these objects in low- $J$  (up to  $J = 3 - 2$ ;  $E_{\text{up}} \approx 23$  K) CO emission, it was discovered that all young stars drive shock waves into their ambient medium, an effect that was not predicted by any theory of star formation at that time (Lada 1998, Snell et al. 1980). With the *Infrared Space Observatory* (ISO) CO lines ranging from  $J = 14 - 13$  ( $E_{\text{up}} \approx 403$  K) to  $J = 25 - 24$  ( $E_{\text{up}} \approx 1247$  K) were observed in nearby low-mass YSOs (see for example the review by van Dishoeck 2004). The currently operating *Herschel Space Observatory* has the *HIFI* instrument that is capable of resolving CO  $J = 16 - 15$  ( $E_{\text{up}} \approx 522$  K) and also the *PACS* instrument which is capable of detecting even CO  $J = 43 - 42$  ( $E_{\text{up}} \approx 3616$  K). This provides observers with coherent data sets spanning a range of more than two orders of magnitude in energy. A consequence is that the astronomical community has the desire to be able to interpret these observations. This is where the need for good shock models explaining the excitation arises, as well as the aspiration for a grid of shock models, so that the parameter space can be explored. The goal of this work is to make a first attempt at such an exploration by means of considering over 200 shocks, computed with the model of Flower & Pineau des Forêts (2003), and analyzing the corresponding CO emission, as calculated by LIME (Brinch & Hogerheijde 2010).

## 1.2. Molecular Recap

In this research  $^{12}\text{CO}$  and  $\text{H}_2$  are the key molecules under consideration, therefore some important facts about the two are mentioned here.

$\text{H}_2$  is the most common molecule in the ISM. It is a diatomic, homonuclear molecule. It does not possess a permanent dipole moment and its rovibrational transitions occur as electric quadrupole transitions. The total nuclear spin  $I$  of the molecule can be either 0 or 1, corresponding to antiparallel and parallel individual nuclear spins. From the Pauli Exclusion Principle it is known that the total wave function for two identical fermions must be antisymmetric. This implies that if  $I = 0$  (resp.  $I = 1$ ), then the total angular momentum quantum number  $J$  must be 0 or even (resp. odd), corresponding to para- $\text{H}_2$  (resp. ortho- $\text{H}_2$ ). These two distinctive flavors of  $\text{H}_2$  can only convert into one another via an exchange of nuclei, i.e. in chemical exchange reactions. The ratio of the ortho- to para- number densities is widely used and is denoted  $r_{op}$ . In cold molecular gas (of temperatures around 10 K)  $r_{op} \approx 0$  and in warmer molecular gas (temperatures greater than 300 K)  $r_{op} \approx 3$ .

CO is a likely candidate for the next most abundant molecule in the ISM. It is a diatomic, heteronuclear molecule. O is more electronegative than C and so CO possesses a permanent dipole moment. As a result the lowest rotational excitation levels of CO can be populated even at very moderate conditions (at densities lower than  $10^3 \text{ cm}^{-3}$  and temperatures below 300 K). On the other hand CO is very stable, thanks to the permanent dipole moment, which allows for rapid radiative stabilization, with a dissociation energy of 11.11 eV (Gaydon & Penney 1944), compared to  $\text{H}_2$  with a dissociation energy of 4.48 eV (Stoicheff 2001). Thus CO can be used to trace shocks. In fact, neither CO nor  $\text{H}_2$  have a direct photodissociation channel, which makes the two molecules hard to dissociate. CO photodissociates via predissociation upon photon absorption and  $\text{H}_2$  - through spontaneous radiative dissociation. Due to the high  $\text{H}_2$  abundance, it is the dominant coolant in a shock. However it requires a sufficiently high temperature of at least 100 K to undergo electric quadrupole transitions and actively cool. This is not only because electric quadrupole transitions must adhere to the  $\Delta J = 2$  selection rule, but also because  $\text{H}_2$  is light and its energy levels are widely spaced. At lower temperatures CO and  $\text{H}_2\text{O}$  are the dominant coolants.

## 1.3. Theoretical Background

A *rotational transition* of a molecule corresponds to a change in the total angular momentum quantum number  $J$ , i.e. a transition between two different rotational energy levels. Consider an ensemble of molecules and let  $n_i$ ,  $i \in \mathbb{Z}_{\geq 0}$  denote

the *level populations*, the number densities of molecules excited to a level  $i$ . Suppose the molecules are in thermodynamic equilibrium at an *excitation temperature*  $T_x$ , then the level populations are prescribed by the Boltzmann distribution:

$$n_i = \frac{n}{Q(T_x)} g_i e^{\frac{-E_i}{k_B T_x}}, \quad (1)$$

where  $n = \sum_{i=0}^{\infty} n_i$ ,  $Q(T_x)$  is the partition function,  $g_i$  is the degeneracy of level  $i$ ,  $E_i$  is the energy of level  $i$  and  $k_B$  is the Boltzmann constant. Many systems are not in thermodynamic equilibrium and the level populations cannot be described by a single  $T_x$ . Suppose the system is in statistical equilibrium though, then:

$$\frac{dn_i}{dt} = R_i + C_i = 0, \quad (2)$$

where  $\frac{d}{dt}$  is the time derivative,  $R_i$  is the rate of radiative transitions into/out of level  $i$  and  $C_i$  is the rate of collisional transitions into/out of level  $i$ . From the theory of radiative processes it is known that:

$$R_i = \sum_{\substack{j=0 \\ j \neq i}}^{\infty} [n_j A_{ji} + (n_j B_{ji} - n_i B_{ij}) \bar{J}_{ij}], \quad (3)$$

where  $A_{ji}$  is the Einstein coefficient for spontaneous emission,  $B_{ji}$  is the Einstein coefficient for stimulated emission,  $B_{ij}$  is the Einstein coefficient for stimulated absorption and  $\bar{J}_{ij}$  is the mean intensity at frequency  $\nu$  corresponding to the transition between level  $i$  and  $j$ . In equation 3 the spontaneous emission from level  $j$  to level  $i$  is taken into account (with  $j > i$ ), then the stimulated emission from level  $j$  to level  $i$  and finally, the absorption of photons from the radiative field leading to a transition from level  $i$  to level  $j$ . By definition:

$$\bar{J}_{ij} \equiv \int_0^{\infty} J_{\nu} \phi(\nu) d\nu, \quad (4)$$

where  $\phi(\nu)$  is the line profile function, which describes the finite width around the frequency  $\nu$ , where absorption can take place. It is taken to be normalized:

$$\int_0^{\infty} \phi(\nu) d\nu = 1. \quad (5)$$

Furthermore,  $J_{\nu}$  is the overall mean intensity, by definition:

$$J_{\nu} = \frac{1}{4\pi} \int I_{\nu} d\Omega, \quad (6)$$

where  $I_{\nu}$  is the specific intensity of the radiative field and  $d\Omega$  is a solid angle. The photon occupation number is defined as:

$$n_{\gamma} = \frac{I_{\nu}}{2h\nu^3/c^2} = \frac{1}{e^{h\nu/k_B T_r} - 1}, \quad (7)$$

where  $T_r$  is the *radiative temperature*, which characterizes the radiative field  $I_{\nu} = B_{\nu}(T_r)$  and:

$$B_{\nu}(T) = \frac{2h\nu^3/c^2}{e^{h\nu/k_B T} - 1} \quad (8)$$

is the Planck function.  $n_{\gamma}$  basically describes the number density of photons per unit of phase space. Two more useful equations are the Einstein relations:

$$g_i B_{ij} = g_j B_{ji}, \quad (9)$$

$$A_{ji} = \frac{2h\nu^3}{c^2} B_{ji}. \quad (10)$$

The reason all these definitions need to be presented is so that a more convenient form of equation 3 could be attained. Substituting equations 6 and 5 into equation 4 yields:

$$\frac{\bar{J}_{ij}}{I_{\nu}} = \frac{\int_0^{\infty} J_{\nu} \phi(\nu) d\nu}{I_{\nu}} = 1. \quad (11)$$

Now substituting equations 9, 10, 7 and 11 into equation 3 further yields:

$$\begin{aligned} R_i &= \sum_{\substack{j=0 \\ j \neq i}}^{\infty} \left[ n_j A_{ji} + \left( n_j \frac{c^2}{2h\nu^3} A_{ji} - n_i \frac{g_j}{g_i} \frac{c^2}{2h\nu^3} A_{ji} \right) \bar{J}_{ij} \right] \\ &= \sum_{\substack{j=0 \\ j \neq i}}^{\infty} n_j A_{ji} + n_{\gamma} \sum_{\substack{j=0 \\ j \neq i}}^{\infty} n_j A_{ji} - \frac{n_i}{g_i} n_{\gamma} \sum_{\substack{j=0 \\ j \neq i}}^{\infty} g_j A_{ji}. \end{aligned} \quad (12)$$

It is also known that:

$$C_i = \sum_{\substack{\text{collisional} \\ \text{partners}}} \sum_{\substack{j=0 \\ j \neq i}}^{\infty} n_c (n_j C_{ji} - n_i C_{ij}), \quad (13)$$

where  $n_c$  is the density of a collision partner,  $C_{ji}$  is the collisional de-excitation rate from level  $j$  to level  $i$  and  $C_{ij}$  is the collisional excitation rate from level  $i$  to level  $j$ . It is known that:

$$C_{ji} = \frac{g_j}{g_i} C_{ij} e^{-\Delta E/k_B T_{kin}}, \quad (14)$$

where  $T_{kin}$  is the *kinetic temperature* of a collision partner. Thus equation 13 can be written as follows:

$$C_i = \sum_{\substack{\text{collisional} \\ \text{partners}}} \sum_{\substack{j=0 \\ j \neq i}}^{\infty} n_c \left( n_j \frac{g_j}{g_i} e^{-\Delta E/k_B T_{kin}} - n_i \right) C_{ij}. \quad (15)$$

Combining equations 2, 12 and 13 yields:

$$\sum_{\substack{j=0 \\ j \neq i}}^{\infty} n_j A_{ji} + n_\gamma \sum_{\substack{j=0 \\ j \neq i}}^{\infty} n_j A_{ji} - \frac{n_i}{g_i} n_\gamma \sum_{\substack{j=0 \\ j \neq i}}^{\infty} g_j A_{ji} + \sum_{\substack{\text{collisional} \\ \text{partners}}} \sum_{\substack{j=0 \\ j \neq i}}^{\infty} n_c \left( n_j \frac{g_j}{g_i} e^{-\Delta E/k_B T_{kin}} - n_i \right) C_{ij} = 0. \quad (16)$$

Another important concept is that of *local thermal equilibrium* (LTE). Molecules are said to be in LTE if they are in thermal equilibrium with themselves (but not necessarily the radiative field). The Boltzmann distribution from equation 1 is still a valid description of the level populations in this case. The *critical density* for an upper level  $u$  is given by:

$$n_{u,crit} = \frac{\sum_{\substack{l=0 \\ l \leq u}}^{\infty} A_{ul}}{C_u}. \quad (17)$$

It compares the radiative transitions to all lower levels with the collisional rates to all levels. When the density is much larger than  $n_{u,crit}$ , collisions dominate the de-excitation process. The system tends to LTE in this case. It is known that for CO the relation  $A_{ul} \propto (J+1)^3$  holds, therefore the critical density increases rapidly for higher transitions. Typical values for CO are  $n_{1,crit} = 2.1 \cdot 10^3 \text{ cm}^{-3}$  for  $J = 1 - 0$  and  $n_{10,crit} = 6.1 \cdot 10^5 \text{ cm}^{-3}$  for  $J = 10 - 9$ , as can be calculated with the values from Neufeld (in prep.) for  $T = 500 \text{ K}$ . Meanwhile, for  $\text{H}_2$  the critical densities depend very weakly on transition and temperature. Typical values are  $10^2$ - $10^3 \text{ cm}^{-3}$  (Nisini 2008). For the range of shock parameters considered in this research it means that low- $J$  CO de-excitations will be mostly collisional and high- $J$  - mostly radiative, while those of  $\text{H}_2$  - mostly collisional for all transitions.

A *rotation diagram* is a plot of  $\ln\left(\frac{n_u}{g_u}\right)$  versus  $\frac{E_u}{k_B}$ , where the subscript  $u$  is used to denote the upper level of a transition. If one takes the natural logarithm of equation 1, then it becomes:

$$\ln\left(\frac{n_u}{g_u}\right) = \ln\left(\frac{n}{Q(T_x)}\right) - \frac{E_u}{k_B} \frac{1}{T_x}. \quad (18)$$

The above equation prescribes a straight line in a rotational diagram. Hence the rotation diagram for a system in LTE has the properties of its gradient being equal to  $\frac{1}{T_x}$  and its ordinate intercept being equal to  $\ln\left(\frac{n}{Q(T_x)}\right)$ .

#### 1.4. Shocks

Shock waves occur whenever material moves at velocities exceeding the sound velocity in the surrounding medium and the upstream material cannot dynamically respond to the upcoming material until it arrives. The shock then compresses, heats and accelerates the medium (Tielens 2010). A *shock wave*, or a *shock* for short, may be defined as any pressure driven disturbance, which is time independent (in a comoving reference frame, i.e. the reference frame, in which the shock is stationary) and which effects an irreversible change in the state of the medium (Draine 1980). A shock typically has a *shock front* - a very short distance, over which there is an abnormal pressure change, and a *relaxation layer* - a region following the shock front, over which the hydrodynamical variables come in equilibrium with the surrounding medium. Further structural specifics of a shock depend on its driving agent (Kristensen et al. 2008, Tielens 2010), such as that of a bow shock (Hollenbach 1997). It is also possible to speak of the *pre-shock material* and *post-shock material*, which lie respectively before and after the shock front.

In general, two types of shocks are distinguished, namely a J-type and a C-type. Consider the situation when there is no magnetic field present. In such a case the fluid is characterized by a single pressure, velocity and temperature. A shock propagating through such an environment causes a very sudden disturbance that can in principle be regarded as a discontinuity in the hydrodynamical variables characterizing the fluid. In such a case the shock front is much thinner than the relaxation layer. This is a *Jump-type* shock, or *J-type* for short.

Now consider the situation when there is a magnetic field present. In this case the charged fluids and the neutral fluid decouple, and each is characterized by its own pressure, velocity and temperature, depending on the charge of a particle. Charged particles couple to the magnetic field and gyrate around the magnetic field lines. Meanwhile neutral particles are not directly affected by the magnetic field and are only made aware of it via collisions with charged particles (assuming that the fractional ionization is sufficiently high). Under the action of a compressive wave, longitudinal magnetic fields compress and a J-type shock occurs. However if transverse magnetic fields are present surpassing a certain critical value, denoted  $B_{\text{crit}}$ , then a *Continuous-type* shock occurs, or *C-type* for short. As the name suggests, in this case the change in temperature, pressure and velocity is smooth. Below is the explanation of why this is the case.

For the purposes of this research multi-fluid environments are considered to be consisting of only neutral species and singly positively ionized species, from now on just simply referred to as ions. These are also the assumptions of the shock code used; however there the electrons are also taken into account. This is a fair assumption for typical shocks in the astronomical context too, since higher degrees of ionization generally require more immoderate conditions. In this context there are three relevant types of plasma waves with respective velocities. There is the sound speed prescribed by

$$c_s = \sqrt{\frac{\gamma k_B T}{\mu}}, \quad (19)$$

where  $\gamma$  is the heat capacity ratio,  $k_B$  is Boltzmann's constant,  $T$  is the temperature of the fluid and  $\mu$  is the mean molecular weight. The Alfvén velocity given by

$$v_A = \sqrt{\frac{B^2}{4\pi\rho}}, \quad (20)$$

where  $B$  is the transverse magnetic field strength and  $\rho$  is the density of the fluid. It describes the longitudinal oscillation of the ions in the magnetic field. Finally comes the magnetosonic velocity described by

$$v_{ims} = \sqrt{\frac{B^2}{4\pi\rho_i}}, \quad (21)$$

where  $\rho_i$  is the density of the ions. It describes the transverse oscillation of the ion in the magnetic field. Let the velocity of the shock front be denoted by  $v_s$ . By definition of a shock it is known that for both J-type and C-type shocks it must hold that  $v_s > c_s$ . This is the only constraint for the J-type, however there are more constraints on the C-type. Namely it must also hold that  $v_s > v_A(B_{\text{crit}})$ , if it were otherwise then the arrival of the shock front would be directly relayed to the neutrals and the fluid would only be pushed, not shocked. There is also a third constraint that C-type shocks must satisfy, that is  $v_s < v_{ims}$ . This condition implies that the magnetic field can begin to be compressed by the shock before the shock front arrives, hence ions are made aware of the shock ahead of the shock front and from the standpoint of ions there is no hydrodynamic surprise, which in turn warn the neutrals too, through collisions. This is what is known as a *magnetic precursor*, the key characteristic feature that makes C-type shocks continuous. In the comoving reference frame a C-type shock is always supersonic. The shock front of a C-type is thicker than that of a J-type.

The explicit formulations of shock physics are very complex. However the conservation of the main magnetohydrodynamic parameters can be expressed via the Rankine-Hugoniot equations, which state that

$$\rho_1 v_1 = \rho_2 v_2, \quad (22)$$

$$\rho_1 v_1^2 + P_1 + \frac{B_1^2}{8\pi} = \rho_2 v_2^2 + P_2 + \frac{B_2^2}{8\pi}, \quad (23)$$

$$\left( \rho_1 \frac{v_1^2}{2} + \frac{\gamma}{\gamma-1} P_1 + \frac{B_1^2}{4\pi} \right) v_1 = \left( \rho_2 \frac{v_2^2}{2} + \frac{\gamma}{\gamma-1} P_2 + \frac{B_2^2}{4\pi} \right) v_2, \quad (24)$$

where  $P$  denotes the pressure,  $v$  the velocity and  $T$  the temperature of the fluid, and subscripts 1, resp. 2, refer to the pre-, resp. post-shock, conditions (Guillet 2008). The three equations describe the conservation of mass, momentum and energy, respectively. Details are not presented here; instead one can refer to texts such as Hollenbach (1997), Tielens (2010), etc. for further details. One important formula, presented here without derivation that is useful later on is for the energy flux of the fluid entering the shock front per unit area and per unit time

$$E \approx \frac{1}{2} \rho v_s^3, \quad (25)$$

where  $\rho$  is the density of the fluid and where the internal energy of the fluid has been neglected.

Another important feature of shocks is stability. The passage of a C-type shock causes excitation of  $\text{H}_2$ , however if the shock is energetic enough, it may also cause dissociation of  $\text{H}_2$ . Due to its high abundance  $\text{H}_2$  is the dominant coolant in a shock and its dissociation leads to a rise in temperature. From equation 19 it can be seen that  $c_s \propto \sqrt{T}$ , thus an increase in temperature also causes an increase in the sound speed. This in turn leads to the initially supersonic shock to be transformed into a subsonic shock in the comoving reference frame. During such a transition the C-type collapses into a J-type. Such shocks are not considered in this research, yet their existence needs to be recognized.

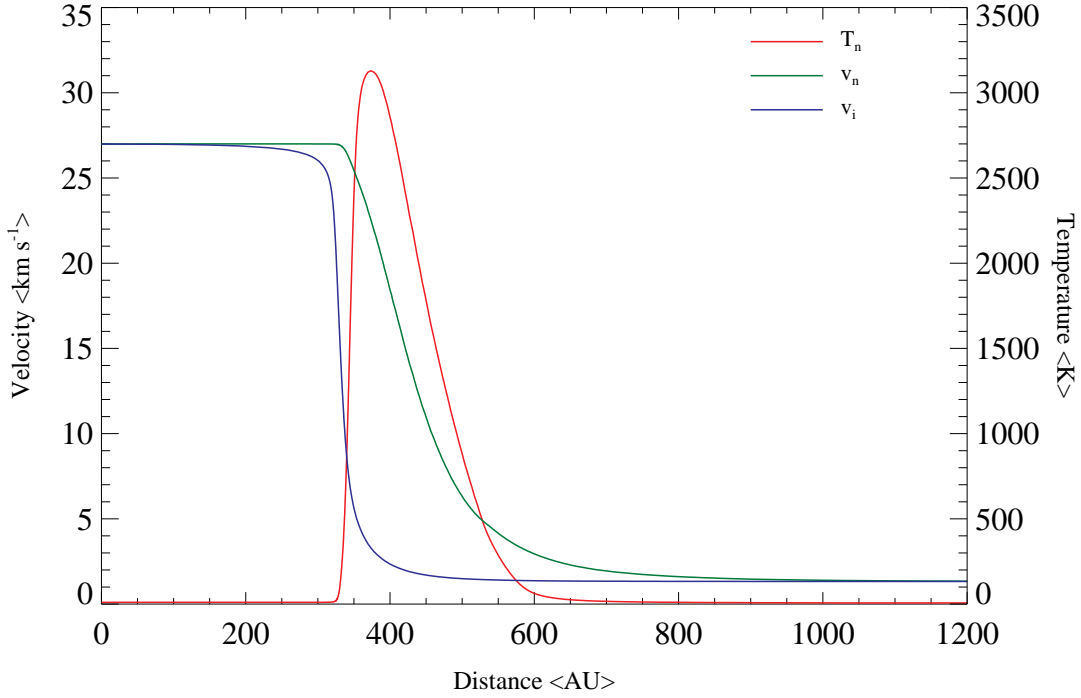


**Fig. 1.** The velocity profile, showing the changes in the velocity of neutrals (green), the velocity of ions (blue) and the temperature of neutrals (red) with the passage of a C-type shock with  $r_{op} = 3.0$ ,  $v_s = 27 \text{ km s}^{-1}$ ,  $n_H = 10^5 \text{ cm}^{-3}$  and  $b = 1.0$  as function of distance in the reference frame of the shock.

### 1.5. Shock Models

For this research the shock model of Flower and Pineau des Forêts (2003) has been used. As many other magnetohydrodynamic (MHD) shock models currently on the market, it assumes idealistic shocks that are steady (i.e.  $\partial/\partial t = 0$ ) and plane-parallel (i.e.  $\partial/\partial y = \partial/\partial z = 0$ ). The shock model integrates the equations describing the conservation of the magnetohydrodynamic parameters in parallel with the  $\text{H}_2$  level population rates. Furthermore, a large number of species and linking reactions are considered, as well as some grain physics. It is one of the few models taking the detailed chemical balance explicitly into account. The computations are performed in 1D in such a way that the post-shock material has been compressed by the shock front and remains compressed at a higher pressure than the pre-shock gas. In reality the post-shock gas would diffuse into the ambient medium in order to attain a pressure equilibrium. For C-type shocks the model causes the compression to remain for a much longer period of time, leading to a possible over-estimation of the post-shock densities and thus in turn emission.

There are five key parameters that differentiate the shocks, specifically: type (C or J),  $r_{op}$ ,  $v_s$ , the pre-shock number density of H,  $n_H$ , and the magnetic scaling factor  $b$ , which comes in through

$$B = b\sqrt{n_H <\text{cm}^{-3}>} <\mu\text{Gauss}>. \quad (26)$$

The original grid of models run by Kristensen (2007) consisted of around 25000 models with the following parameter space

- $r_{op} \in \{0.01, 1.0, 2.0, 3.0\}$ ,
- $v_s \in [10, 50] \text{ km s}^{-1}$  with a step-size of  $1 \text{ km s}^{-1}$ ,
- $n_H \in \{10^4, 5 \cdot 10^4, 10^5, 5 \cdot 10^5, 10^6, 5 \cdot 10^6, 10^7\} \text{ cm}^{-3}$ ,
- J-type shocks with  $b \in \{0, 0.1\}$ ,
- C-type shocks with  $b \in [0.5, 10]$  with a step-size of 0.5.

These particular ranges were taken in order to be representative of Orion Molecular Cloud 1 (Kristensen 2007). In this research only C-type shocks with  $r_{op} = 3.0$  and  $b = 1.0$  were considered from the above grid of models, which adds up to more than 200 models.

The output of the MHD simulation by Flower and Pineau des Forêts (2003) contains a large amount of physical data along the entire extent of a shock. The key parameters of interest here are the velocities of neutrals and ions,  $v_n$  and  $v_i$  respectively, the temperature of neutrals,  $T_n$ , fractional abundance of CO with respect to  $\text{H}_2$ ,  $2 \cdot x(\text{CO})$  (where  $x(\text{CO})$  is the fractional abundance of CO with respect to H) and the density of  $\text{H}_2$ ,  $n_{\text{H}_2}$  (which equals  $x(\text{H}_2) \cdot n_H$ , where  $x(\text{H}_2)$  is the fractional abundance of  $\text{H}_2$  with respect to H). In Appendix A the way of extracting these data from the output is explained in detail. In Fig. 1 through 3 these three profiles are depicted with the  $T_n$  profile present in all for reference and

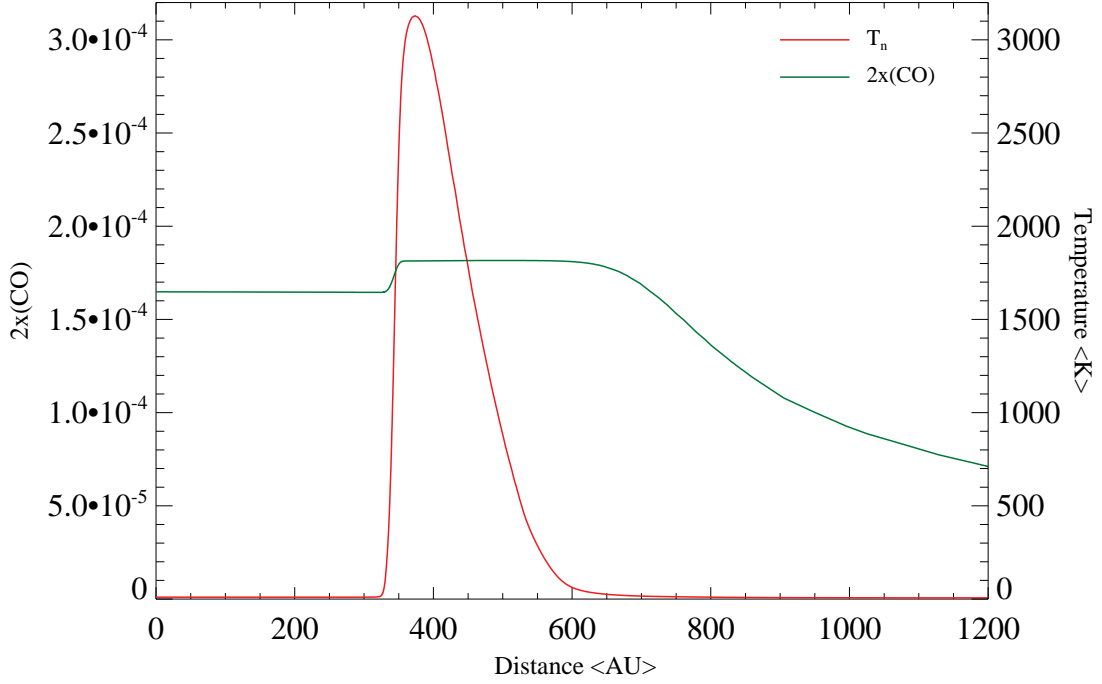


**Fig. 2.** The fractional abundance profile of CO, showing the changes in the fractional abundance of CO with respect to H<sub>2</sub>,  $2 \cdot x(\text{CO})$  (where  $x(\text{CO})$  is the fractional abundance of CO with respect to H) (green) and the temperature of neutrals (red) with the passage of a C-type shock with  $r_{op} = 3.0$ ,  $v_s = 27 \text{ km s}^{-1}$ ,  $n_H = 10^5 \text{ cm}^{-3}$  and  $b = 1.0$  as function of distance in the reference frame of the shock.

due to its defining nature in a shock, for the C type shock with  $r_{op} = 3.0$ ,  $v_s = 27 \text{ km s}^{-1}$ ,  $n_H = 10^5 \text{ cm}^{-3}$  and  $b = 1.0$ . The velocity profile shows that both neutrals and ions decelerate from the velocity of the shock front of  $27 \text{ km s}^{-1}$  down to a very low velocity. However this deceleration happens at different moments and at different rates, since the shock causes the two fluids to decouple. First the velocity of the ions starts to decrease, since they have been warned about the arrival of the shock by the magnetic precursor, this is also why the velocity decreases significantly prior to the reaching of the peak temperature. Only afterwards does the velocity of the neutrals starts to decrease, since they are only made aware of the shock via collisions with the ions and this process is not instantaneous. Furthermore, the changes in velocity and in temperature are all smooth, indicating that this is indeed a C-type shock. The fractional abundance profile of CO shows that the pre-shock value increases with the passage of the shock front and then decreases in the relaxation layer to a significantly lower value than the pre-shock one. The significant decrease is due to freeze-out of CO, i.e. it gets stuck on the dust grains, forms ice and remains there. The density profile of H<sub>2</sub> is the reflection of the first Rankine-Hugoniot equation 22. According to that equation  $\rho_2 = \frac{\rho_1 v_1}{v_2}$  and from the decrease observed in  $v_n$  in Fig. 1 with the passage of the shock, it becomes clear why the increase in the density of H<sub>2</sub> is observed. In a C-type shock  $T$  spans almost three orders of magnitude,  $n$  - at least one and a J-type shock could span even larger ranges. Therefore when modeling the radiation emitted by a shock, a code must be chosen that can cover such a dynamic range of  $T$  and  $n$ , which implies a big range of values for the individual level populations of CO, which in turn must be treated very careful in the computation.

### 1.6. LIME

The Line Modeling Engine (LIME, Brinch & Hogerheijde 2010) is an excitation and radiation transfer code that predicts line and continuum radiation from an astronomical source model. Version 1.01 has been used in this research. The inner workings of LIME can be summarized briefly in the following steps:

1. LIME generates a computational domain, a sphere, of a certain radius that the user specifies.
2. A user-specified number of grid points is distributed randomly through the computational domain, weighted by a source model dependent function.
3. The Delaunay triangulation of these grid points is constructed.
4. The Delaunay triangulation is smoothed by means of Lloyds algorithm. Essentially, each grid point (Voronoi point) is iteratively moved towards the center of mass of its Voronoi cell.
5. The radiation field is obtained by the propagation of photons along the boundaries of Delaunay cells. Using the resulting radiation field, a minor iteration loop is executed, where a set of linear equations, determining the statistical equilibrium, are iterated upon in order to converge to a set of level populations.

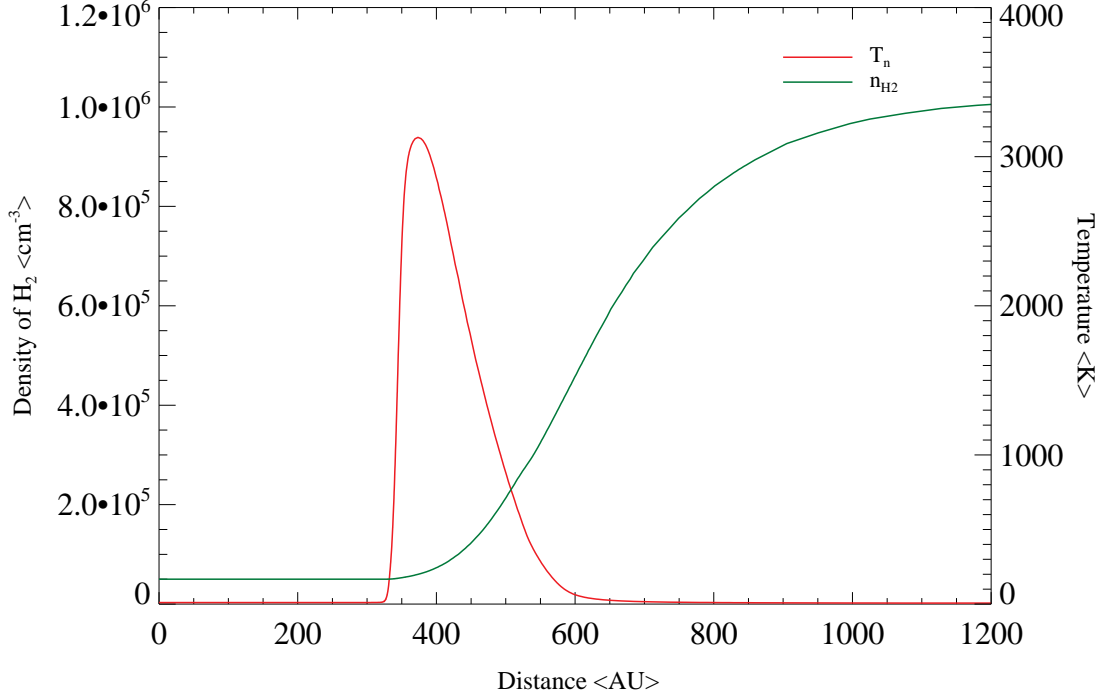


**Fig. 3.** The density profile of  $H_2$ , showing the changes in the density of  $H_2$ ,  $n_{H_2}$  (green) and the temperature of neutrals (red) with the passage of a C-type shock with  $r_{op} = 3.0$ ,  $v_s = 27 \text{ km s}^{-1}$ ,  $n_H = 10^5 \text{ cm}^{-3}$  and  $b = 1.0$  as function of distance in the reference frame of the shock.

6. This is repeated a fixed number of times to ensure convergence and the signal to noise ratio (SNR) is displayed to quantify it.
7. Ray-tracing of the lines of sight through the model is done, in order to obtain a square image of the radiation that escapes from the surface.

A number of parameters are user specified here, e.g. source distance, velocity, orientation, image resolution, etc. The photons are allowed to move in straight lines through the Voronoi tessellation of the grid points during ray-tracing. Each Voronoi cell is assigned the level populations of its associated grid point, but the velocity varies smoothly across each cell. This is why the stepping through the source model is done in small step sizes, which are a fraction of the cell size.

The input of LIME consists of a large number of parameters, some mandatory, some optional and some semi-optional. Almost all of them are specified in a single input file. The parameters are described in detail in Appendix A with the direct application to the shock models and the basic idea of the setup is presented in Section 2.1.

The output of LIME consists of three different types of files. Firstly, is a formatted ASCII file containing the  $(x, y, z)$  coordinates of each grid point. Secondly, is a file, which contains the  $(x, y, z)$  coordinate of each grid point alongside the associated  $H_2$  density, kinetic gas density, molecular density and level populations (with respect to  $H_2$  density). Thirdly, is the main output of LIME, the FITS files containing the image cubes on a velocity scale. For further details refer to Brinch & Hogerheijde (2010) and Brinch (2011).

The design of LIME is such that it mimics any arbitrary distribution in a realistic manner thanks to the properties of Delaunay triangulations. It performs the computation in 3D and the level populations are calculated carefully. For these reasons LIME is appropriate for processing of shock model results. In Section 4 the LIME results are compared to the output of a 1D Large Velocity Gradient (LVG) code, which has more inherent assumptions and simplifications than LIME.

## 2. Methods

### 2.1. Applied

In this section the basics of setting up LIME in order to process the shock models are discussed. Cartesian coordinates are used here. The idea is to treat shocks as face-on infinite slabs. The most practical way to achieve this is to place a cylinder containing all the data points of the shock into the spherical computational domain of LIME. There is a reason that it is necessary to specify a cylinder rather than use the whole spherical computational domain of LIME. The assumption is made that a shock is a 1D object, aligned (arbitrarily) along the  $z$  axis. In order to smooth out some of LIME's inherent randomness, different lines of sight need to be probed through the shock, and thus the shock needs to be extended in the  $x$  and  $y$  directions. It is also desirable to have all lines probe the entire length of the shock. That is a



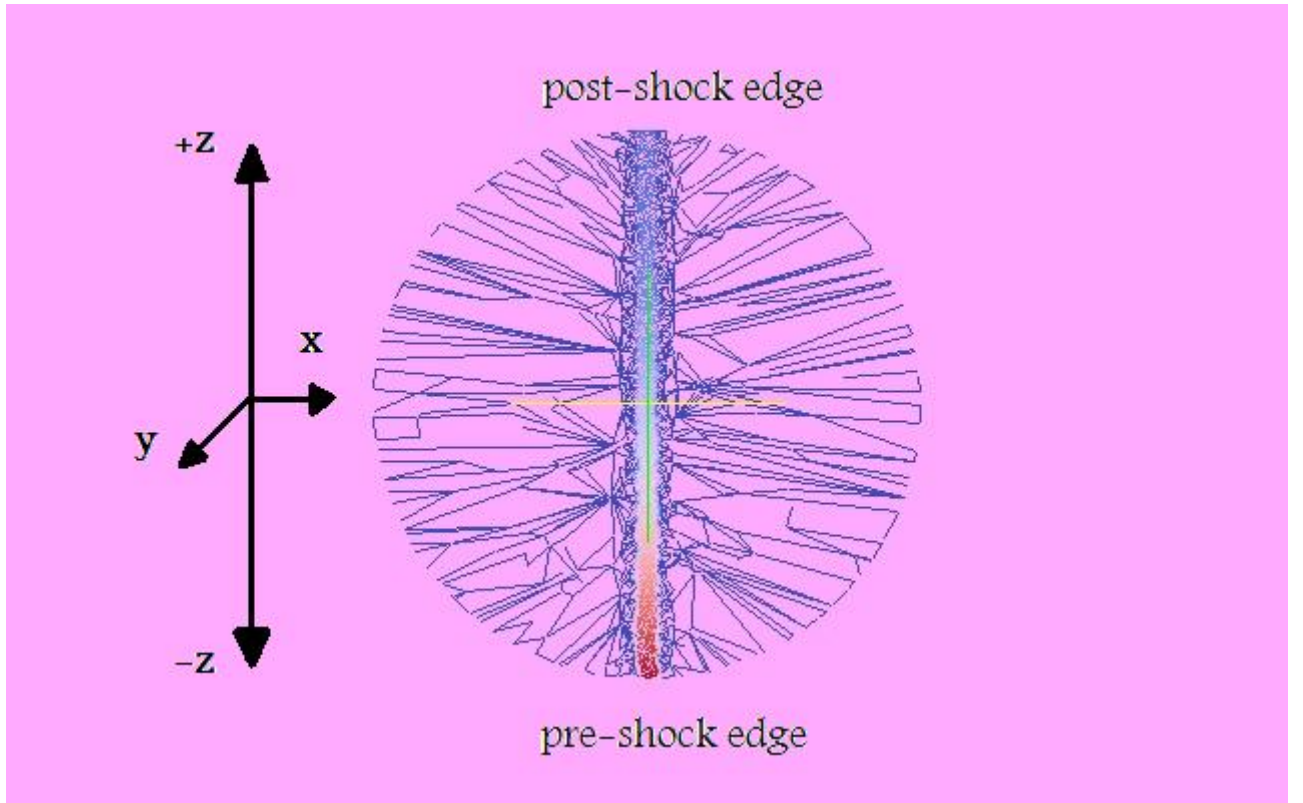


**Fig. 4.** A slice through the spherical computational domain of LIME and the inscribed cylinder containing the shock data points. The slice is made along the length of the cylinder, so along the extent of the shock. The red indicates a higher density of grid points, meanwhile the blue indicates a lower density. The lines are the borders of the Delaunay tessellation. This visualization is for the C-type shock with  $r_{op} = 3.0$ ,  $v_s = 27 \text{ km s}^{-1}$ ,  $n_H = 10^5 \text{ cm}^{-3}$  and  $b = 1.0$ .

means of achieving an infinite or semi-infinite slab. The thickness of the slab corresponds to the length of the shock, and the cross-sectional area of the slab is whatever is necessary to have sufficient lines of sight. If the whole sphere was filled with shock data, then the lines of sight would be of different length. In the cylinder setup they all have the same length. Every image cube generated contains  $11^2$  pixels.

The dimensions of the cylinder need to depend on the specific shock model under investigation. Its positioning is such that it is aligned along the  $z$  axis and its circular cross-sectional areas are in the  $xy$  plane. In Fig. 4 the situation is visualized by means a slice through the computational domain along the length of the cylinder. The collisional rates from Neufeld (in prep.), extrapolated to  $J = 80$  from Yang et al. (2010), which are made available on Leiden Atomic and Molecular Database (LAMDA) (Schöier et al. 2005), are used here. From the collisional rates for CO with para- and ortho-  $\text{H}_2$  quoted there, it can be seen that the two rates do not differ by much and therefore it is safe to treat the situation as if there is only one collisional partner, here all  $\text{H}_2$  was treated as para- $\text{H}_2$ . All other collisional partners can be neglected due to their low abundances. Dust is present in the computations and here the data file from Ossenkopf & Henning (1994) for dust with thin ice mantles with a gas density of  $10^6 \text{ cm}^{-3}$  is used.

LIME requires four physical parameters to be provided from the shock models: the density of  $\text{H}_2$ , the temperature of the neutrals, the fractional abundance of CO with respect to  $\text{H}_2$  and the velocity of the neutrals. There is also a Doppler broadening of  $1 \text{ km s}^{-1}$  present for all models. The sampling of the random grid points is done according to temperature. This ensures that most grid points are near the temperature peak that occurs in a shock (Fig. 1). Hence the location, where the major changes occur, is sampled very well.

## 2.2. Additional Considerations

In this section some additional considerations are discussed that are related to running LIME on shock models. These include the truncation, the shifting, the number of grid points and the averaging.

### 2.2.1. Truncation

In the grid models by Kristensen (2007) the shock is allowed to evolve to a dynamical age of  $10^8$  years, which leads to the over-estimation of pressure mentioned in Section 1.5. As a result the column density of cold post-shock gas will dominate emission. Hence it is necessary to truncate the shock model data. Here a constant truncation temperature is used for all models, specifically  $T_{trunc} = 25 \text{ K}$ . This means that all corresponding data points before the temperature of

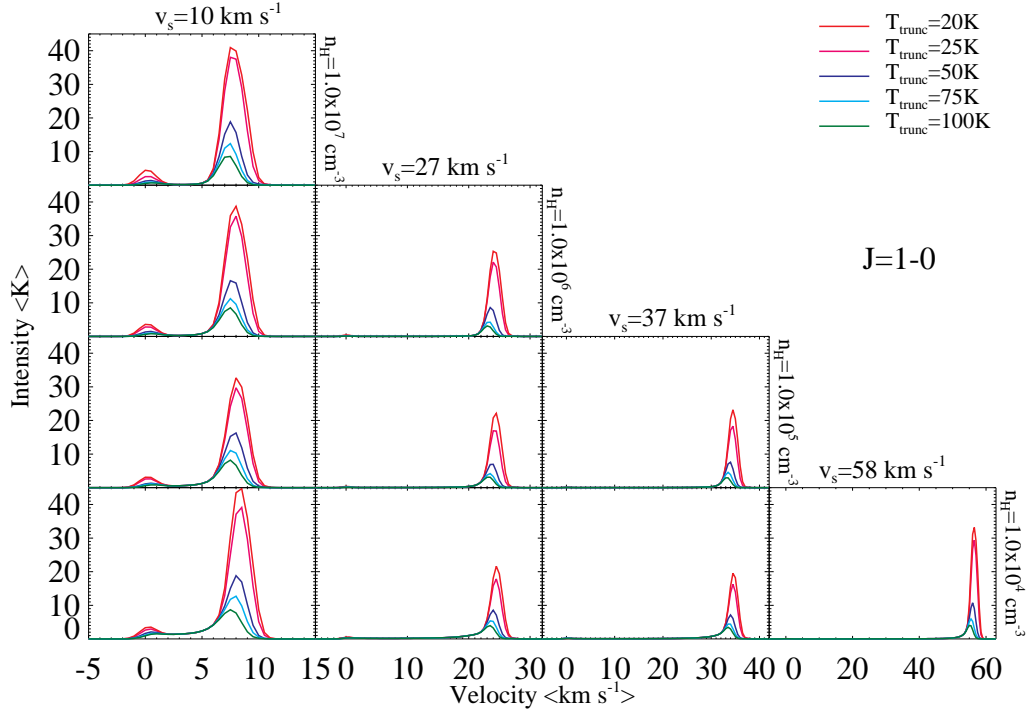


**Fig. 5.** The  $J = 1 - 0$  line profiles for ten representative shock models truncated at five different temperatures.

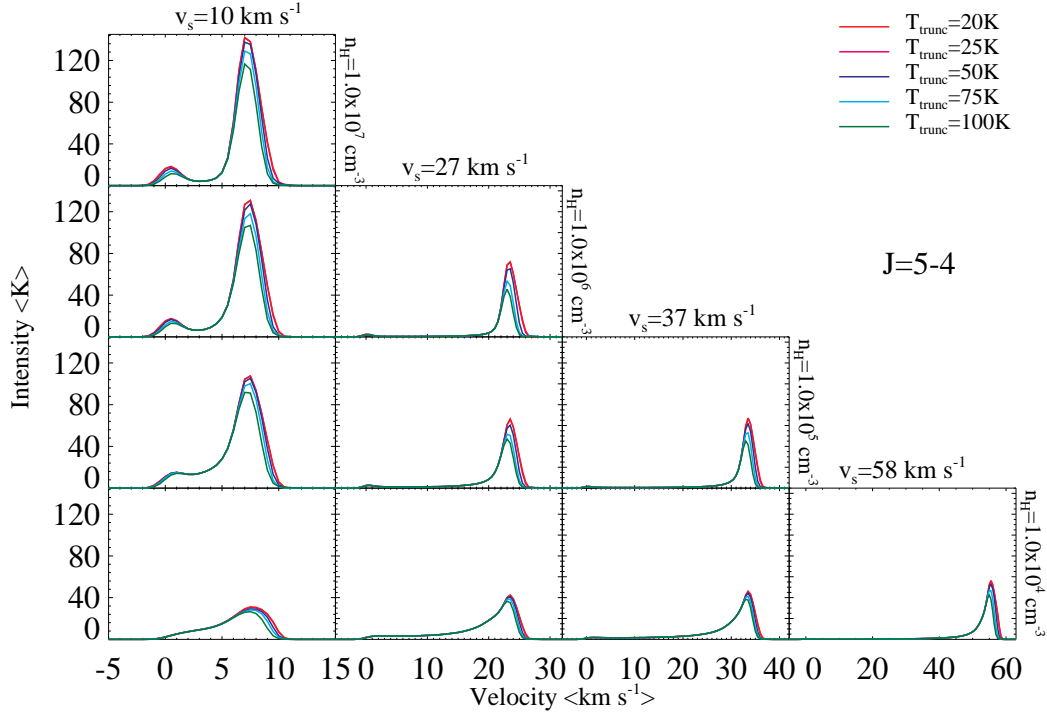


**Fig. 6.** The  $J = 5 - 4$  line profiles for ten representative shock models truncated at five different temperatures.

neutrals reaches 25 K are ignored and all those after the temperature of neutrals falls below 25 K. Otherwise a significant over-estimation could be included in the emission (especially in the lower transitions).

The interest lies in the shock itself, rather than the pre- and post-shock gases. The dust temperature is set to a constant 15 K in the LIME input file for all models. The shock model does not compute the temperature of the dust, thus this is appropriate for the LIME setup. It is known that downstream the shocked material in the form of post-shock gas always comes to an equilibrium with the dust, because the dust acts as an infinite heat reservoir. Taking into account

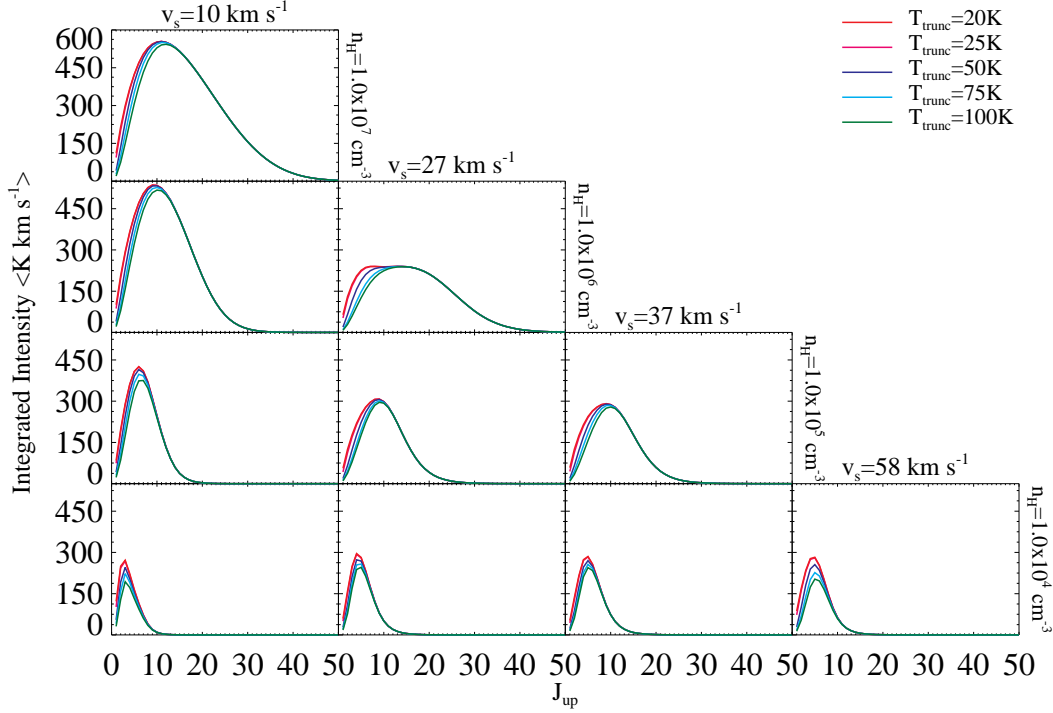


**Fig. 7.** The CO ladders for ten representative shock models truncated at five different temperatures.

that C-type shocks have maximum temperatures reaching several thousand Kelvin, it is reasonable to truncate at 25 K. This in turn must be done from both sides, to exclude the pre-shock gas too. Truncation is performed upon the temperature of neutrals, since here CO, a neutral molecule, is considered. In reality, when a shock is observed some amount of pre- and post-shock gas is observed too. Truncating at any temperature is an arbitrary choice. However this has also been performed by others in the past, including Flower and Pineau des Forêts (2010).

The effect of the choice of the truncation temperature has been analyzed for ten representative models in Fig. 5 for the  $J = 1 - 0$  transition. From this figure it is seen that the truncation temperature does not influence the shape of the profile. It only influences the total amount of the emission in the  $J = 1 - 0$  transition and hence the maxima attained. The greatest difference is between 25 K and 50 K truncation temperatures. The difference between 20 K and 25 K is not so large. Hence by truncating some emission is lost, however a truncation temperature of 25 K does not result in too large of a loss, approximately 5 – 10% for any of the ten models shown. In Fig. 6 the effect of the choice of the truncation temperature is visualized for the same ten models for the  $J = 5 - 4$  transition. From this figure it is seen that the truncation temperature barely influences the  $J = 5 - 4$  emission. The shape of the profiles is unaltered by it just like for  $J = 1 - 0$ . The total amount of emission and the peak value attained are only affected by approximately 5% at most if the data are truncated at 100 K (the C type shock with  $r_{op} = 3.0$ ,  $v_s = 10 \text{ km s}^{-1}$ ,  $n_H = 10^7 \text{ cm}^{-3}$  and  $b = 1.0$  being this worst case scenario). Therefore truncation at 25 K results in minimal loss in the  $J = 5 - 4$  transition. The difference between the effects of the truncation temperature in Fig. 5 and Fig. 6 is due to the fact that lower  $J$  levels are mostly populated at lower temperatures, so when truncation at 25 K is performed, only the few lowest  $J$  levels are affected significantly. This is further visualized in Fig. 7 where the CO ladders for the same ten models are depicted. For levels higher than  $J = 12$ , the ladders for different truncation temperatures are essentially indistinguishable for all the models due to the explanation just provided. The ladders corresponding to 20 K and 25 K truncation temperatures are essentially identical for all levels. For these reasons it can be concluded that truncation at 25 K is a safe choice to make.

### 2.2.2. Shifting

The data are shifted (and hence the cylinder) along the  $z$  axis, such that it is positioned symmetrically about the origin. For example, suppose that the shock model data extend from 1000 AU to 5000 AU, then the shifted shock model data extend from –2000 AU to 2000 AU. This can generically be calculated with the following simple formula:

$$z_{\text{shifted}} = z_{\text{original}} - 0.5 \left( z_{\text{original}} [\text{1st value}] + z_{\text{original}} [\text{last value}] \right). \quad (27)$$

There is also a good reason for doing this. If the shift is not performed, then an “artificial feature” appears. This is illustrated in Fig. 8 for the C-type shock model with  $r_{op} = 3.0$ ,  $v_s = 20 \text{ km s}^{-1}$ ,  $n_H = 10^4 \text{ cm}^{-3}$  and  $b = 1.0$ . In Fig. 8 the  $J = 1 - 0$  line profiles of this shock are plotted in five different pixels. Around  $20 \text{ km s}^{-1}$  an additional peak is observed for the non-shifted data. This peak is strongest towards the central pixel. Upon averaging over  $7^2$  pixels the contribution

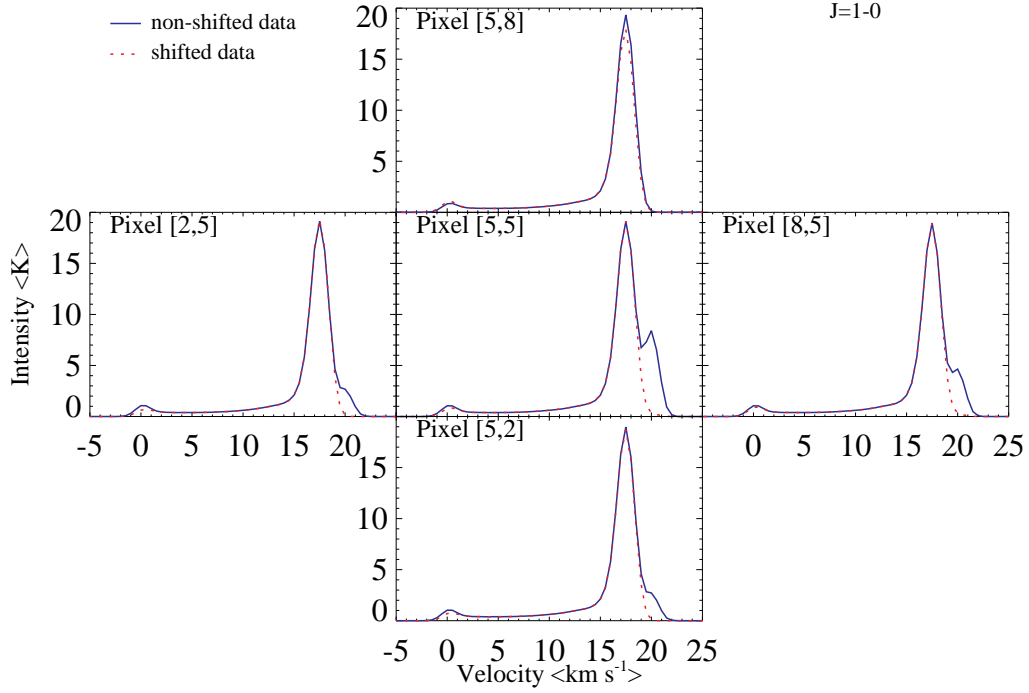


**Fig. 8.** The  $J = 1 - 0$  line profile for the C-type shock model with  $r_{op} = 3.0$ ,  $v_s = 20 \text{ km s}^{-1}$ ,  $n_H = 10^4 \text{ cm}^{-3}$  and  $b = 1.0$  in five different pixels.

of the “artificial feature” becomes even smaller, nevertheless its presence is undesirable. The effect is also diminished by increasing the number of grid points. The default value used in all other figures of this section is 3000 interior points and 2000 sink points (see the next section). Furthermore, the effect is less prominent for higher transitions. In Fig. 9 the

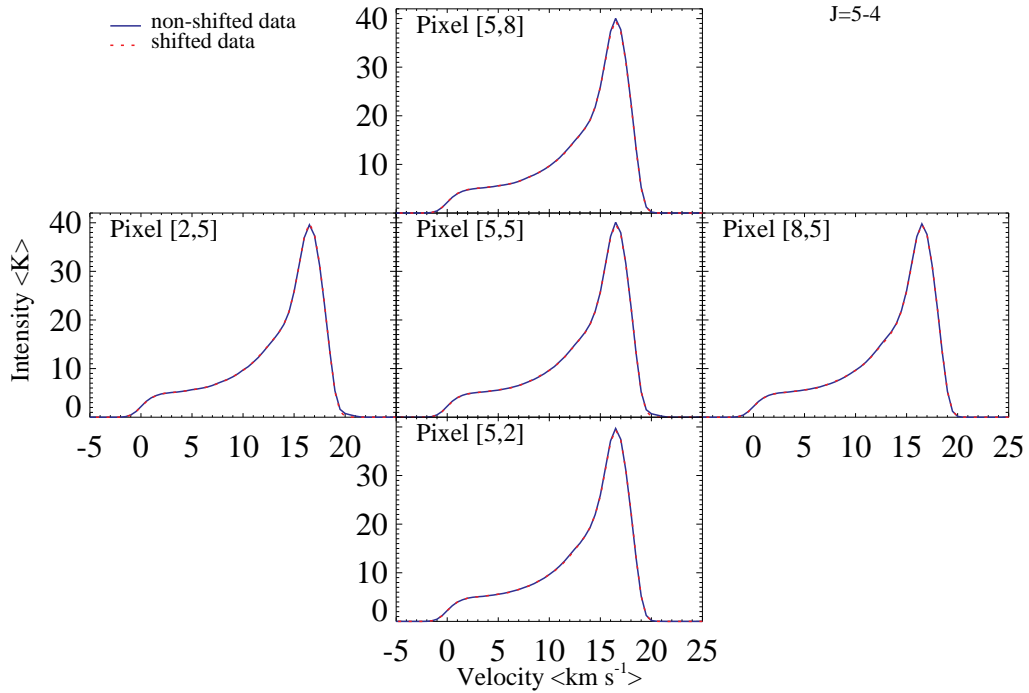


**Fig. 9.** The  $J = 5 - 4$  line profile for the C-type shock model with  $r_{op} = 3.0$ ,  $v_s = 20 \text{ km s}^{-1}$ ,  $n_H = 10^4 \text{ cm}^{-3}$  and  $b = 1.0$  in five different pixels.

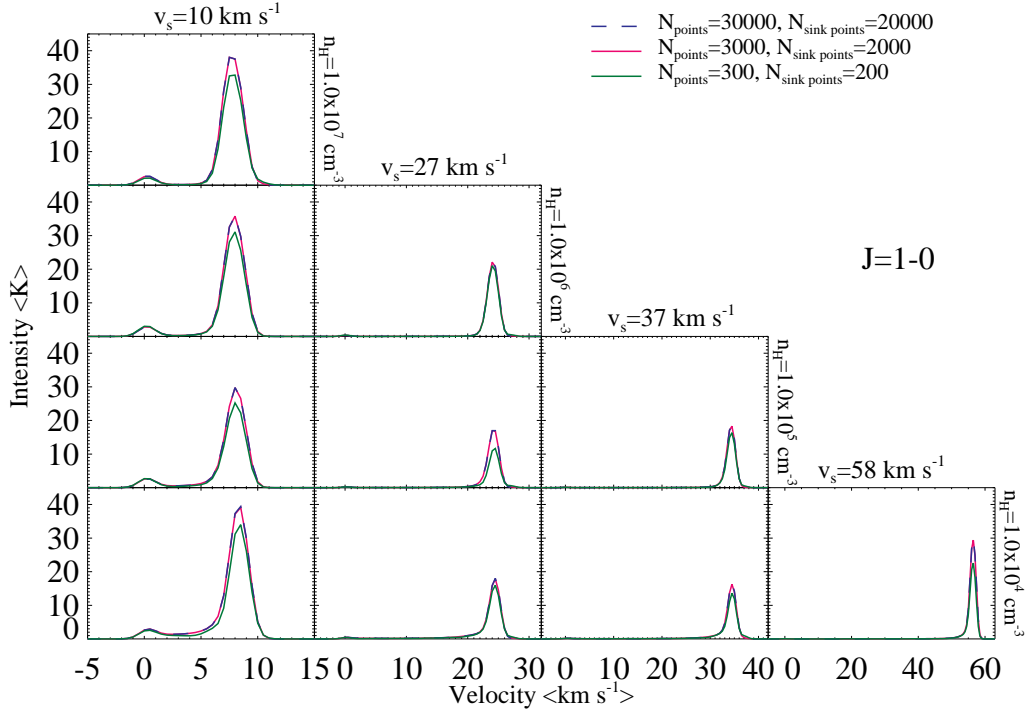


**Fig. 10.** The  $J = 1 - 0$  line profiles for ten representative shock models for three different sets of grid points.

$J = 5 - 4$  line profiles of this shock are plotted in five different pixels. The non-shifted and shifted data sets are essentially indistinguishable for the whole velocity domain. The same observation persists for the averaged case (over  $7^2$  pixels).

The “artificial feature” is an edge effect of LIME. Around the circular boundary of the cylinder at the pre-shock edge there are some Voronoi cells that lie partially inside and partially outside of the cylinder. Every such cell has a constant density determined by the location of the center of the cell. If the center lies inside the cylinder, it gets the density from the shock at that  $z$  value; if the center lies outside, it gets zero density. However, the velocity is not constant across the cell. This is because LIME splits each cell up into smaller pieces when it does the ray-tracing. Consider one of these edge cells at the pre-shock end of the cylinder, with the center just inside. The density of the entire cell is set to the pre-shock density. In the ray-tracing, the part of the cell that lies inside the cylinder gets the pre-shock velocity ( $20 \text{ km s}^{-1}$  in the reference frame of the shock), and the part that lies outside gets a velocity of  $0 \text{ km s}^{-1}$ . In the plots these are transformed to the reference frame of the observer, so the inside part gets  $v = 0 \text{ km s}^{-1}$  and the outside part gets  $v = 20 \text{ km s}^{-1}$ . The latter shows up in the spectrum at  $20 \text{ km s}^{-1}$ . Note that such “bad” Voronoi cells are present along the whole surface of the cylinder. However the ones at the post-shock edge circular boundary lie just outside the spherical computational domain and are thus in fact non-existent. As for the remaining boundary, these cells are excluded from the image from the way the pixels are defined, see Appendix A for justification.

### 2.2.3. Number of Grid Points

By design LIME has a certain degree of randomness. The primary means of getting a hold on this randomness is by increasing the number of grid points used. This would always imply a better sampling. It is possible to increase the number of grid points in the interior of the sphere and/or the number of grid points on the surface of the sphere, so-called sink points. The two values should in principle be kept in balance with one another, it means then that when increasing the number of grid points both of these values need to be increased. However the more grid points there are, the longer the computation takes. Yet again there needs to be a healthy balance between the two factors, so that the results are reliable and yet the computation takes a realistic amount of time. Here 3000 and 2000 points, respectively, have been used for the two parameters. The justification can be seen from the following plots. In Fig. 10 the  $J = 1 - 0$  line profiles for ten representative shock models for three different sets of grid points are shown. For some models there is little difference between the three sets of grid points, such as the two with  $v_s = 37 \text{ km s}^{-1}$ . However for most other ones emission corresponding to the set with the lowest number of grid points, namely  $N_{\text{points}} = 300$  and  $N_{\text{sinkpoints}} = 200$ , tends to be underrepresented by at most 10%. Meanwhile the other two sets are indistinguishable. The underestimation by the smallest set of grid points adds up over all the transitions and results in very large discrepancies between the CO ladders in Fig. 11. The two larger sets of grid points coincide fully. It can be seen that the underestimation by the smallest set is worst for transitions corresponding to the peaks of the ladders, so the  $J = 1 - 0$  case presented in Fig. 10 is far from the worst case scenario. Based on these figures, the smaller set of grid points must be rejected. LIME runs with the largest set of grid points take 12 hours on average and approximately 24 hours in a worst case scenario, depending on the

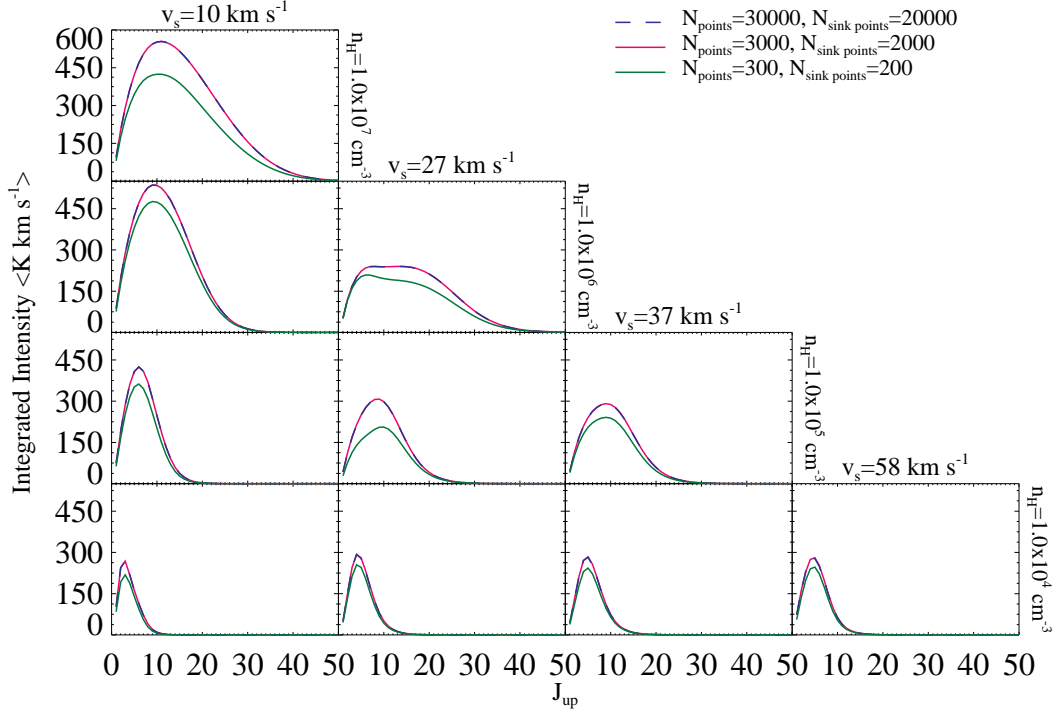


**Fig. 11.** The CO ladders for ten representative shock models for three different sets of grid points.

specific shock model. LIME runs with the intermediate set of grid points take 30 minutes in average and approximately 1 hour in a worst case scenario. Taking into account that over 200 shock models need to be computed and the results with the intermediate set of grid points do not differ in any significant way from the results attained with the largest set of grid points,  $N_{\text{points}} = 3000$  and  $N_{\text{sink points}} = 2000$  is used in this research for all models.

#### 2.2.4. Averaging

Lastly, the need for  $11^2$  pixels should be explained. It was stated above that LIME has inherent randomness and even though it can be controlled by the number of grid points, it can never be fully eliminated. This randomness may manifest itself by means of varying spectra across the pixels. Overall the spectra in each individual pixel are expected to be quite similar, however details may vary from pixel to pixel. The solution to this lies with averaging over all the available pixels to gain the most “truthful” spectrum. Here  $7^2$  pixels was deemed a sufficient number and the justification can be observed from the following plots. In Fig. 12 the  $J = 1 - 0$  emission is plotted for the C-type shock model with  $r_{op} = 3.0$ ,  $v_s = 27$  km s $^{-1}$ ,  $n_H = 10^5$  cm $^{-3}$  and  $b = 1.0$ . In the figure the emission is plotted for the central pixel and then averaged over  $3^2$ ,  $7^2$  and  $11^2$  pixels. It can be seen that the averaging over  $3^2$  and  $7^2$  pixels are indistinguishable and are both very similar to the central pixel. Meanwhile the averaging over  $11^2$  seems to underestimate the emission by around 1%. As stated above, emission from individual pixels is expected to vary, therefore it is not surprising that the averages do not match the central pixels fully. The idea is to average over as many pixels as possible to diminish the pixel to pixel variations. However averaging over all pixels, which is  $11^2$  here, is also not a good idea. Since the image square is almost perfectly inscribed into the circular cross-sections of the cylinder, the corner four pixels may be influenced by edge effects similar to those that caused the “artificial feature”. Furthermore, since the half-length of the cylinder is equal to the radius of the sphere, parts of the cylinder stick out of the spherical computational domain. As a result, some pixels will not contain any data points. These are the reasons why averaging over all  $11^2$  pixels actually produces a lower emission. For these reasons averaging is performed over  $7^2$  pixels in this research (while the total number of pixels is kept at a constant  $11^2$  for all models).

#### 2.2.5. Collisional Rate Coefficients

An essential input file for LIME and any other radiation transfer code, is the molecular data file containing the collisional rate coefficients for the molecule under consideration and its collisional partners. There are a number of such calculations available in the literature. In Fig. 14 three CO ladders for the C-type shock model with  $r_{op} = 3.0$ ,  $v_s = 27$  km s $^{-1}$ ,  $n_H = 10^5$  cm $^{-3}$  and  $b = 1.0$  with a logarithmic scale along the ordinate are shown, as computed with three different CO data files. The Neufeld (in prep.) data file is the one used for all of the results in this research, unless otherwise stated. An older version of this file is also considered (Neufeld in prep., old) and the much older 40 transition data file from

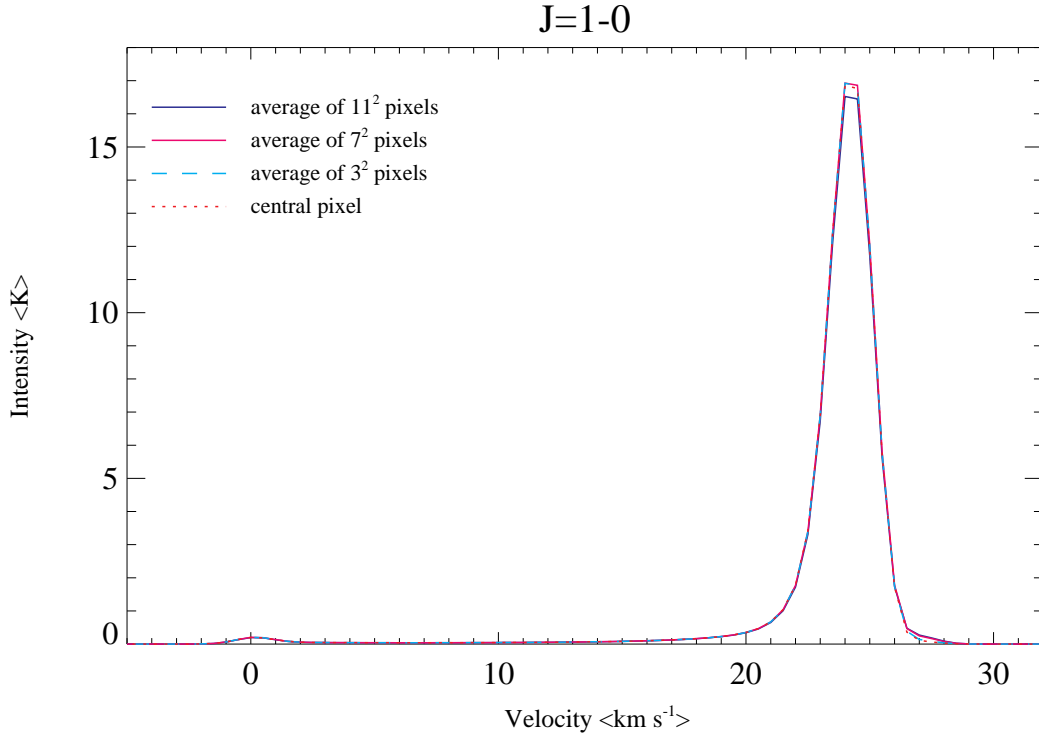


**Fig. 12.** The  $J = 1 - 0$  line profile for the C-type shock model with  $r_{op} = 3.0$ ,  $v_s = 27 \text{ km s}^{-1}$ ,  $n_H = 10^5 \text{ cm}^{-3}$  and  $b = 1.0$  for four different pixel selections.

Flower (2001) and Wernli et al. (2006), extrapolated up to  $J = 40$  by Schöier et al. (2005). It can be seen that for up to  $J = 35$  the results with the three sets of collisional rates are indistinguishable. For higher transition the two sets from Neufeld display some differences, but these are at most a factor of 2. It can be concluded that for the first 35 transitions any CO data file can be used. However in order to investigate the higher transitions, it is necessary to use one of the

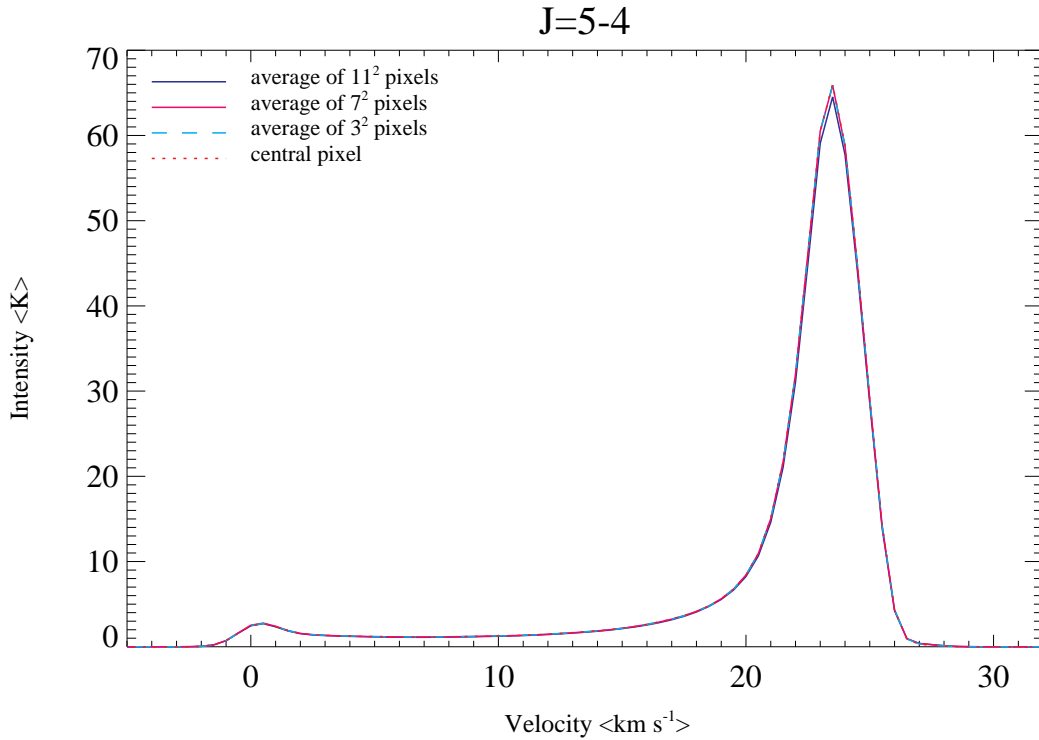


**Fig. 13.** The  $J = 5 - 4$  line profiles for the C-type shock model with  $r_{op} = 3.0$ ,  $v_s = 27 \text{ km s}^{-1}$ ,  $n_H = 10^5 \text{ cm}^{-3}$  and  $b = 1.0$  for four different pixel selections.



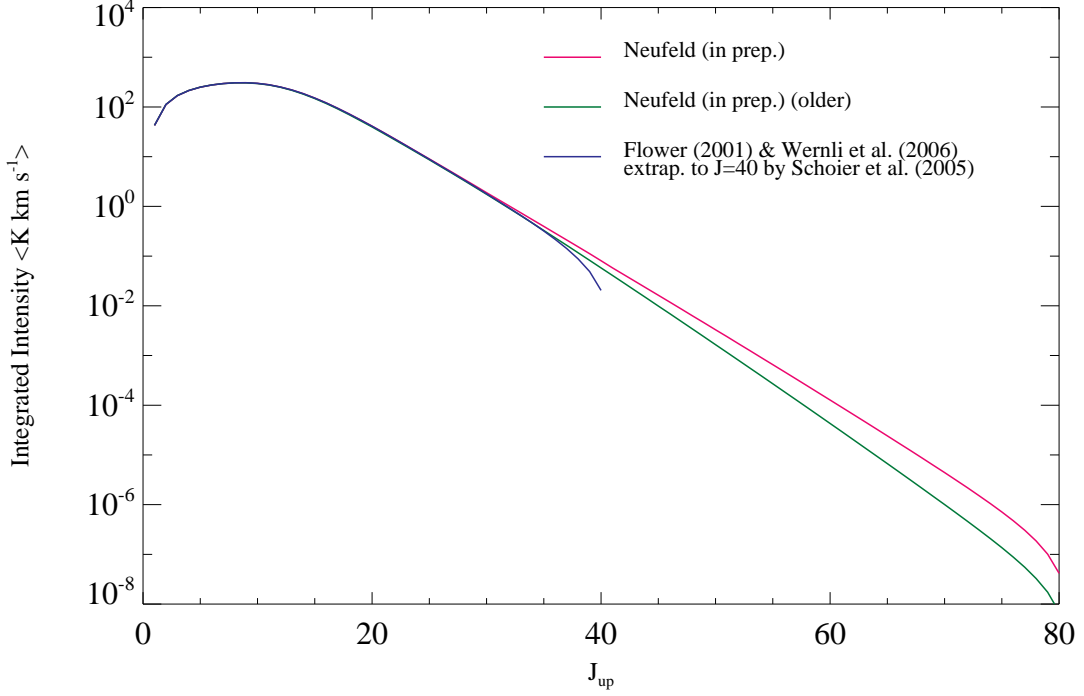


**Fig. 14.** The CO ladders for the C-type shock model with  $r_{op} = 3.0$ ,  $v_s = 27 \text{ km s}^{-1}$ ,  $n_H = 10^5 \text{ cm}^{-3}$  and  $b = 1.0$  with a logarithmic scale along the ordinate, as computed with three different CO data files.

Neufeld data files. In any case the differences will certainly be within a factor of 2 for  $J \geq 30$  and much better ( $\leq 3\%$ ) for lower  $J$ .

### 2.3. Robustness of LIME

A program is said to be *robust* if it performs well not only under ordinary conditions, but also under unusual conditions that stress its designers' assumptions. In this section the robustness of LIME is verified by means of two theoretical tests with known outcome criteria. For these tests the setup is kept identical to the one used for the shock runs, only the absolute mandatory changes were made as follows. The data points are still spread though a cylinder centered at the origin of a three dimensional Cartesian space and aligned along the  $z$ -axis, as before. The cylinder extends from  $-5 \cdot 10^{17} \text{ cm}$  to  $5 \cdot 10^{17} \text{ cm}$  and has a radius of 2610 AU (calculated using equation A.2). There is a linear velocity gradient through the cylinder, such that the velocity increases from  $0 \text{ km s}^{-1}$  at  $z = -5 \cdot 10^{17} \text{ cm}$  to  $10 \text{ km s}^{-1}$  at  $z = 5 \cdot 10^{17} \text{ cm}$ . Meanwhile the temperature is set to a constant 100 K, the fractional abundance of CO with respect to  $\text{H}_2$  is set to a constant  $10^{-4}$  and the density of  $\text{H}_2$  to a constant  $10^4 \text{ cm}^{-3}$ . The number of interior grid points is 3000 and the number of sink points is 2000. For all the details concerning the setup refer to Appendix E; there the source code modifications obligatory for carrying out these tests are also described.

Consider a collision dominated medium, i.e. a medium in which all radiative processes are negligible. It is expected that in this case LTE conditions exist. This means that a regular LIME run produces identical results to the special LTE run of LIME described in Appendix A. Furthermore, it is expected that  $T_{ex} = T_{kin}$  for all transitions, recalling Section 1.3. It was indeed established that the regular run and the special LTE run produced results within 1%. It was also computed that  $T_{ex} = 100 \text{ K}$ , which is  $T_{kin}$  in the setup. Hence LIME meets both conditions of passing the collision dominated medium test.

Consider a radiation dominated medium, i.e. a medium in which all collisional processes are negligible. It is expected that  $T_{ex} = T_{cmb}$  for all transitions, where  $T_{cmb}$  is the temperature of the cosmic microwave background. In the source code of LIME,  $T_{cmb}$  is set to equal 2.725 K. Upon running LIME under these conditions, it was computed that  $T_{ex} = 2.725 \text{ K}$  (4 s.f.). This means that LIME passed both tests and is therefore robust.

## 3. Results & Discussion

In this section the results of this research are presented. One of the primary goals of this research is to analyze the CO emission spectra acquired via LIME from over 200 shock models. All plots in this section use spectra averaged over  $7^2$  pixels for reasons given in Section 2.2.4.



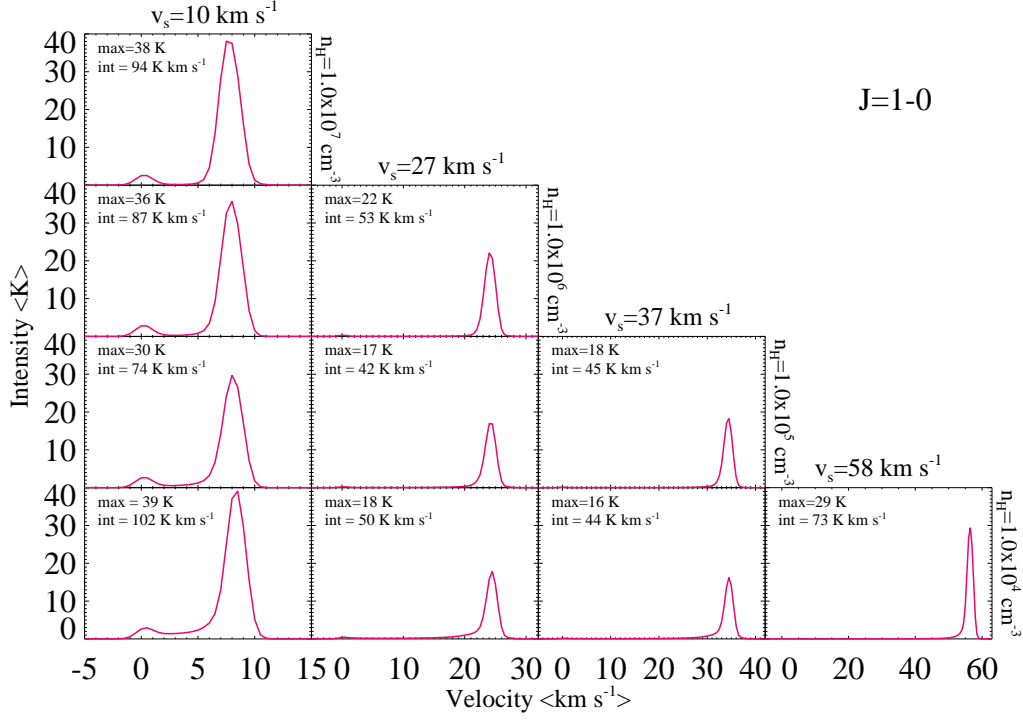


Fig. 15. The  $J = 1 - 0$  line profiles for ten representative shock models.

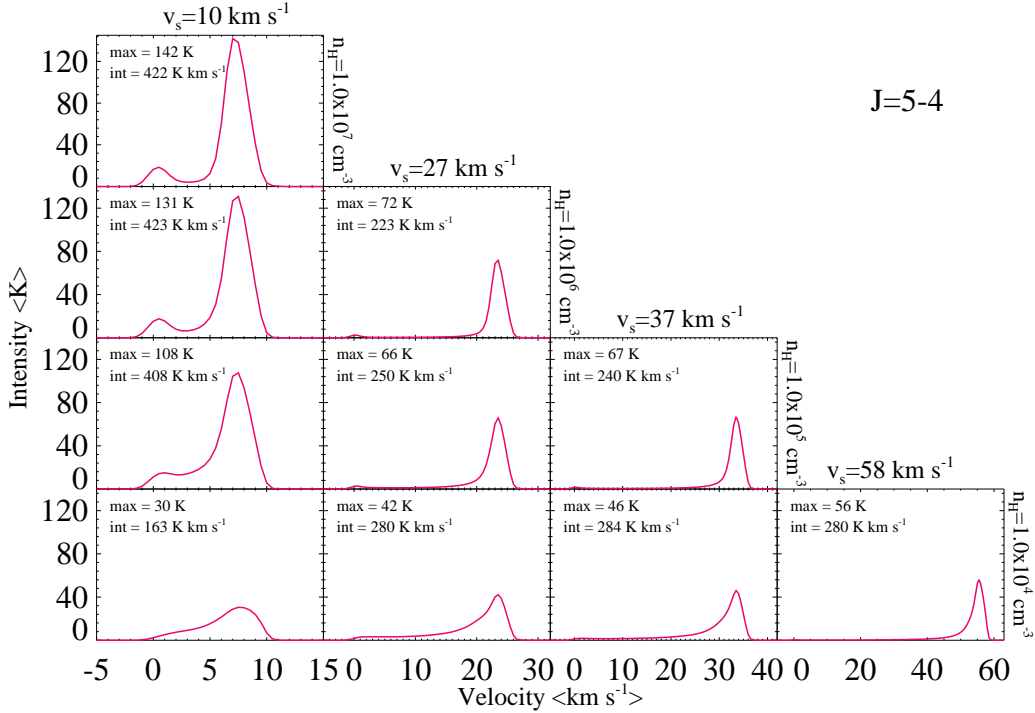
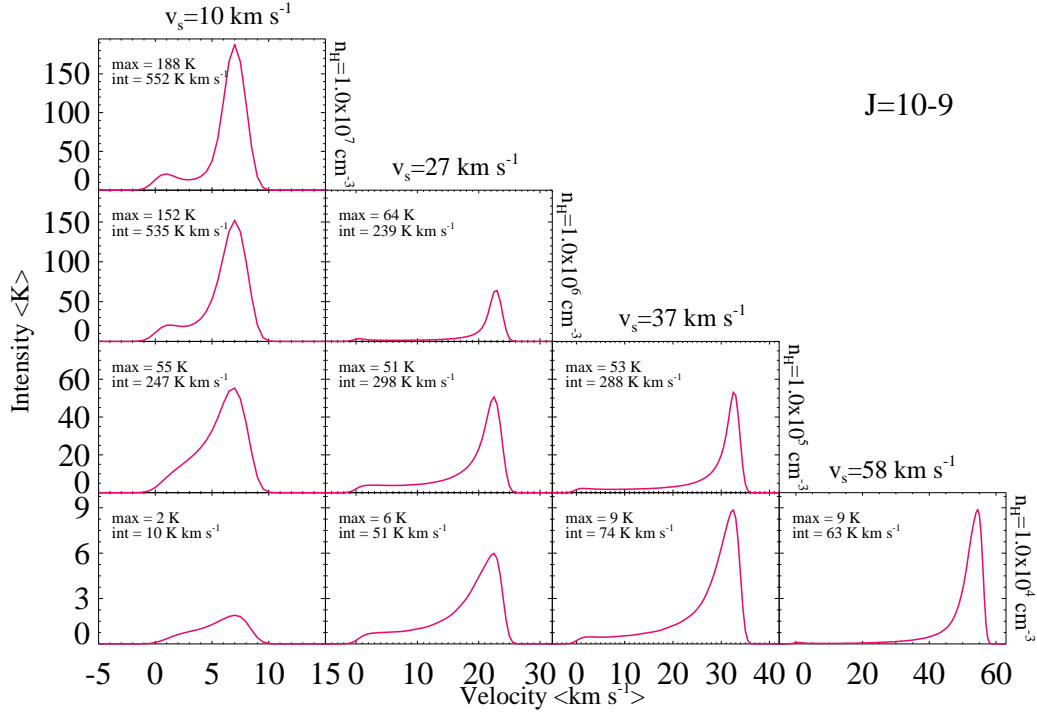


Fig. 16. The  $J = 5 - 4$  line profiles for ten representative shock models.

### 3.1. Line Profiles

In Fig. 15 the  $J = 1 - 0$  line profiles for ten representative models are presented. The peak intensity and the integrated intensity are also displayed for each model. In this figure the pre-shock gas is at the velocity of  $0 \text{ km s}^{-1}$  and the shock front is at its respective  $v_s$  value. From the maximum values and the integrated intensities it can be seen that there is more CO excited to the  $J = 1$  level with slow shocks, in this plot these are the shocks with  $v_s = 10 \text{ km s}^{-1}$ . Slower shocks are less energetic (equation 25), and thus are expected to excite CO to only the lower excitation levels. In Fig. 16



**Fig. 17.** The  $J = 10 - 9$  line profiles for ten representative shock models.

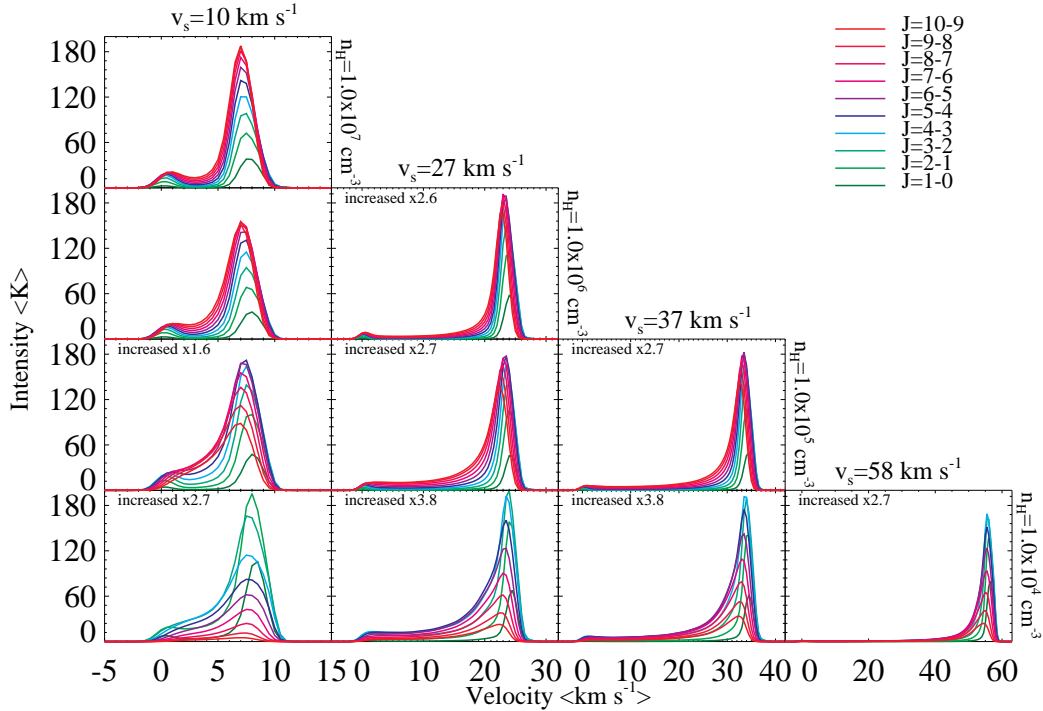


**Fig. 18.** The composite plot of line profiles from  $J_{\text{up}} = 1$  to  $J_{\text{up}} = 10$  for ten representative shock models.

the  $J = 5 - 4$  line profiles are displayed for the same ten models. For the highest three densities there is more CO excited to the  $J = 5$  level with slow shocks. For the lowest density,  $n_{\text{H}} = 10^4 \text{ cm}^{-3}$ , there is more excited CO in the  $J = 5$  level for faster shocks. The  $J = 5$  level is not a low-lying level like  $J = 1$ , where one expects to see more CO emission for slow shocks, however it is not a high-excitation level either like  $J = 10$ , where one expects to see more CO emission for fast shocks (since only they are sufficiently energetic to excite CO to the highest excited states). Therefore both trends are observed. Excitation also depends on  $n_i$  of a level  $i$  and is fast if  $n_i > n_{i,\text{crit}}$ . Thus for the C-type shock model with

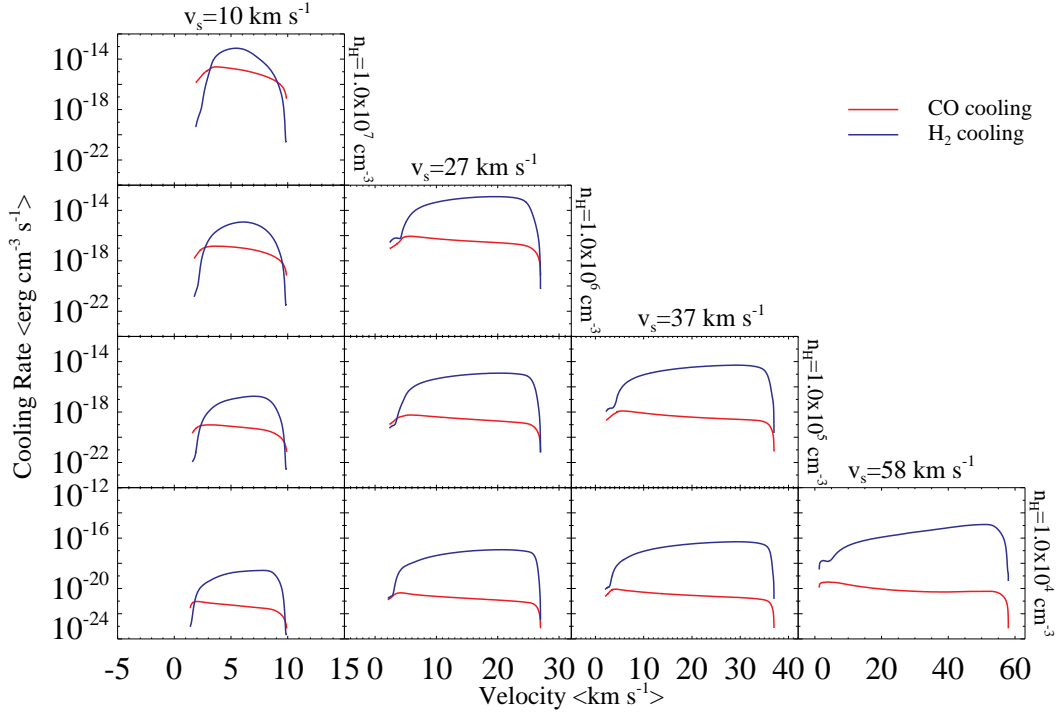


**Fig. 19.** The cooling curves of H<sub>2</sub> (blue) and CO (red) as a function of the velocity of neutrals with a logarithmic scale along the ordinate for ten representative shock models.

$r_{op} = 3.0$ ,  $v_s = 10 \text{ km s}^{-1}$ ,  $n_H = 10^4 \text{ cm}^{-3}$  and  $b = 1.0$  it seems that  $n_5 < n_{5, \text{crit}} \approx 1.4 \cdot 10^5 \text{ cm}^{-3}$  (see Section 1.3). Hence it is no surprise that both trends manifest themselves in this figure. Finally, in Fig. 17 the  $J = 10 - 9$  line profiles are shown. In this plot, as anticipated from the above stated, the faster the shock the more emission is observed, since  $J = 10$  is a high-excitation level. This is particularly visible for the lowest density. The  $v_s = 58 \text{ km s}^{-1}$  shock falls out of

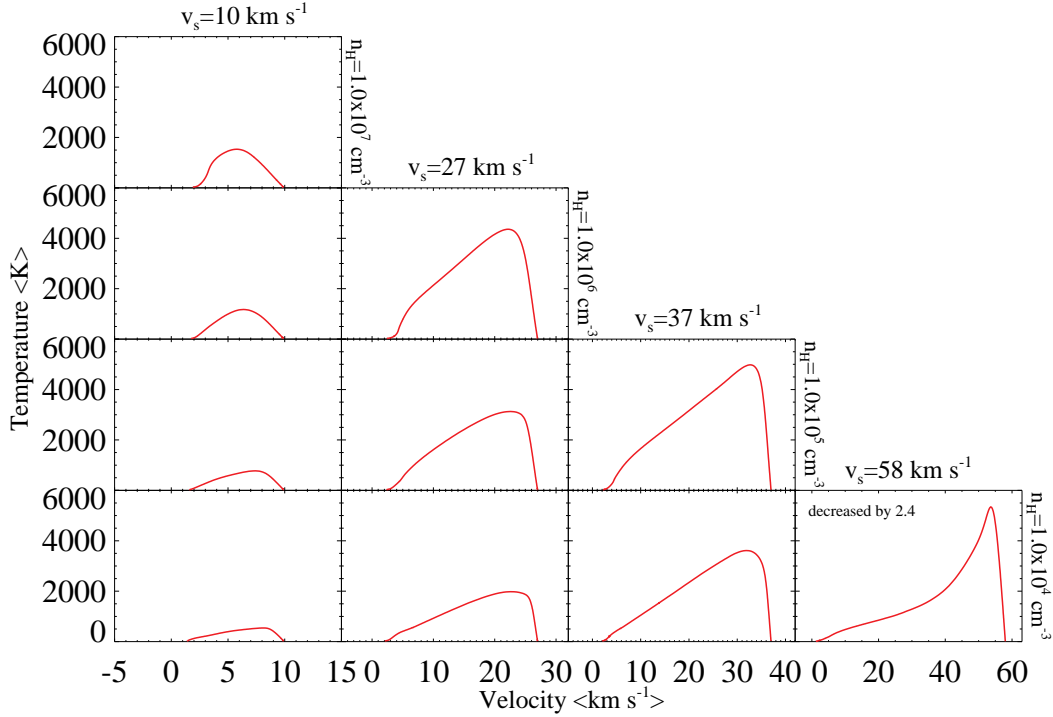


**Fig. 20.** The temperature profile, showing the changes in the temperature of neutrals with the passage of a shock as function of the velocity of neutrals for ten representative shock models.

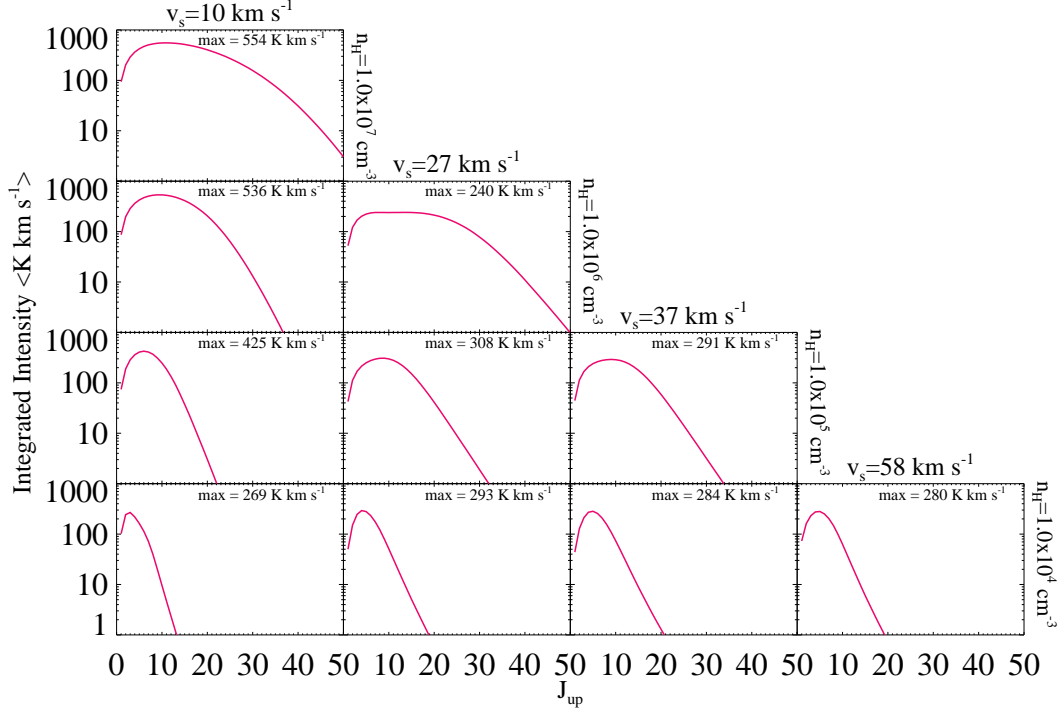


**Fig. 21.** The CO ladder for ten representative shock models with a logarithmic scale along the ordinate.

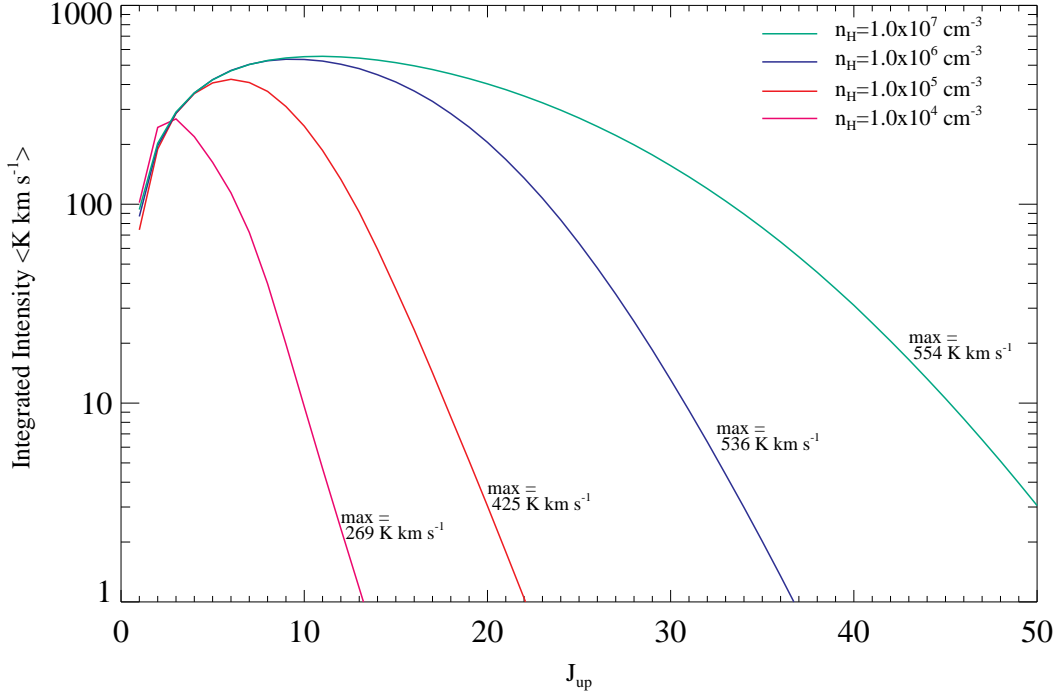


**Fig. 22.** The CO ladders for four shock models with  $v_s = 10 \text{ km s}^{-1}$  with a logarithmic scale along the ordinate.

the trend just a little bit, which probably has to do with  $n_{10}$  being just under  $n_{10,\text{crit}}$ . In this plot another trend becomes apparent: the higher the density, the more emission is observed. This is best visible for the slowest shocks. The higher the density, the more CO is present, the more CO can be excited and thus the more emission can be observed. This was not visible clearly for the other levels most likely as a result of the  $n_i$  not exceeding  $n_{i,\text{crit}}$ . A true rivalry between the dependence on the density and the shock velocity is seen here. Along the abscissa the shock velocity varies from  $10 \text{ km s}^{-1}$  to  $58 \text{ km s}^{-1}$ , since  $E \propto v_s^3$  (equation 25), the energy undergoes a variation of two orders of magnitude. Along the

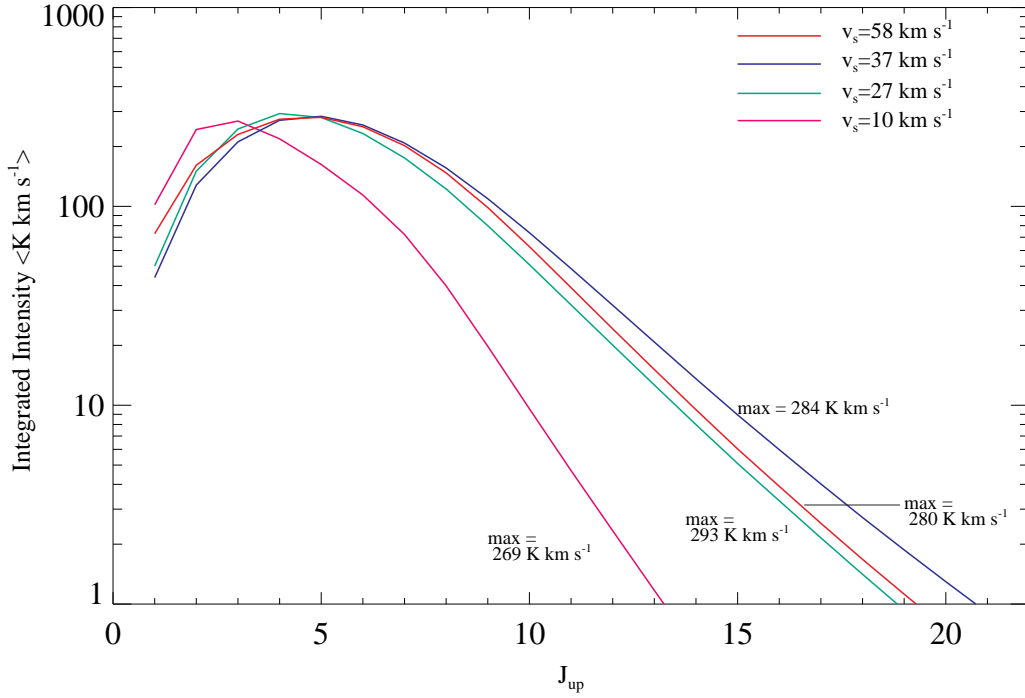


**Fig. 23.** The CO ladders for four shock models with  $n_{\text{H}} = 10^4 \text{ cm}^{-3}$  with a logarithmic scale along the ordinate.

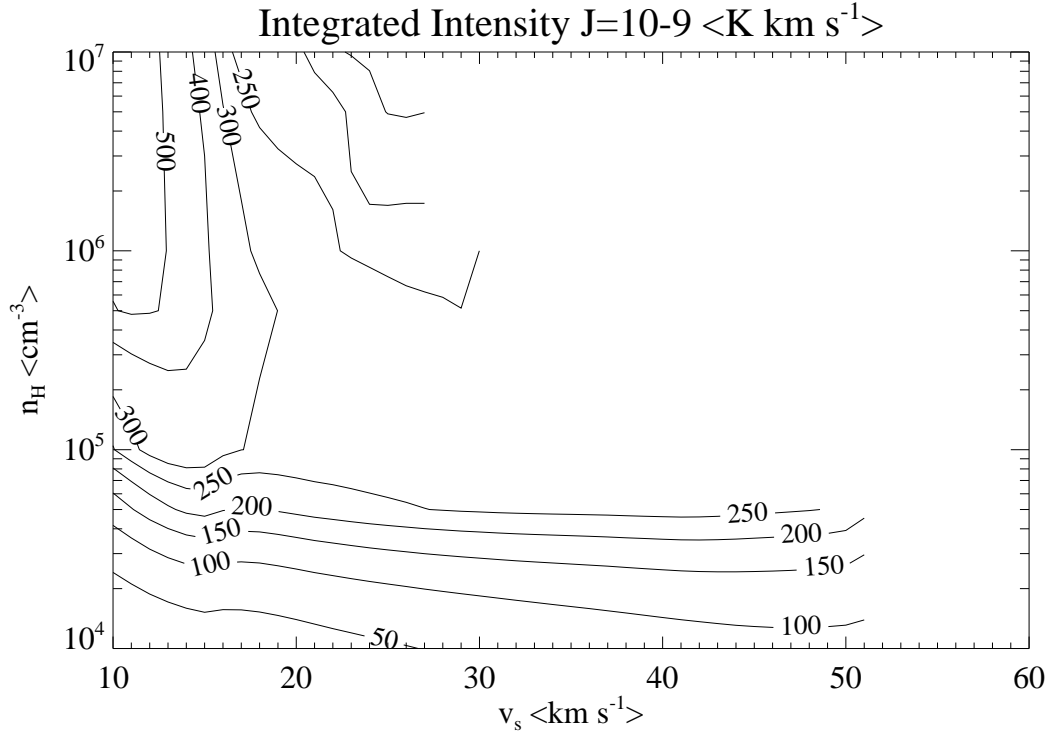


**Fig. 24.** The contour plot of the integrated intensity in the  $J = 10 - 9$  transition for all the shock models computed.

ordinate the density varies from  $10^4 \text{ cm}^{-3}$  to  $10^7 \text{ cm}^{-3}$ , since  $E \propto \rho$  (equation 25), the energy undergoes a variation of three orders of magnitude. This variation is what we see when we go either to the right along the abscissa or up along the ordinate. Line profiles are a measure of the energetic input of the shock. However the need to exceed  $n_{i,\text{crit}}$  further complicates the observed trends.

Another interesting feature observed in Fig. 15, 16 and 17 is that as we go to higher transitions the line profiles get wider for velocities smaller than  $v_s$  for all models. This trend is best visualized in a composite plot of the first ten

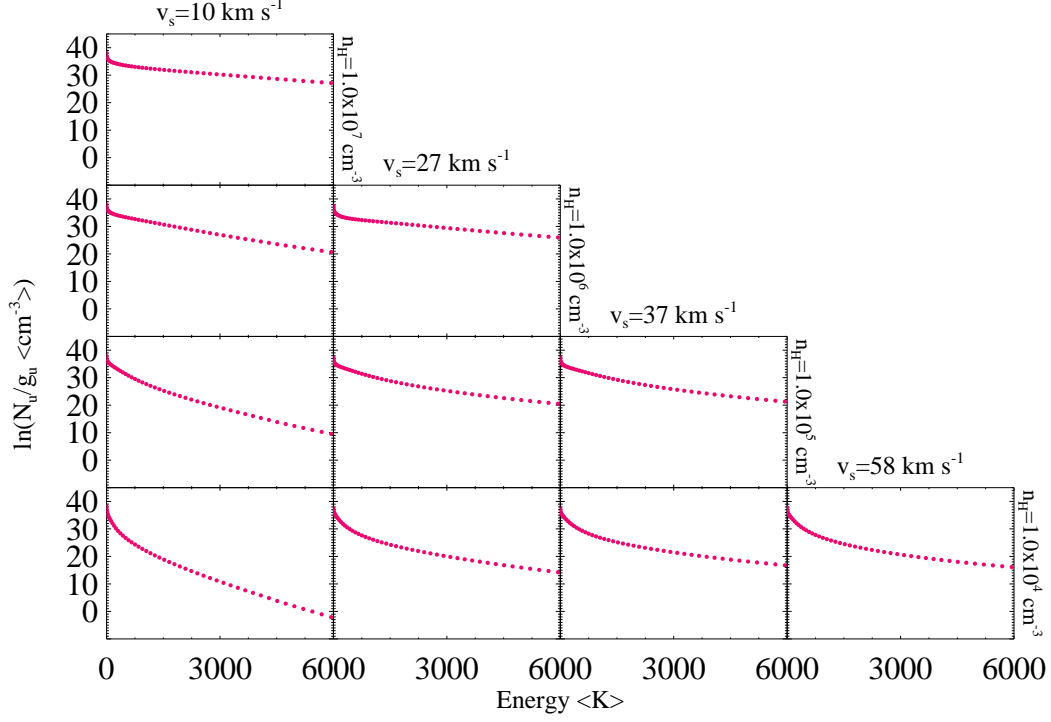


**Fig. 25.** The rotational diagrams for ten representative shock models.

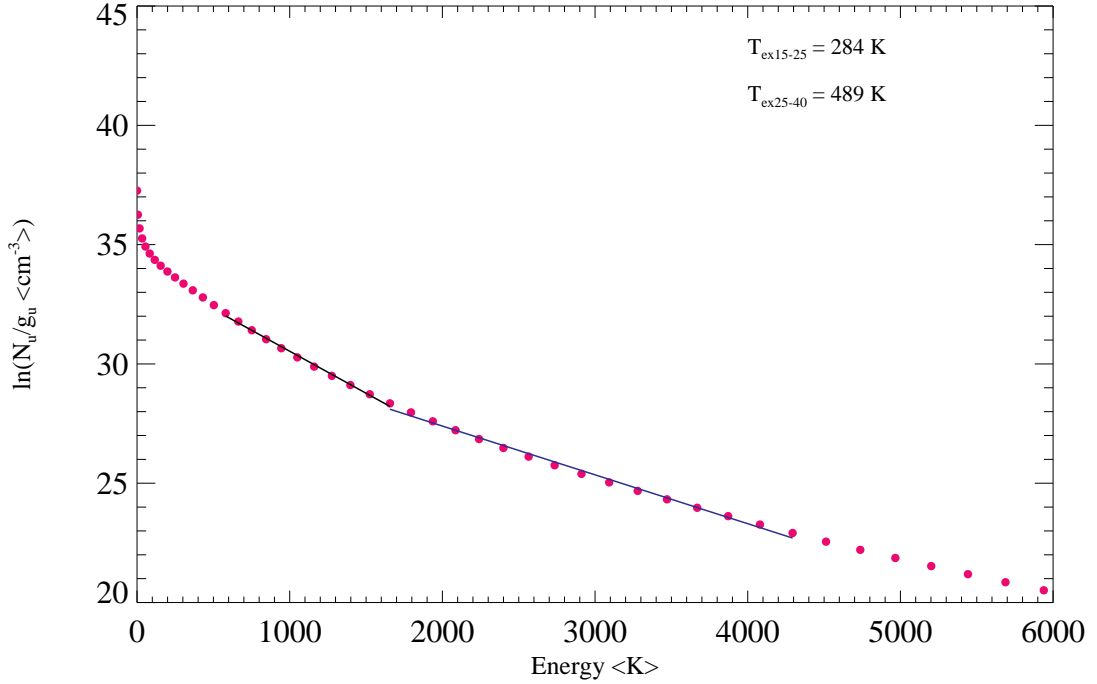


**Fig. 26.** The rotational diagram for the C-type shock model with  $r_{op} = 3.0$ ,  $v_s = 27 \text{ km s}^{-1}$ ,  $n_H = 10^5 \text{ cm}^{-3}$  and  $b = 1.0$  with two linear fits.

transitions, see Fig. 18. This widening can be seen in this composite plot and what it physically shows is that the shock is passing through the material. At  $v = v_s$  is where the shock front hits the gas and at this point all types of transitions are present. Then lower transitions fall off much quicker in number than the higher ones, because as the gas is being shocked a large amount of energy is released into the gas. Finally, all emission goes down as the energy is dissipated away. In this plot the trends mentioned in the previous paragraph are seen again. All these trends further persevere to the highest possible level transitions. The slow, low-density shock displays most emission in low transitions, notice that

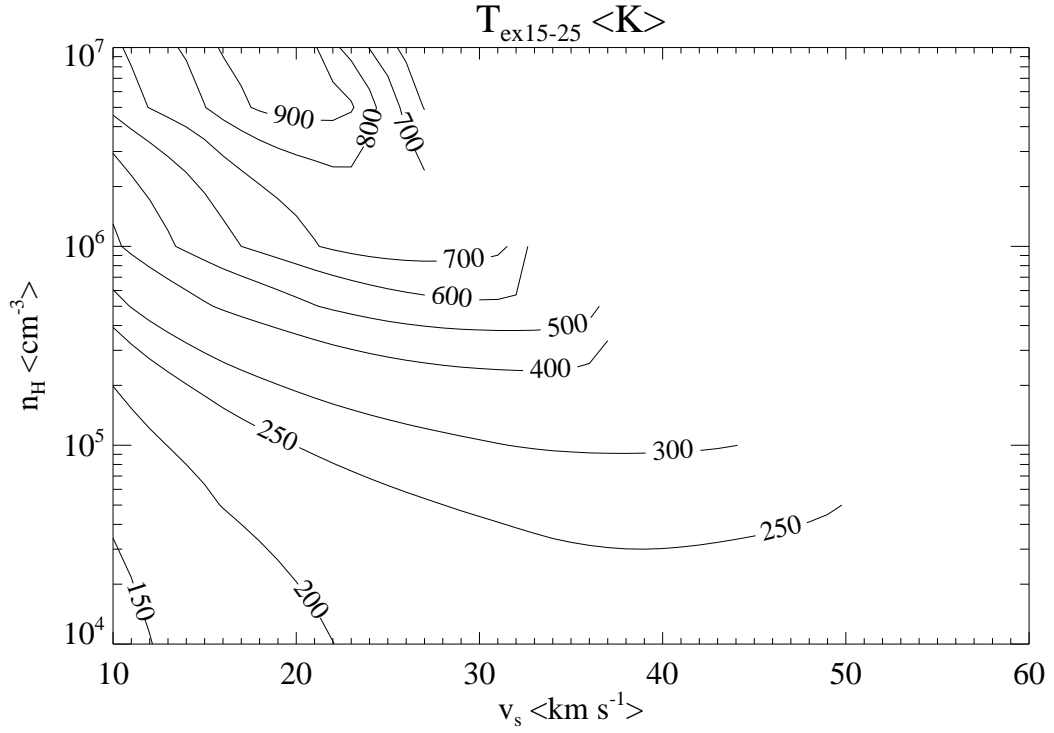


**Fig. 27.** The excitation temperature for  $J_{\text{up}} = 15 - 25$  contour plot for all the shock models computed.

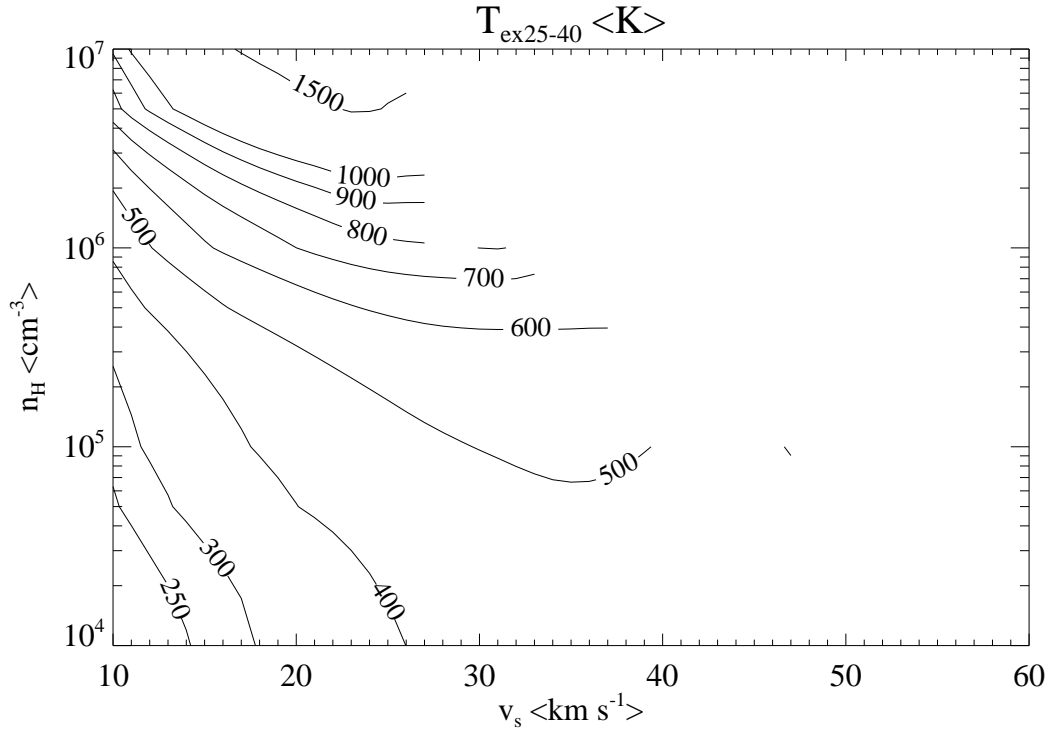


**Fig. 28.** The excitation temperature for  $J_{\text{up}} = 25 - 40$  contour plot for all the shock models computed.

for the  $v_s = 10 \text{ km s}^{-1}$  and  $n_H = 10^4 \text{ cm}^{-3}$  shock the highest peak is for the  $J = 2 - 1$  transition. The slow, dense shock  $v_s = 10 \text{ km s}^{-1}$  and  $n_H = 10^7 \text{ cm}^{-3}$  displays emission peaking for the  $J = 10 - 9$  transition and in fact, even for a higher transition, which is not displayed in this figure. The fast shock  $v_s = 58 \text{ km s}^{-1}$  and  $n_H = 10^4 \text{ cm}^{-3}$  displays emission peaking for the  $J = 4 - 3$  transition. Meanwhile the inner models of the diagram peak at intermediate transitions around  $J = 7 - 6$ . This is another good visualization of the tug war between the shock velocity and the density with what appears to be a stronger pull along the density.

There is another curious feature present in all three line profile sets presented. There is a very prominent second peak in the emission for slow shocks and a smaller one for the models with  $v_s = 27 \text{ km s}^{-1}$ . For an explanation of this phenomenon it is useful to turn to the cooling profiles as a function of the velocity of neutrals. In Fig. 19 the cooling curves of  $\text{H}_2$  and  $^{13}\text{CO}$  are presented for the same ten shock models. Note that these have been accordingly truncated too. The cooling of  $^{12}\text{CO}$  is approximated in the MHD simulations to be 65 times that of  $^{13}\text{CO}$ , as it cannot be computed directly as a result of being optically thick, unlike the optically thin  $^{13}\text{CO}$ . From this figure the answer to the mysterious secondary peak becomes obvious. For the slower shocks, like those with  $v_s = 10 \text{ km s}^{-1}$  and  $v_s = 27 \text{ km s}^{-1}$ , CO dominates the cooling around  $v = 0 \text{ km s}^{-1}$  rather than  $\text{H}_2$ . This leads to the emission peak around  $v = 0 \text{ km s}^{-1}$  in the line profiles. One can also spot that very close to the shock velocity CO dominates cooling yet again. The reason that there is no peak there in the presented line profiles, is because this dominance is much smaller and since the Doppler  $b$ -parameter is set to  $1 \text{ km s}^{-1}$  this peak is smeared together with the primary emission peak (see 4.2 for verification).

In order to explain why CO is capable of dominating cooling over  $\text{H}_2$  for some parts of certain models one should turn to the temperature profiles of neutrals. In Fig. 20 the temperature of neutrals is plotted for the ten models as a function of the velocity of the neutrals. For the slower models the temperature gradient is quite low around  $v = 0 \text{ km s}^{-1}$ , while for the other models it is much higher. The same observation can be made at the other end, around the value of  $v_s$ .  $\text{H}_2$  requires a sufficiently high temperature for it to efficiently cool the gas via its electric quadrupole transitions (Section 1.2). For slower shocks around  $v = 0 \text{ km s}^{-1}$  the temperature of the gas does not rise fast enough for  $\text{H}_2$  cooling to be effective, therefore CO takes over the cooling of the gas via its electric dipole transitions. The same happens very close to  $v_s$  too.

### 3.2. CO Ladders

In Fig. 21 are the CO ladders for the ten models analyzed on a logarithmic scale along the ordinate. The CO ladders, just like the individual line profiles making them up, are a reflection of the energetic input of the shock. The same argument can be made about how the energy undergoes a variation of two orders of magnitude along the abscissa and a variation of three orders of magnitude along the ordinate. In Fig. 22 the four CO ladders corresponding to the slowest shocks with  $v_s = 10 \text{ km s}^{-1}$  are overplotted and in Fig. 23 the four CO ladders corresponding to the least dense shocks with  $n_{\text{H}} = 10^4 \text{ cm}^{-3}$  are overplotted. In Fig. 23 the ladders are much closer together, displaying weak dependence on shock velocity. Meanwhile in Fig. 22 the ladders show large discrepancies between one another, displaying a much stronger dependence on density. This boils down to the observation that CO appears to be primarily a tracer of the pre-shock density rather than the shock velocity. It is possible to visualize this further by means of a contour plot of the integrated intensity in the  $J = 10 - 9$  transition in Fig. 24. For densities of around  $10^5 \text{ cm}^{-3}$  and below, the integrated intensity depends only on the pre-shock density and it cannot be used to discriminate between different shock velocities. For pre-shock densities above  $10^5 \text{ cm}^{-3}$  a drastic change occurs, the contours become almost vertical rather than horizontal for lower densities. In Section 1.3 it was calculated that  $n_{10\text{crit}} = 6.1 \cdot 10^5 \text{ cm}^{-3}$  for  $T = 500 \text{ K}$ . Since here the temperature under question is not exactly  $500 \text{ K}$ , it appears that  $n_{10\text{crit}} \approx 10^5 \text{ cm}^{-3}$  instead. At this density the  $J = 10 - 9$  transition switches from being radiation dominated to collisionally dominated. This is the reason for the contour lines becoming vertical. For densities higher than  $10^5 \text{ cm}^{-3}$  this transition is collision dominated, hence it purely traces the density, as the more CO there is, the more emission there will be in this line.

### 3.3. Rotation Diagrams

In Fig. 25 the rotation diagrams for the ten models are presented. From them it can be derived that the level populations also reflect the energy of the shock prescribed by equation 25. This comes as no surprise, since level populations prescribe emission. It appears that the more energetic a shock is, the more horizontal its curve in a rotational diagram becomes and the higher its  $T_{\text{ex}}$ . This leads to the bend between the lowest transitions and the higher transitions to be more acute for more energetic shocks. Note that insignificant data points are excluded from these plots, by which are meant points, which are unrealistic due to the very small numbers encountered in the calculations. Another point that can be established from these diagrams is that shocks are not in LTE, since the curves are not straight lines, which is much expected. Now consider one of these diagrams in detail. In Fig. 26 the rotational diagram for the shock model with  $v_s = 27 \text{ km s}^{-1}$  and  $n_{\text{H}} = 10^5 \text{ cm}^{-3}$  is displayed. Even if a system is not in LTE, it is still possible to calculate “excitation temperatures” for subsets of the data points. That is precisely what is done here. One linear fit is made for data points corresponding to  $J = 15$  through  $J = 25$ , and another one for data points corresponding to  $J = 25$  through  $J = 40$ . This gives the excitation temperature corresponding to the  $J_{\text{up}} = 15 - 25$  subset, denoted  $T_{\text{ex}15-25}$ , and the excitation temperature corresponding to the  $J_{\text{up}} = 25 - 40$  subset, denoted  $T_{\text{ex}25-40}$ . For this shock model  $T_{\text{ex}15-25} = 284 \text{ K}$  and  $T_{\text{ex}25-40} = 489 \text{ K}$ . From this figure it can be seen that the linear fits for the over the two ranges made are quite good, even though the data points appear to trace out a continuous curve.

If such fitting is done for all the models computed in this research, two contour plots can be made, one for  $T_{\text{ex}15-25}$  and another for  $T_{\text{ex}25-40}$ . These are respectively Fig. 27 and 28. From these plots it is very easy to determine the type of shock at play from an observed excitation temperature. From Fig. 27 it can be seen that  $T_{\text{ex}15-25}$  does not vary strongly with  $v_s$ , since some contours are almost horizontal, with the exceptions of the two highest  $T_{\text{ex}15-25}$  contours of  $800 \text{ K}$  and  $900 \text{ K}$ , and the two lowest  $T_{\text{ex}15-25}$  contours of  $150 \text{ K}$  and  $200 \text{ K}$ . Pre-shock densities varying between  $10^5 \text{ cm}^{-3}$  and  $10^6 \text{ cm}^{-3}$  have  $T_{\text{ex}15-25} \in [250, 600] \text{ K}$  roughly. Only the higher densities between  $10^6 \text{ cm}^{-3}$  and  $10^7 \text{ cm}^{-3}$  will attain



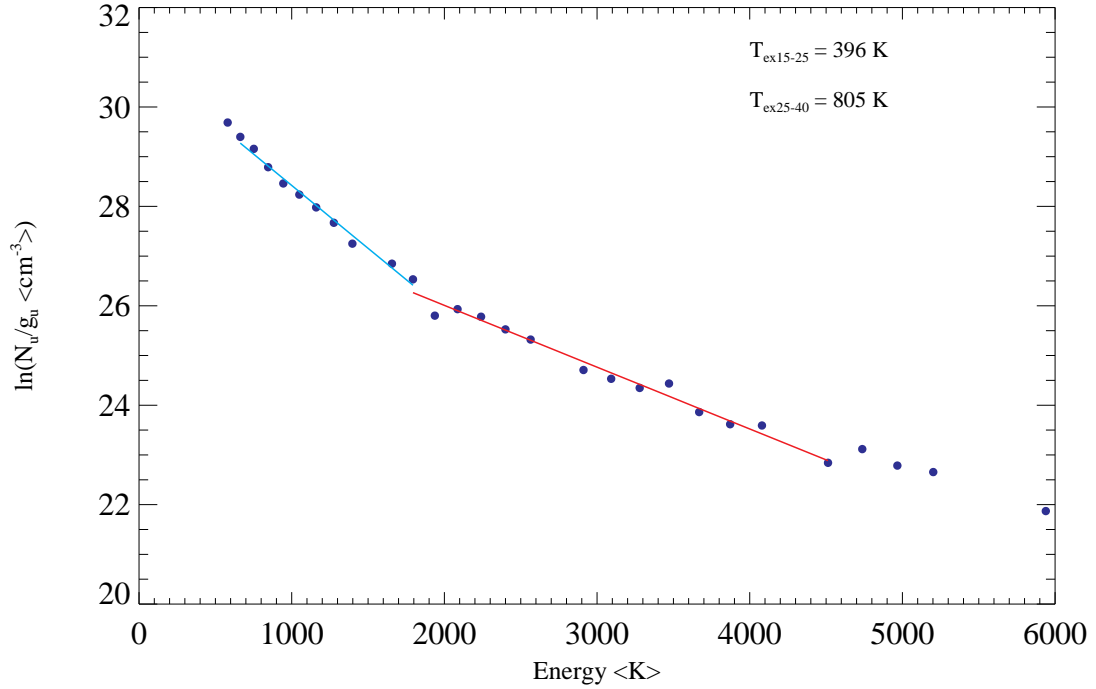


**Fig. 29.** The rotational diagram for the low-mass protostar NGC1333-IRAS4A, as computed by Karska, Herczeg et al. (in prep.).

**Table 1.** Source Properties (van Dishoeck et al. 2011).

Source	RA <h m s>	Dec <° ' " >	L <sub>bol</sub> <L <sub>⊙</sub> >	d <pc>
NGC1333-IRAS4A	03 29 10.5	+31 13 30.9	7.7	235
Serpens-SMM1	18 29 49.8	+01 15 20.5	30	250

$T_{ex15-25}$  closer to 900 K. Meanwhile the lower densities between  $10^4 \text{ cm}^{-3}$  and  $10^5 \text{ cm}^{-3}$  will attain  $T_{ex15-25}$  of at most to 200 K. From Fig. 28 it can be seen that  $T_{ex25-40}$  does not vary with  $v_s$  at all for densities varying between  $3 \cdot 10^5 \text{ cm}^{-3}$  and  $10^7 \text{ cm}^{-3}$ , with corresponding  $T_{ex25-40} \in [600, 1500] \text{ K}$  and mildly for densities lower than  $3 \cdot 10^5 \text{ cm}^{-3}$ , with corresponding  $T_{ex25-40} \leq 400 \text{ K}$  approximately.

There are a number of interesting conclusions an observer can draw from the above presented results. Suppose observations have been made, and  $T_{ex15-25} > 300 \text{ K}$  and  $T_{ex25-40} > 600 \text{ K}$  have been calculated. The observer can then refer to Fig. 27 and Fig. 28 to determine a pre-shock density associated with the observed shock, which would definitely be greater than  $10^5 \text{ cm}^{-3}$ . In general, one can get the pre-shock density corresponding to these two excitation temperatures to roughly within a factor of 2. However the shock velocity cannot be determined from this. The observer can then turn to his/her individual line profiles and determine at what velocity they peak relative to that of the unshocked gas. The velocity, at which the peak is observed, is not the exact shock velocity in observations, but rather the projection of  $v_s$  on the line of sight. So this gives a minimum value of  $v_s$ . This already gives the observer some significant information about the shock observed. However since other species are commonly observed to complement CO, they could be a source of other shock diagnostics. This is however beyond the scope of this research.

### 3.4. Application to Observations

Finally, two data sets are presented as an example of how an observer can go about interpreting results from an observation. In Fig. 29 and Fig. 30 the rotational diagrams for two low-mass protostars NGC1333-IRAS4A and Serpens-SMM1 are presented, as computed by Karska, Herczeg et al. (in prep.). Some key properties for these two sources are given in Table 1 (van Dishoeck et al. 2011), namely the right ascension (RA), the declination (Dec), the bolometric luminosity ( $L_{bol}$ ) and the distance (d). These two objects have been recently observed as part of the key program “Water in Star-Forming Regions with *Herschel*” (WISH, van Dishoeck et al. 2011). Full *PACS* scans were obtained for each source revealing the entire CO ladder from  $J = 14 - 13$  to  $J = 43 - 42$  between approximately  $60 \mu\text{m}$  and  $180 \mu\text{m}$  (Karska, Herczeg et al. in prep.). From past observations it is known that they display prominent outflow activity. For these figures the blended lines are excluded. Consider Fig. 29 of NGC1333-IRAS4A. For this source  $T_{ex15-25} = 396 \text{ K}$ , which implies a pre-shock density of around  $3 \cdot 10^5 \text{ cm}^{-3}$ , based on Fig. 27, while  $T_{ex25-40} = 805 \text{ K}$ , which implies a pre-shock density of around  $10^6 \text{ cm}^{-3}$ , based on Fig. 28. Consider Fig. 30 of Serpens-SMM1. For this source  $T_{ex15-25} = 360 \text{ K}$ , which implies

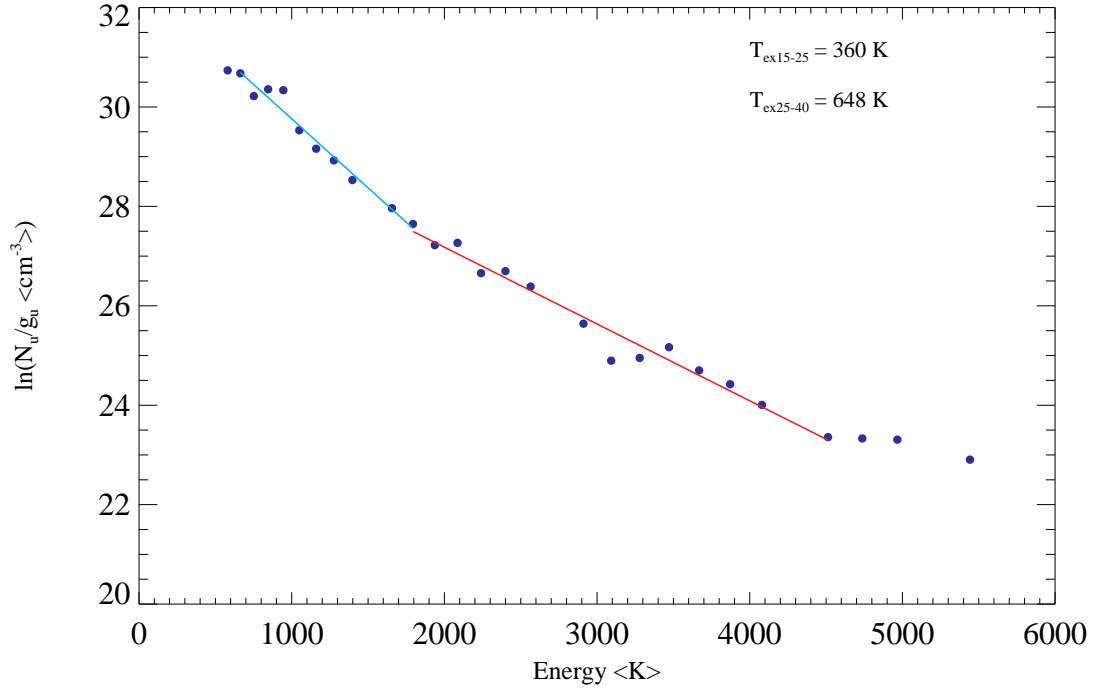


**Fig. 30.** The rotational diagram for the low-mass protostar Serpens-SMM1, as computed by Karska, Herczeg et al. (in prep).

a pre-shock density of around  $2 \cdot 10^5 \text{ cm}^{-3}$ , based on Fig. 27, while  $T_{ex25-40} = 648 \text{ K}$ , which implies a pre-shock density of around  $8 \cdot 10^5 \text{ cm}^{-3}$ , based on Fig. 28. From these incompatible facts it can be concluded that these observations could not have been produced by a single shock. It is possible that such observed CO emission is in fact a combination of UV heating and C-type shocks. This was concluded for other *Herschel* observations of low-mass young stellar objects such as HH 46, NGC1333-IRAS2A and DK Cha by Visser et al. (subm.).

## 4. Comparison of LIME with LVG

### 4.1. LVG

The Large Velocity Gradient (LVG, Gusdorf 2008) program is another radiation transfer code that can be used to predict the emission from a source. It is based on the so-called LVG approximation. When a velocity gradient is sufficiently high, an emitted photon undergoes a Doppler shift that is larger than the local width of the line, in which it was emitted. As a result such a photon can no longer be absorbed by ambient atoms or molecules, i.e. the matter has become transparent for the photon. The LVG calculations are carried out in 1D and point-wise. At the first data point the level populations are initialized to a value prescribed by the Boltzmann distribution for the considered molecule at the temperature of that first point. At the next point the level populations are taken to be that of the preceding point to zeroth order. Then a Lambda iteration is carried out and the relevant physical parameters are calculated, and the equations of radiative transfer are solved, with the use of the LVG approximation. This is repeated for all subsequent points one by one. The LVG output consists of a few files containing the calculated intensities, integrated intensities, etc. for every single data point that was given in the input. One key difference between LIME and LVG is that the calculations are performed in 3D, resp. 1D. Another key difference is that LVG's calculations are point-wise for every single data point. Meanwhile in LIME grid points differing from the data points are generated, and the calculations are performed along lines (along the boundaries of Delaunay cells for the generation of the radiation field and through Voronoi cells for the ray-tracing). There are fewer assumptions going into LIME than there are going into LVG.

### 4.2. Results

In this section the comparison between the LIME and the LVG output is performed via CO emission. The LIME setup remains unchanged from that used in the above discussions. The LVG output has been supplied by Kristensen through the use of a code supplied by Gusdorf. LVG calculations are done on the basis of a 41 level CO data file from Yang et al. (2010), made available on LAMDA (Schöier et al. 2005), therefore the comparison will be performed up to  $J_{up} = 41$ . The LVG output can be manually truncated in any way, as it does not keep memory of the preceding points in its calculations.

In Fig. 31 the  $J = 1 - 0$  emission is displayed for the same ten representative models used previously as calculated with LIME and with LVG. It appears that LVG consistently overestimates the peak intensities and the integrated intensity in

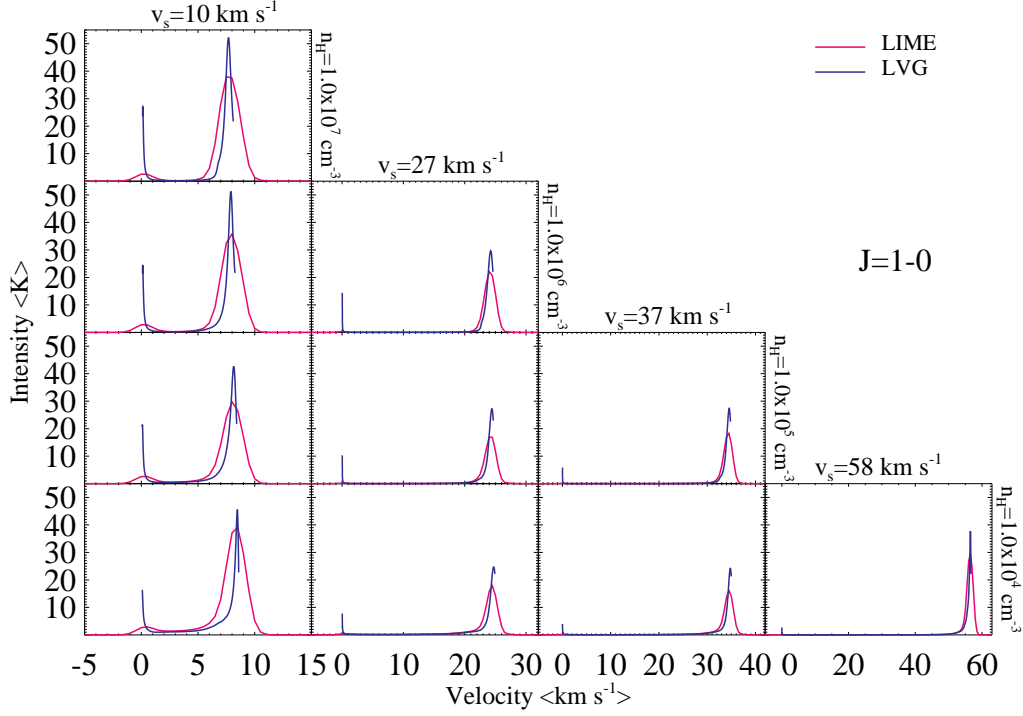


**Fig. 31.** The  $J = 1 - 0$  line profiles for ten representative shock models as computed by LIME and LVG.

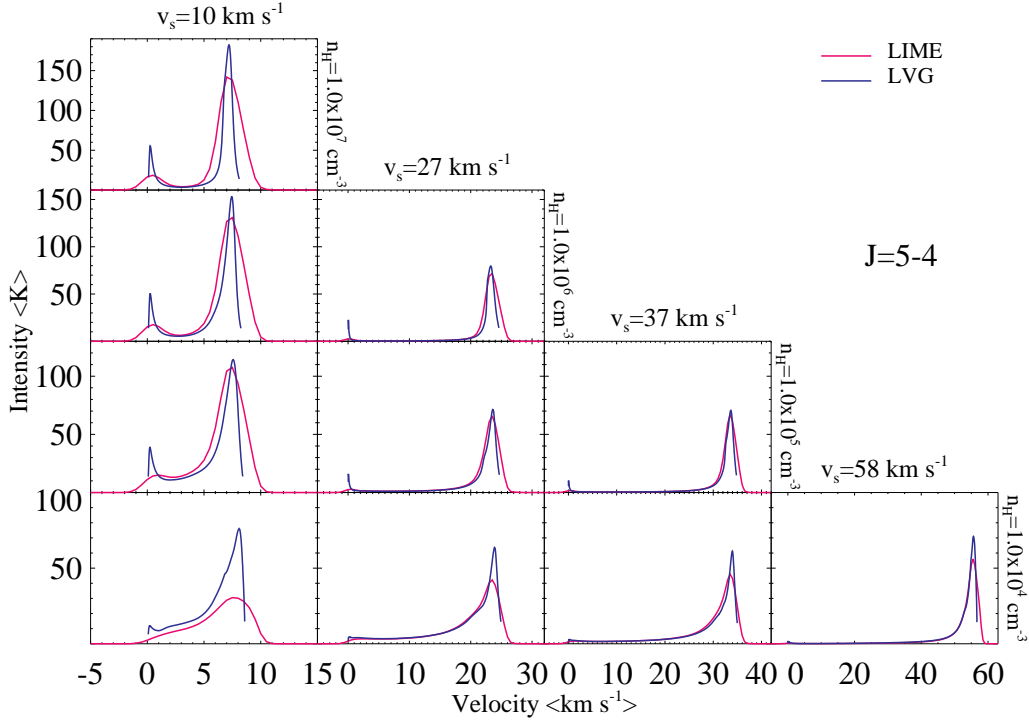


**Fig. 32.** The  $J = 5 - 4$  line profiles for ten representative shock models as computed by LIME and LVG.

this lowest rotational transition. For all ten models the peak intensity calculated with LVG is higher than that calculated with LIME. This also holds for the secondary peak around  $v_s = 0 \text{ km s}^{-1}$ . The two codes do agree in the positioning of both peaks. The integrated intensity calculated with LIME is higher than that calculated with LVG. Furthermore, the LIME line profiles tend to be wider than those of LVG, in particular with the slower models. The line profiles of LVG do not drop to 0 K either, like the LIME ones do, since LVG performs its calculations point-wise. In Fig. 32 the  $J = 5 - 4$  emission is displayed for the same ten models for both codes. For this transition LVG too overestimates both

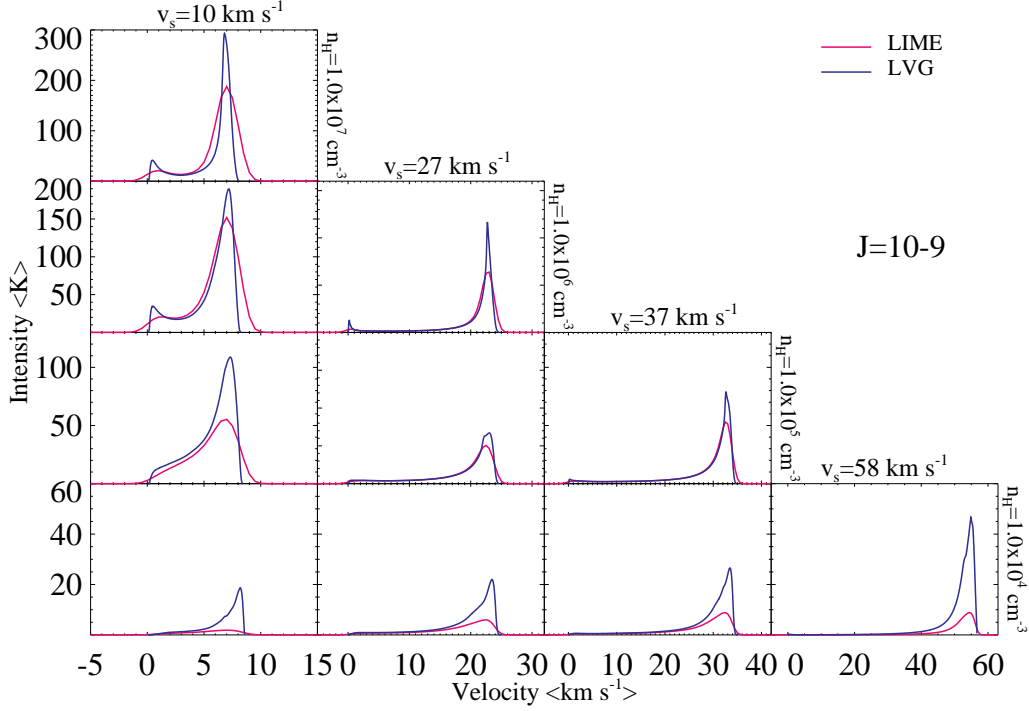


**Fig. 33.** The  $J = 10 - 9$  line profiles for ten representative shock models as computed by LIME and LVG.

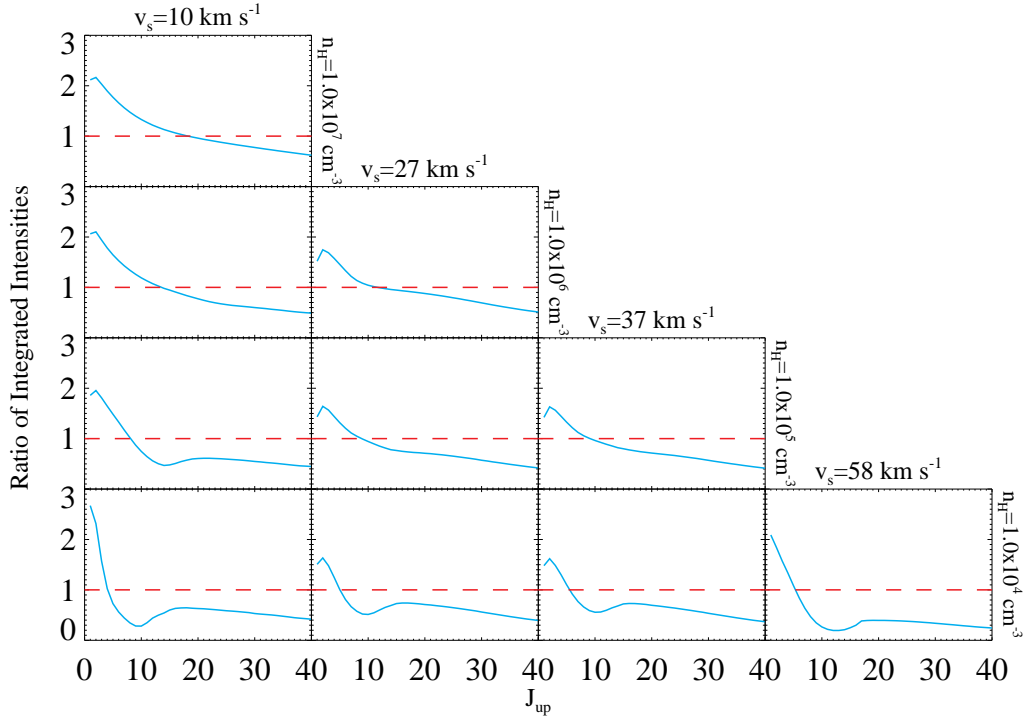


**Fig. 34.** The ratio of the LIME and LVG CO ladders (solid aqua) for ten representative shock models. The dashed red line corresponds to a perfect match, i.e. a ratio of 1.

peak intensities, as well as it produces thinner profiles. The positioning of the two peaks is again the same for both. Moreover, the three inner models of the figure display good agreement in the primary intensity peak in this transition, within 10 K of each other. The integrated intensities appear to coincide within a factor of less than 3. However the C-type shock model with  $r_{op} = 3.0$ ,  $v_s = 10 \text{ km s}^{-1}$ ,  $n_H = 10^4 \text{ cm}^{-3}$  and  $b = 1.0$  displays a very poor agreement, the peak intensity alone shows a mismatch of 50 K. In Fig. 33 the  $J = 10 - 9$  emission is shown. The LVG overestimation of

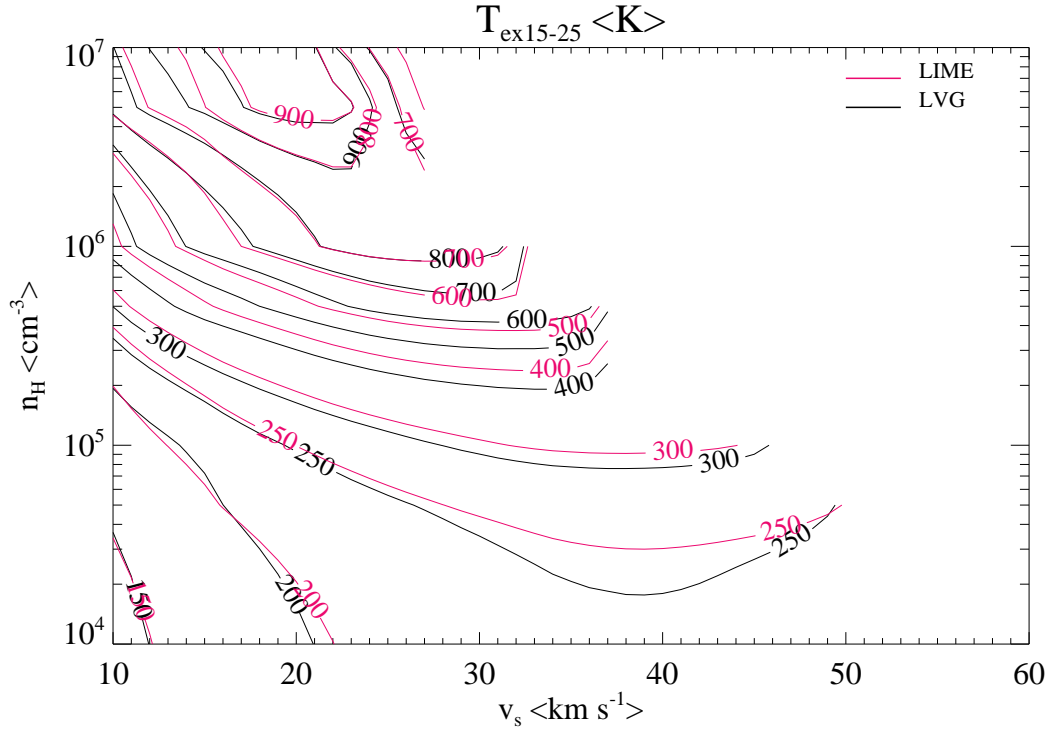


**Fig. 35.** The contour plot for all the shock models computed with the excitation temperature for  $J_{\text{up}} = 15 - 25$  as computed by LIME and LVG.

the peaks persists, while the width of the line profiles seems to agree somewhat better. However no models show decent agreement of a factor close to 1, like they did in the  $J = 5 - 4$  transition for inner models. The locations of the peaks still match. Upon comparing the integrated intensities of LIME and LVG in Fig. 33 to the integrated intensities in other

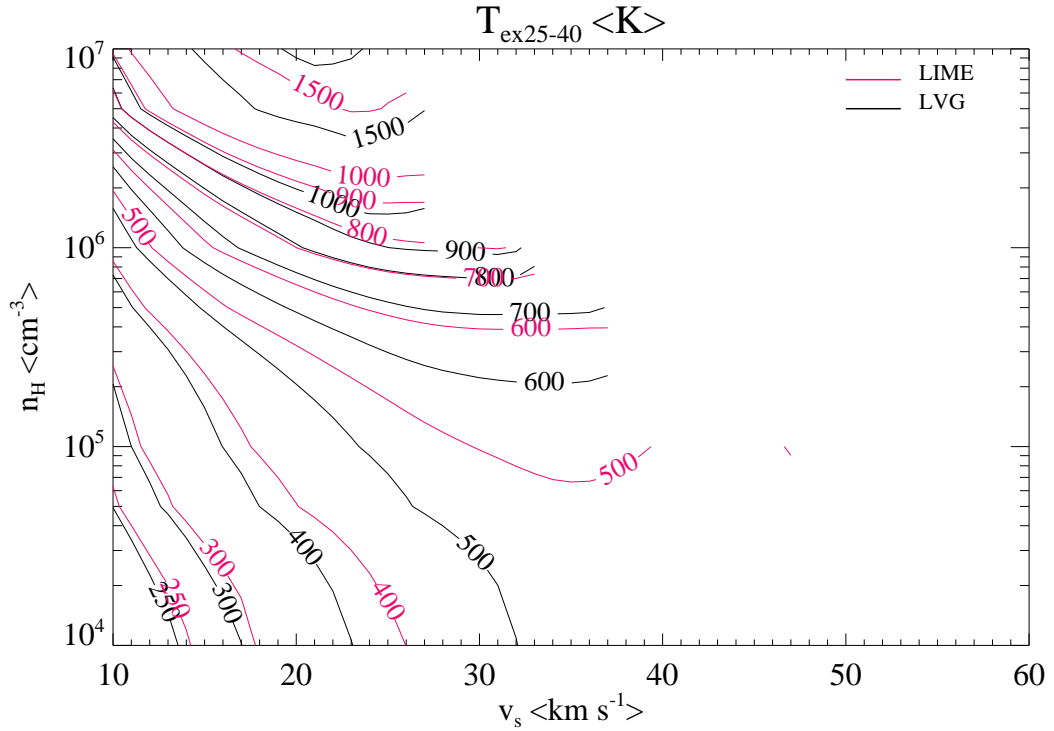


**Fig. 36.** The contour plot for all the shock models computed with the excitation temperature for  $J_{\text{up}} = 25 - 40$  as computed by LIME and LVG.

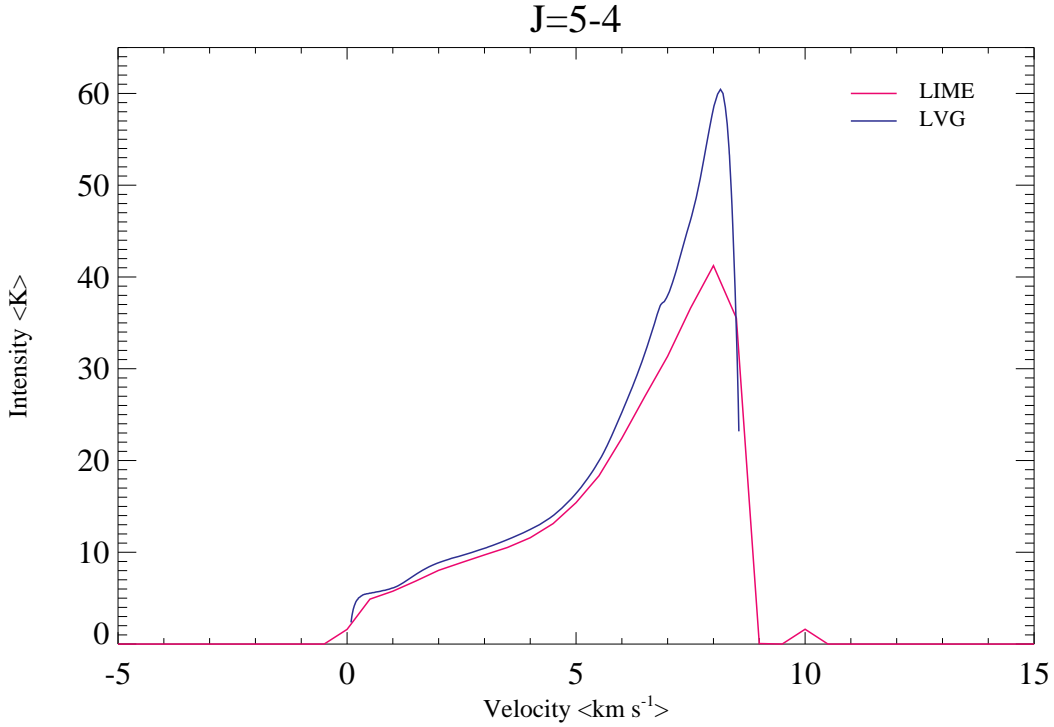


**Fig. 37.** The  $J = 5 - 4$  line profile for the C-type shock model with  $r_{op} = 3.0$ ,  $v_s = 10 \text{ km s}^{-1}$ ,  $n_H = 10^4 \text{ cm}^{-3}$  and  $b = 1.0$  as computed by LIME and LVG (with no dust and Doppler taken in account, and with both codes operating on the same 80 transition CO molecular data file by Neufeld (in prep.)).

**Table 2.** “Constant” model results for the  $J = 1 - 0$  transition.

Type of Run	LIME <K>	LVG <K>	RADEX <K>
regular	31.3	36.1	34.8
collision dominated	19.0	19.3	

transitions for the ten shocks, it can be seen that the  $J = 10 - 9$  transition shows the worst agreement between the two codes.

In Fig. 34 the ratios of the CO ladders as computed with LIME and LVG are shown. For every model the LIME and LVG ladders coincide perfectly for  $J_{up}$  ranging from 5 to 15, depending on the specific model. This means that LIME calculates a higher integrated emission in the low  $J$  transitions than LVG and LVG predicts a higher integrated emission in the high  $J$  transitions than LIME. Finally, in Fig. 35 and 36 the contour plots for  $T_{ex15-25}$  and  $T_{ex25-40}$  as computed with LIME and LVG are shown. It can be seen that the LIME contours of  $T_{ex15-25}$  lie consistently above those predicted with LVG by 10 K to 50 K, with the separation between the two increasing for higher  $T_{ex15-25}$  up to a staggering 100 K. Furthermore, the LIME contours of  $T_{ex25-40}$  lie consistently above those predicted with LVG too by 100 K on average. The overall discrepancies between the contours are a direct reflection of the differences in the CO ladders. It can be anticipated from Fig. 34 that the contours would show even larger differences over the  $J_{up} = 1 - 10$  range.

#### 4.3. Discussion

It is necessary to understand the roots of the differences between LIME and LVG fully. Therefore a number of tests are performed and the results are presented below. The first test subject is a so-called “constant” model. The specifics of this “constant model” are those that were used for testing the robustness of LIME in Section 2.3. Namely, a cylinder of the specified dimensions is filled with constant physical parameters and only the velocity varies linearly (see Section 2.3 for the details). Since LVG does not perform calculations in 3D and such a model does not have a dependence on distance (the velocity gradient is constant everywhere), the LVG output consists of one point. LIME still produces a line profile for such a model. The maximum value attained will be quoted here. This “constant model” can be computed in the “regular” modes of both codes, but also under the assumptions of a collision dominated medium. The acquired values are summarized in Table 2 for the  $J = 1 - 0$  transition, in Table 3 for the  $J = 5 - 4$  transition and in Table 4 for the  $J = 10 - 9$  transition. In this table also the RADEX (van der Tak et al. 2007) values have been included for benchmarking purposes, as calculated with the online version. RADEX is another statistical equilibrium radiative transfer code, which is made available for the public on LAMDA (Schöier et al. 2005). It is a 1D non-LTE radiative transfer code, that uses the escape probability formulation assuming an isothermal and homogeneous medium without large-scale velocity fields.

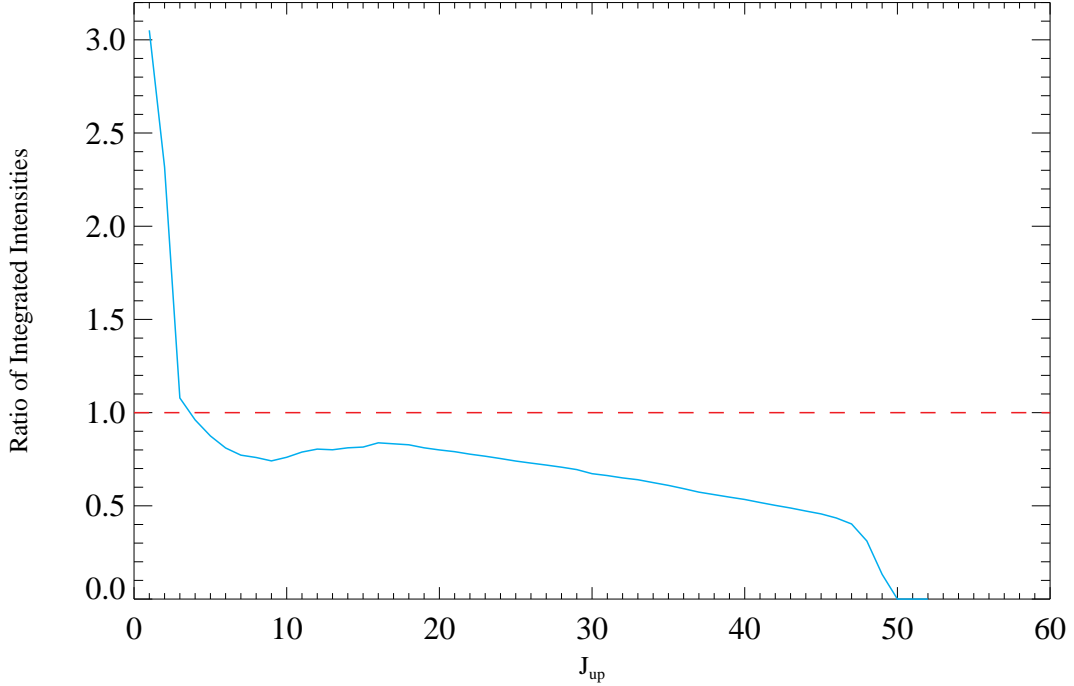


**Fig. 38.** The ratio of the LIME and LVG CO ladder (solid aqua) for the C-type shock model with  $r_{op} = 3.0$ ,  $v_s = 10 \text{ km s}^{-1}$ ,  $n_H = 10^4 \text{ cm}^{-3}$  and  $b = 1.0$  (with no dust and Doppler taken into account, and with both codes operating on the same 80 transition CO molecular data file by Neufeld (in prep.)). The dashed red line corresponds to a perfect match, i.e. a ratio of 1.

**Table 3.** “Constant” model results for the  $J = 5 - 4$  transition.

Type of Run	LIME $\langle K \rangle$	LVG $\langle K \rangle$	RADEX $\langle K \rangle$
regular	61.6	37.7	36.2
collision dominated	81.6	81.9	

**Table 4.** “Constant” model results for the  $J = 10 - 9$  transition.

Type of Run	LIME $\langle K \rangle$	LVG $\langle K \rangle$	RADEX $\langle K \rangle$
regular	1.56201	0.905700	0.7898
collision dominated	56.5876	57.5100	

From the tabulated values it can be seen that there are still discrepancies between the “regular” runs of LIME and LVG. For the  $J = 1 - 0$  transition the two differ by 5 K with LVG providing the higher value, and for the  $J = 5 - 4$  transition the two differ by 24 K with LIME providing the higher value. Meanwhile under the assumption of a collision dominated medium (LTE), the agreement is very good, namely the values do not differ by more than 2 K.

The second test subject is one of the worst models in terms of the agreement between LIME and LVG, namely the C-type shock model with  $r_{op} = 3.0$ ,  $v_s = 10 \text{ km s}^{-1}$ ,  $n_H = 10^4 \text{ cm}^{-3}$  and  $b = 1.0$ , as can be seen from the comparative line profile plots or the comparative integrated intensity plots. The differences between LIME and LVG could arise from the fact that the Doppler broadening is taken into account by LIME. The differences may also stem from the fact that dust is present in the calculations of LIME. Furthermore, the above comparisons between LIME and LVG used different CO data files and this is potential source of variations. For all of the following tests the Doppler  $b$ -parameter was set to  $0 \text{ km s}^{-1}$  and the dust was not taken into account in LIME. LVG has been modified to work with the 80 transition CO data file by Neufeld (in prep.). Thus both LIME and LVG perform computations with the same CO data file in these tests. Individually these tests provide minor improvements in the agreement, but even if all three adjustments are made, the agreement is far from even being consistently within a factor of 2. In Fig. 37 the  $J = 5 - 4$  emission is displayed as calculated by both codes. LVG still overestimates the peak intensity. The location of the peak and the widths of the profiles do agree though. It should be noted that LIME output has been truncated at 25 K from both ends as before. However LVG has been truncated 25 K manually from the pre-shock end and at approximately 35 K at the post-shock end by Gusdorf. However from Section 2.2.1 it is known that this may only influence the  $J = 1 - 0$  transition slightly (by a factor of 2 at most) and the  $J = 5 - 4$  transition will already be essentially unaffected (the ratio of the two profiles at  $T_{\text{trunc}} = 25 \text{ K}$  and  $T_{\text{trunc}} = 35 \text{ K}$  will be 1 to the nearest integer). It is also interesting to note that the third small peak right at  $v_s = 10 \text{ km s}^{-1}$ , that was predicted in Section 3, based on the cooling curves of CO and  $\text{H}_2$ , is indeed visible

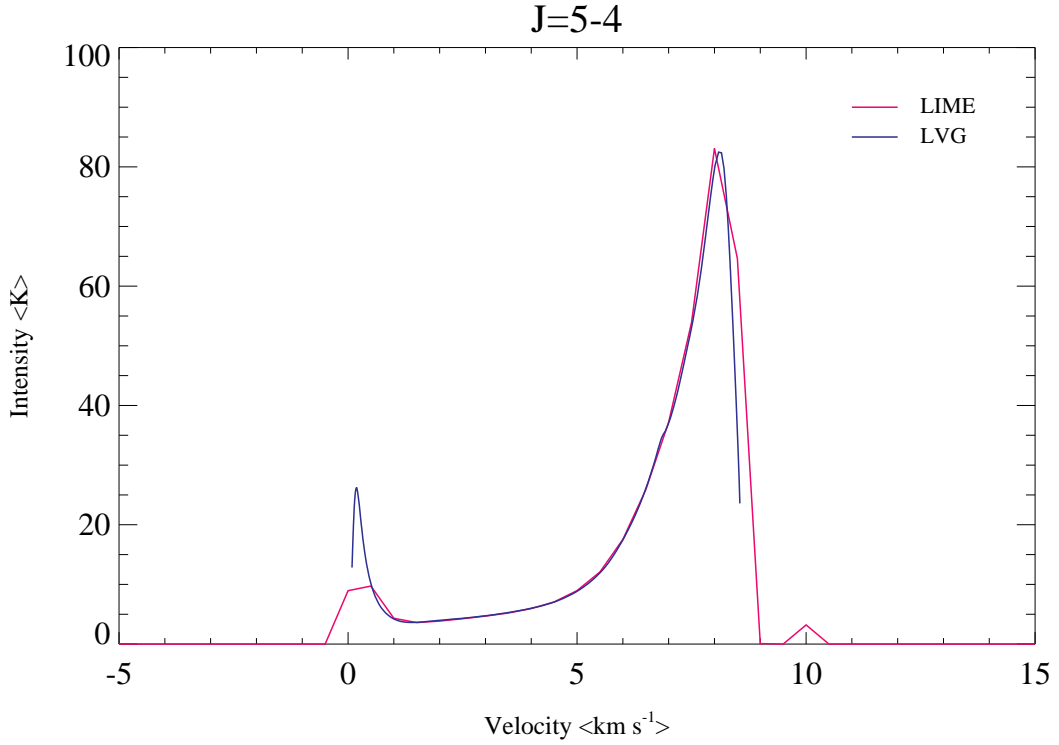


**Fig. 39.** The  $J = 5 - 4$  line profile for the C-type shock model with  $r_{op} = 3.0$ ,  $v_s = 10 \text{ km s}^{-1}$ ,  $n_H = 10^4 \text{ cm}^{-3}$  and  $b = 1.0$  as computed by LIME and LVG (with no dust and Doppler taken into account, and with both codes operating on the same 80 transition CO molecular data file by Neufeld (in prep.)) under the assumption of a collision dominated medium.

here. It was postulated there that it was previously smeared together with the primary emission peak as a result of the Doppler  $b$ -parameter being set to  $1 \text{ km s}^{-1}$ . Since here the Doppler  $b$ -parameter is set to  $0 \text{ km s}^{-1}$ , the peak shows itself. In Appendix G the  $J = 1 - 0$  and the  $J = 10 - 9$  transitions are also given. These three modifications do not result in a better agreement of the CO ladders either, as can be seen from Fig. 38. LIME still predicts a higher integrated emission for low  $J$  levels than LVG and LVG predicts a higher integrated emission for high  $J$  levels than LIME.

Since these adjustments did not resolve the differences between LIME and LVG, it is necessary to investigate further. The same C-type shock model with  $r_{op} = 3.0$ ,  $v_s = 10 \text{ km s}^{-1}$ ,  $n_H = 10^4 \text{ cm}^{-3}$  and  $b = 1.0$  can be computed by both LIME and LVG under the assumption of a collision dominated medium. The same source code modifications are required in LIME as was done for the test of robustness in Section 2.3. In Fig. 39 the  $J = 5 - 4$  emission is displayed as calculated by both codes under the assumption of a collision dominated medium (LTE). It can be seen that the agreement between LIME and LVG is within a factor of roughly 1 in this case for the integrated intensity, improving from a factor of roughly 1.5 in Fig. 37. The peaks coincide not only in location within  $0.2 \text{ km s}^{-1}$ , but also in value within 1 K. The profiles coincide in width within just  $0.5 \text{ km s}^{-1}$  at worst. Only the secondary peak intensities appears to be a factor of 3 higher with LVG. The third one is not reflected by LVG at all. In Appendix G the  $J = 1 - 0$  and the  $J = 10 - 9$  transitions are also given. In Fig. 40 the CO ladders as computed by LIME and LVG under the assumption of a collision dominated medium (LTE) are shown. The agreement is satisfactory here too, namely the ratio lies in the  $[0.5, 1.5]$  range, which is much smaller than the range seen in Fig. 38. This means that the overestimation of either one of the codes over the other is reduced. The CO ladders still do intersect.

From these tests it can be concluded that there are a number of discrepancies between the output of LIME and LVG, which may even be very large for particular shocks and transitions. It seems that there are differences in the way the collisions are treated and in the way the radiation field is computed. The agreement between the two is significantly better under the assumption of a collision dominated medium, i.e. LTE, than for regular runs, so it appears that the differences lie mostly in the way the level populations are calculated, which in turn is determined by the calculation of a photon either being trapped or escaping at a point. The variations persist for the theoretical setups, such as the “constant” model, so not only for shocks. It is unlikely that the differences arise from the inherent randomness of LIME as the constraints on that have been tested in previous sections, i.e. in Section 2.2.3 and 2.2.4. However perhaps for slower shocks the velocity resolution in the LIME code could be set a smaller value (currently  $500 \text{ m s}^{-1}$  is used for all models). Also the cylinder could have been narrower in order to “fit” the spherical computational domain better and thereby avoid empty pixels. Further testing is outside of the timeframe of this research.



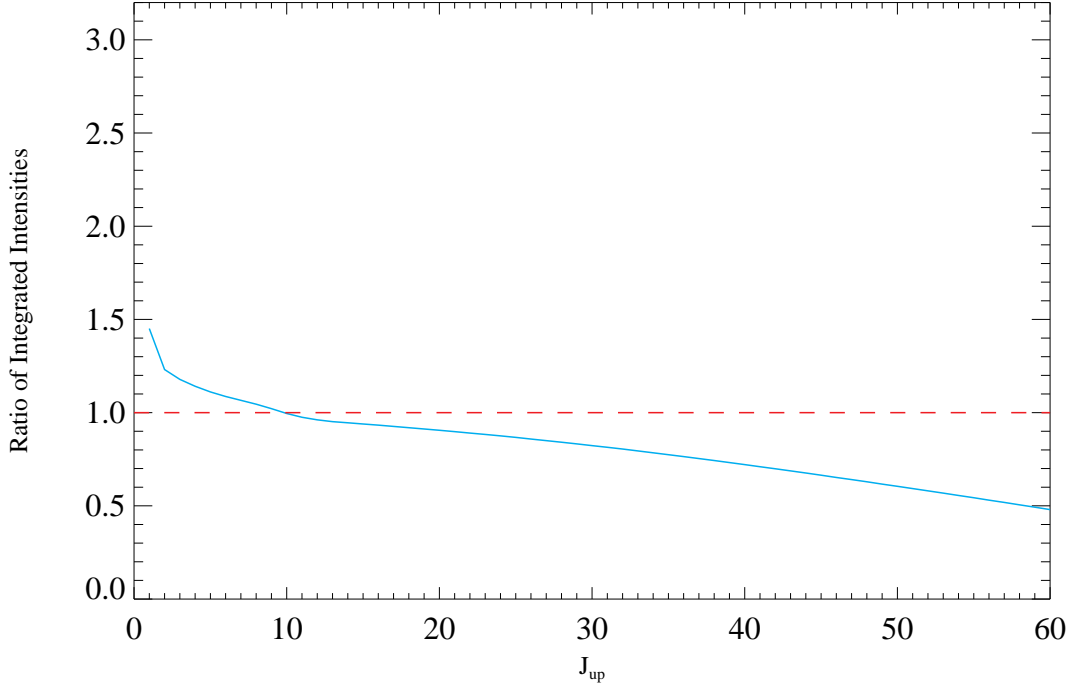


**Fig. 40.** The ratio of the LIME and LVG CO ladder (solid aqua) for the C-type shock model with  $r_{op} = 3.0$ ,  $v_s = 10 \text{ km s}^{-1}$ ,  $n_H = 10^4 \text{ cm}^{-3}$  and  $b = 1.0$  (with no dust and Doppler taken into account, and with both codes operating on the same 80 transition CO molecular data file by Neufeld (in prep.)) under the assumption of a collision dominated medium. The dashed red line corresponds to a perfect match, i.e. a ratio of 1.

## 5. Conclusion

The general aim of this research was to investigate CO emission in shocks. The advanced shock models of Flower and Pineau des Forêts (2003) were used. The emission was computed with LIME (Brinch & Hogerheijde 2010), an excitation and radiation transfer code that has nice model-adaptive characteristics and that performs the computation in 3D. The shocks were investigated as infinite slabs and the first sub-aim of the research was to setup LIME accordingly for the processing of these data. The model data had to be shifted and truncated in the process.

Once the machinery was set up, a batch of over 200 shock models was computed. These were all C-type shocks with  $r_{op} = 3.0$  and  $b = 1.0$ . The line profiles in various CO transitions were investigated. It was established that they were all a reflection of the energetic input of the shock, which is  $\propto v_s^3 \rho$ . The faster the shock, the more emission there is and CO is excited to higher-excitation levels. The denser the pre-shock material, the more emission there is. However the criterion of  $n_{i_{crit}}$  also plays a role in the development of the two trends. Then the CO ladders were considered. They too reflected the energetic input, furthermore, they displayed that CO is primarily a tracer of pre-shock density rather than shock velocity. For rotational diagrams it meant that the more energetic the shock, the more horizontal its curve would be, hence the higher its excitation energy for all transitions. Finally, contour plots of the excitation temperatures  $T_{ex15-25}$  and  $T_{ex25-40}$  were made, which are very useful for observers trying to pin down the pre-shock density from excitation temperatures. Due to CO's apparent indifference to shock velocity, the observer would need to extract a lower bound on the shock velocity from the value at which line profiles peak. It is also possible to extract the pre-shock density from the integrated intensity, however that is less trivial, as exact fitting would be required. Two small observational examples were shown.

Finally, LIME was benchmarked against LVG. The outputs of the two codes were tested on shock models and on a theoretical “constant” model. Furthermore, not only the “regular” runs were compared, but also those under the assumption of the collision dominated medium, i.e. LTE. LIME and LVG do not predict identical emission. In fact, the differences may be quite large for certain shocks and transitions. The rigorous testing showed that the differences persist for the theoretical “constant” model and not only for the shocks, however under LTE the agreement improves. It seems that the greatest differences result from the ways the level populations are computed. Most likely the net variations are a complex combination of the key differences between the operations of the two codes. LIME does have greater potential to be closer to the truth, as the number of assumptions going into it are less and the computations are performed in a more realistic manner (namely, continuously and in 3D).

The growing number of coherent data sets of high CO excitation lines stemming from *ISO* and *Herschel* is calling for sophisticated shock model data to be used in order to generate a grid which analyzes parameter dependences. This would allow an efficient and meaningful way of processing the collected data and any data collected in the future. This research

made the first step in this direction by exploring the dependence on pre-shock-density and shock velocity. Further projects can expand the grid of model and thus make a bigger survey. Furthermore, the same idea can be extended onto other species, providing an even more detailed look at shock diagnostics, in particular  $\text{H}_2\text{O}$ .

## References

- Bachiller, R. & M. Tafalla, 1998, Bipolar Molecular Outflows, Crete II
- Brinch, C., LIME User Manual, Version 1.02 (2011), as seen on <http://www.strw.leidenuniv.nl/~brinch/website/lime.html> on 11 May, 2011
- Brinch, C. & M.R. Hogerheijde, 2010, A & A, 523, A25
- Burlaga, L.F. et al., Nature, 454
- Draine, B.T., 1980, ApJ, 241, 1021
- Draine, B.T., W.G. Roberge & A. Dalgarno, ApJ, 264, 485
- Draine, B.T., 1993, Annu. Rev. Astron. Astrophys., 31, 373
- Dyson, J.E. & D.A. Williams, The Physics of the Interstellar Medium, 1980, Manchester: Manchester University Press
- Flower, D.R., 2001, J. Phys. B, 34, 2731
- Flower, D.R. & G. Pineau des Forêts, 2003, Mon. Not. R. Astron. Soc., 343, 390
- Flower, D.R. & G. Pineau des Forêts, 2010, Mon. Not. R. Astron. Soc., 406, 1745
- Foot, C.J., Atomic Physics, 2005, Oxford: Oxford University Press
- Gaydon, A.G. & W.G. Penney, Proc. Roy. Soc., 1944, 183A
- Guillet, V., 2008, Evolution des Poussières dans les Chocs, PhD thesis, Paris
- Gusdorf, A., 2008, Molecular Emission in Regions of Star Formation, PhD thesis, Paris
- Haas, M. et al, A & A, 433
- Hartigan, P. et al., ApJ, 316
- Hartquist, T.W. & D.A. Williams, The Molecular Astrophysics of Stars and Galaxies, 1998, Oxford: Oxford University Press
- Hollenbach, D., The Physics of Molecular Shocks in YSO Outflows, 1997, Herbig-Haro Flows and the Birth of Stars; IAU Symposium No. 182, 181-198
- Karska, A., G.J. Herczeg et al. (in prep.)
- Kristensen, L.E., 2007, Observational Analysis of the Physical Conditions in Galactic and Extragalactic Active Star Forming Regions, PhD thesis, Paris
- Kristensen, L.E. et al., 2008, A & A, 477, 1
- Lada, C.J., 1998, The Formation of Low Mass Stars: An Observational Overview, Crete II
- Mac Low, M.-M. & R.S. Klessen, 2004, Reviews of Modern Physics, 76, 125
- McKee, C.F. & L.L. Cowie, 1975, ApJ, 195
- Neufeld, D. (in prep.)
- Nisini, B., 2008, IR Spectroscopy of Jets, Lect. Notes Phys., 742
- Ossenkopf & Henning, 1994, A & A, 291, 943
- Ostlie, D.A. & B.W. Carroll, 2007, An Introduction to Modern Stellar Astrophysics, Second Edition, U.S.A.: Pearson Addison Wesley
- Peredo M. et al., 1995, Journal of Geophysical Research, 100, A5
- Rybicki, G.B. & A.P. Lightman, Radiative Processes in Astrophysics, 2004, Weinheim: Wiley-VCH
- Schöier, F.L., van der Tak, F.F.S., van Dishoeck E.F., Black, J.H., 2005, A & A, 432, 369-379
- Snell, R.L. et al., 1980, ApJ, 239, 1
- Stoicheff, B.P., 2001, Canadian Journal of Physics, 79
- van der Tak et al., 2007, A & A, 468, 627
- Tielens, A.G.G.M., The Physics and Chemistry of the Interstellar Medium, 2010, Cambridge: Cambridge University Press
- van Dishoeck, E.F., 2004, Annu. Rev. Astron. Astrophys., 42, 119
- van Dishoeck, E.F. et al., 2011, PASP, 123, 900
- Visser, R. et al. (subm.)
- Wernli M. et al., 2006, A & A, 446, 367
- Yang, B. et al., 2010, ApJ, 718, 1062

## Appendix A: The Detailed LIME Setup.

In this appendix the details of setting up LIME in order to process the shock models will be discussed. It was mentioned that LIME requires one primary input file, which is called `model.c` here. The three types of output files of LIME are called as follows:

1. `grid.vtk`, which is the formatted ASCII file containing the  $(x, y, z)$  coordinate of each grid point, that can be opened by several visualization software packages, such as Paraview;
2. `populations.pop`, which contains the  $(x, y, z)$  coordinate of each grid point alongside the associated  $H_2$  density, kinetic gas density, molecular density and level populations (with respect to  $H_2$  density);
3. `image000.fits`, multiple FITS files containing the image cubes on a velocity scale (numbered accordingly in place of 000).

The task of running LIME on shock models basically comes down to providing LIME with an appropriate `model.c` file. An example of this file is presented in Appendix C and the parameters are discussed below one by one.

1. First up is `par->radius`, this is the radius of the computational domain of LIME. Here it is taken to be the absolute value of the maximal extent of the shock along the  $z$ -axis, in either the positive or negative direction, whichever absolute value is greatest.
2. Secondly, `par->minScale` is the minimal scale that will be sampled by the grid. For the non-shifted data, this corresponds to the  $z$  value at which the shock begins. For the shifted data, this can be set to an arbitrarily small value, here 1 m is used.
3. Thirdly, `par->pIntensity` is the number of grid points that will be spread though the interior of the computational domain. Refer to Section 2.2.3 for further details.
4. Next, `par->sinkPoints` is the number of grid points that will be spread on the boundaries of the computational domain. If a photon reaches a sinkPoint it is said to escape and is not traced any longer. This number needs to be sufficiently large not to cause artifacts in the image and yet small enough to not slow down the gridding too much. Refer to Section 2.2.3 for further details.
5. Then `par->dust` is the path to the dust opacity table. Here the data file from Ossenkopf & Henning (1994) for dust with thin ice mantles with a gas density of  $10^6 \text{ cm}^{-3}$  is used.
6. `par->moldatfile[m]` is the path to the  $m$ th molecular data file, for  $m \in \mathbb{Z}_{\geq 0}$ . Here the CO data file from Neufeld (in prep.) is used.
7. `par->outputfile` is the name of the file that will contain the level populations.
8. `par->sampling` can be set to either 0 for uniform sampling in  $\log(\text{par->radius})$  or 1 for uniform sampling along all axes. Here 1 is used for all models.

Next come the parameters for `img[i]`, the  $i$ th FITS file containing the  $i$ th image cube. Here  $i$  corresponds to the transition down to the  $i$ th level.

1. `nchan` is the number of velocity channels in a spectral image cube. `velres` is the velocity resolution of the spectral dimension of the FITS file (the width of a velocity channel) in  $\text{m s}^{-1}$ . Here `velres` is set to  $500 \text{ m s}^{-1}$  for all models. `nchan` therefore needs to vary with  $v_s$  in order to accommodate for the various shock velocities analyzed. It is calculated with the following formula

$$\text{nchan} = 2 \frac{v_s + 5000}{\text{velres}} + 1 \quad (\text{A.1})$$

where both  $v_s$  and `velres` need to be given in  $\text{m s}^{-1}$ . In this equation the number of channels required to cover  $v_s$  and an additional  $5000 \text{ m s}^{-1}$  with the prescribed channel resolution is calculated. The multiplication by 2 is necessary to account for the negative and positive directions, and finally 1 is added to make the number odd. It is desirable to make this number odd so that the central velocity channel exists.

2. `trans` is the transition number for the image is to be constructed; it needs to correspond to the transition number in the appropriate molecular data file. The suitable number is  $i$ .
3. `pxls` is the number of pixels per spatial dimension of the FITS file. The total number of pixels in the image is thus the square of this number. Here it is set to 11 for all models. See Section 2.2.4 for justification.
4. `imgres` is the image resolution of each pixel in arc seconds. See below for an explanation.
5. `theta` is the viewing angle, i.e. the angle between the model  $z$ -axis and the ray-tracers' line of sight, in radians. Face-on view corresponds to 0 and edge-on view to  $\pi/2$ . Here the face-on view is adapted for all models.
6. `distance` is the distance to the source from the observer. Here it is set to 100 pc for all models.
7. `source_vel` is the source velocity. Here it is set to 0 for all models.
8. `unit` is the unit of the image. Four values are allowed: 0 for Kelvin, 1 for Jansky per pixel, 2 for SI units and 3 for Solar luminosity per pixel. Here Kelvin is always used.
9. `filename` is the name of the FITS file to be created.

After these two sets of parameters, it is necessary to supply five main functions with data. This is also where the cylinder mentioned earlier, is prescribed to LIME.

First up is the density function, which requires the number densities of the collision partners. Here one single collision partner is considered, namely  $H_2$ , both para- and ortho- flavors together. In the first line it says to include another file called `density.h`. This is a C header file, it contains three declarations:

1. integer `nval`, which is the number of shock data points left after truncation;
2. float array `dist` of size `nval`, which contains the shifted  $z$  values of the shock data points left after truncation;
3. float array `dens` of size `nval`, which contains the  $H_2$  density values left after truncation.

In the second and third lines two integer variables and two double variables are declared, which will be needed later on. In the fourth line the switch is made from the shock traveling in the positive  $z$  direction to it traveling in the negative  $z$  direction. Now finally comes the if statement that prescribes the cylinder. The statement says that points outside of the cylinder will be given a density equal to 0 and that points inside the cylinder will be given a density computed by logarithmic interpolation.<sup>1</sup> Consider the else part of the statement in more detail. LIME has generated a random point  $(x, y, z)$ , suppose that it happens to belong to the interior of the cylinder. The point's  $z$  coordinate will not necessarily match a  $z$  value of a data point from `dist`, however it will certainly lie between some two of its values. By means of a for loop through all the available  $z$  values of data points and an if statement, the nearest neighbors of the point's  $z$  coordinate, namely `dist[i]` and `dist[i+1]`, are determined. This `i` value is stored in `index`. Then `feps` is calculated corresponding to this `index`. `feps` is the ratio of the logarithm of the distance separating the point's  $z$  coordinate and neighbor `dist[i]` and the logarithm of the distance separating neighbor `dist[i+1]` and the point's  $z$  coordinate. Notice the need to convert here to the non-shifted  $z$  values by equation 2.2.2 in order to avoid taking the logarithm of negative numbers. Next comes another if statement that double checks that `feps` was computed correctly, i.e. whether `feps`  $\in [0, 1]$ , which follows from the way it is defined. Then the value of `feps` is used to get the interpolated value for the density, a value which lies between the density at `dist[i]` and the density at `dist[i+1]`. There is still the need to take the exponential due to the previous use of logarithms and that is how `dnst` is acquired. In the final line we set `density[0]`, which is the number density of the 0th collision partner that LIME requires, equal to `dnst`.

Second up is the temperature function, which requires the kinetic gas temperature to equal `temperature[0]` and the dust temperature to equal `temperature[1]`. The kinetic gas temperature calculation is done exactly as it was for density with `temp` instead of `dens` (including a different `temperature.h` C header file naturally) and `gastemp` instead of `dnst`. The dust temperature is set to a constant 15 K, a typical value for the dust in the ISM. In principle, the dust temperature is optional, however if it is not set, then LIME assumes that it is equal to the gas temperature. This is undesirable for the context of shocks.

Third up is the abundance function, which requires the fractional abundance of CO (the molecule that is studied here) with respect to the primary collision partner (`density[0]`), which is  $H_2$  here. The abundance calculation is done exactly as it was for density with `abun` instead of `dens` (including a different `abundance.h` C header file naturally) and `abnd` instead of `dnst`.

Next is the doppler function, which requires Doppler  $b$ -parameter, which is the  $1/e$  half-width of the line profile. It is fair to take a constant Doppler broadening everywhere and so here `*doppler` was set to  $1000 \text{ m s}^{-1}$  for all models.

Finally, comes the velocity function, which requires the velocity of CO (the molecule that is studied here). The calculation is done exactly as it was for density with `velo` instead of `dens` (including a different `velocity.h` C header file naturally) and `vlct` instead of `dnst`. The calculated value is then set for `vel[2]`, i.e. the velocity along the  $z$ -axis, which corresponds to the setup of the shock travelling along the  $z$ -axis. The velocities along the  $x$  and  $y$  axes, i.e. `vel[0]` and `vel[1]` respectively, are set to 0. In the final line the transformation from the reference frame of the shock front to the reference frame of the observer is performed.

It is still necessary to address the dimensions of the cylinder. In the shifted situation, it is centered about the origin, so `par->radius` is taken here to be half the length of the cylinder. This means that the cylinder and the spherical computational domain share the  $z$  axis. It is necessary for the cylinder to occupy a sufficiently large volume of the sphere in order to contain as many grid points as possible (without the need to increase the total number of grid points too much causing a much longer computational time). However, on the other hand, it should not stick out of the sphere too much and thus leave out data points. So the definition of the radius needs to be a balance between these two considerations. Here the following formula was used based on various tests:

$$\text{cylinder radius} = \frac{\text{cylinder length}}{25} \quad (\text{A.2})$$

where cylinder length equals the value set for `par->radius`, as just explained.

Now there is still the question of `imgres`. The determination of this comes down to realizing that the image box of  $11^2$  pixels needs to be within the interior of a circular cross-sectional area of the cylinder in order to avoid the edge effects, such as the ones that caused the “artificial feature”. The idea of the edge effects here is precisely the same, namely Voronoi cells that lie partially inside and partially outside the cylinder. However, on the other hand, the image should cover as much of the circular cross-section area as possible in order to consider as many data points as possible. Once again the two factors need to be balanced and so it was decided to go for the exactly inscribed image box. Since the diagonal of a square is  $\sqrt{2} \cdot \text{side of the box}$  and the diameter of a circle is  $2 \cdot \text{radius of the circle}$ , equating the two yields that side of the box  $= \frac{\sqrt{2}}{2} \cdot \text{radius of the circle}$ . Thus the side of one pixel will be  $\frac{\sqrt{2}}{\sqrt{2 \cdot 11}} \cdot \text{radius of the circle}$ , because there

<sup>1</sup> In principle, linear interpolation will do that job just as well here. However, in the non-shifted situation, the use of logarithmic interpolation is obligatory. In general, the type of interpolation required is determined by whether the plot of the two variable being involved in the integration gives a straight line in lin-lin, lin-log, log-lin or log-log space.

are 11 pixels along each axis always (see `pxls`). The resolution needs to equal side of one pixel/100 < pc >, because 100 pc is the distance from the source to the observer (see `distance`). This boils down to the following formula

$$\text{imgres} = \frac{2}{\sqrt{2} \cdot 11 \cdot 100 < \text{pc} >} \text{cylinder radius} \quad (\text{A.3})$$

where cylinder radius is prescribed by equation A.2.

Note that all physical numbers in this input file must be given in SI units (with a single exception for the dust opacity table). Also note that LIME has conversion definitions for pc and AU, so it's possible to use those units in the `model.c` file directly, as long as they are explicitly prescribed then. There are still three more parameters that require awareness. In Section 1.6 it was stated that photon propagation is an iterative process. The number of iterations performed is user defined. It can be set in the `src` directory in file `lime.h` on line 41 by changing the value of `Niterations`. Here 15 is used for all models, which leads to minimum SNR values over a 100 and median SNR values of several thousand, generally. Another handy parameter is defined on line 24 in the same file. It is called `silent` and if it's set to 1 instead of the default 0, then the visualization of LIME is turned off. Otherwise when LIME is running a visualization of the progress appears in the terminal window. Finally, in the directory `src` in the file `weights.c` the user specifies how the weighting of the random grid points is done, this was mentioned in step 2 of Section 1.6. There are two options, either sample according to density or according to temperature. In the context of shocks sampling according to temperature is much more appropriate, and was done so here, because then the sampling of the peak in the temperature profiles of shocks is assured to be good. This means that few of the lines in this file need to be changed, in Appendix D the modified file is presented.

In this research LIME needs to be run on a batch of over 200 shock models, therefore an automated process has been developed. It consists of a main IDL procedure file `shock_run.pro` and a template model file for LIME called `model.tmpl`. These two files can be found in Appendix B and C respectively. It is also possible to run LIME in a special LTE mode, by include the line `par->lte_only = 1` immediately after the line when `par->sampling` is specified. If this parameter is set than LIME performs an LTE calculation, which may be useful for quick checks.

Now it is necessary to extract the appropriate shock model data from the output of the MHD simulation by Flower and Pineau des Forêts (2003). Two files are of primary interest here, namely `mhd\_phys.out` and `mhd\_speci.out`. These two files contain all the relevant physical data in ASCII format along the entire extent of the shock. The calculations of the MHD simulations were performed in the reference frame of the shock front, which is moving along the positive  $z$  axis. Therefore the above mentioned reference frame modifications had to occur in the input file of LIME. The following data are necessary for LIME:

1. distance along the extend of the shock, i.e. the  $z$  coordinate, which is found in the 1st column of `mhd\_phys.out`, unit conversion from cm to m is required;
2.  $v_n$ , which is found in the 6th column of `mhd\_phys.out`, unit conversion from  $\text{cm s}^{-1}$  to  $\text{m s}^{-1}$  is required;
3.  $T_n$ , which is found in the 8th column of `mhd\_phys.out`, no unit conversion is required;
4.  $n_{\text{H}_2} = x(\text{H}_2) \cdot n_{\text{H}}$ , which implies the multiplication of the 4th and 6th columns of `mhd\_speci.out`, unit conversion from  $\text{cm}^{-3}$  to  $\text{m}^{-3}$  is required;
5. fractional abundance of CO with respect to  $\text{H}_2$ , equal to  $2 \cdot x(\text{CO})$ , implies the multiplication of the 17th column of `mhd\_speci.out` with 2, no unit conversion required.

Later on the cooling information is used too, it can be found in the output file `cooling.out`, in columns 5 and 4 respectively.

## Appendix B: The shock\_run.pro File.

```
pro shock_run

;make an array with all the file names
dummy=rascii('noncrit_op30_b10.txt', head=dir)

;find the number of models
nmodels=n_elements(dir(*))

for i=0, nmodels-1, 1 do begin

model_name_i=dir(i)

print,model_name_i

;read in relevant data files
mhd_phys_i=rascii('/disks/chem6/models/shocks/b10/'+model_name_i+'/mhd_phys.out')
mhd_speci_i=rascii('/disks/chem6/models/shocks/b10/'+model_name_i+'/mhd_speci.out')

;find the number of data points
nrows=n_elements(mhd_phys_i(0,*))

;define the constant truncation temperature
T_trunc=25.

;find from which and to which data point index lies the data above the truncation temperature
;temperature of neutrals is in the 7th column
for j=1, nrows-2, 1 do begin
  if mhd_phys_i(7,j-1) lt T_trunc && mhd_phys_i(7,j) ge T_trunc then begin
    nfrom=j+1
  endif
  if mhd_phys_i(7,j) ge T_trunc && mhd_phys_i(7,j+1) lt T_trunc then begin
    nto=j
  endif
endfor

;calculate the number of data points above the truncation temperature
nvalues=nto-nfrom+1

;create an Output folder
spawn, 'mkdir Output_'+model_name_i
spawn, 'cp -f co@neufeld.dat Output_'+model_name_i+'/'
spawn, 'cp jena_thin_e6.tab Output_'+model_name_i+'/'

;calculate the parameters needed in the model.c in the appropriate units

;the maximum shifted distance that the shock reaches is required here
shocklength=(mhd_phys_i[0,nto]-0.5*(mhd_phys_i[0,nfrom]+mhd_phys_i[0,nto]))*0.01

;shock velocity is the first value of velocity of neutrals in <cm s-1>
shockvelocity=mhd_phys_i[5,0]*0.01

;define constant in <m s-1>, same as specified in the model.tmp1
channelresolution=500

;(shockvelocity+5e3)/channelresolution is the number of channels required to cover the
;positive direction of the shock velocity plus an extra 5e3 km s-1
;multiply by 2 to account for the negative direction too and add 1 to make the channel number odd
numberofchannels=round(2*(shockvelocity+5e3)/channelresolution+1)

;the maximum and minimum un-shifted distances that the shock covers are required here
minoriginalshockdistance=mhd_phys_i[0,nfrom]*0.01
maxoriginalshockdistance=mhd_phys_i[0,nto]*0.01
```

```

;convert the shock length from <m> to <AU> and divide by a ratio, which was prior calculated
;to be optimal in avoiding edge effects
cylinderradius=shocklength*6.68458134e-12/25

;define constant in <pc>, same as specified in the model.tmpl
distanceaway=100.

;define constant, same as specified in the model.tmpl
numberpixels=11.

;pixel resolution <'>=(side of 1 pixel in <AU>)/(distance away <pc>)
;side of 1 pixel=(side of the inside box)/(number of pixels per dimension)
;side of the inside box=(cylinder radius)*2/sqrt(2), this is coming from formulas
;about inscribed squares in circles
pixelresolution=2*cylinderradius/(sqrt(2.)*numberpixels*distanceaway)

;create the model.c file for the specific shock, i.e. substitute the appropriate parameters

;define the keywords needed in the model.c and their respective values (must be defined as strings)
;let each keyword occupy 25 character positions, add s after each name to compensate
keyword1='ShockLengthssssssssssssssss'
keyword2='NumberOfChannelssssssssssss'
keyword3='ShockVelocityssssssssssssss'
keyword4='MinOriginalShockDistances'
keyword5='MaxOriginalShockDistances'
keyword6='PixelResolutionssssssssssss'
keyword7='CylinderRadiusssssssssssss'

value1=string(shocklength, format='(e25.3)')
value2=string(numberofchannels, format='(i25)')
value3=string(shockvelocity, format='(i25)')
value4=string(minoriginalshockdistance, format='(e25.3)')
value5=string(maxoriginalshockdistance, format='(e25.3)')
value6=string(pixelresolution, format='(e25.3)')
value7=string(cylinderradius, format='(e25.3)')

;open the template model.tmpl file that has the keywords
openr, 1, 'model.tmpl'
;open the model.c file that LIME will be using
openw, 2, 'model.c'

;create string dummy for a line, assuming there will be no more than
;300 characters per line in the model.tmpl
dum=string(300)

;copy a line from the model.tmpl into variable dum, check it for keywords,
;replace keywords with values if found, print dum into the model.c
;do this for every line, assuming there will be no more than 1000 lines in the model.tmpl
for k=0, 1000 do begin
  if eof(1) ne 1 then begin ;check that the end of the file with unit = 1 has not been reached
    readf, 1, dum
    while ((t = strpos(dum, keyword1)) ne -1) do strput, dum, value1, t
    while ((t = strpos(dum, keyword2)) ne -1) do strput, dum, value2, t
    while ((t = strpos(dum, keyword3)) ne -1) do strput, dum, value3, t
    while ((t = strpos(dum, keyword4)) ne -1) do strput, dum, value4, t
    while ((t = strpos(dum, keyword5)) ne -1) do strput, dum, value5, t
    while ((t = strpos(dum, keyword6)) ne -1) do strput, dum, value6, t
    while ((t = strpos(dum, keyword7)) ne -1) do strput, dum, value7, t
    printf, 2, dum
  endif
endfor

```



```

;close both files
close,1
close,2

;move the created model.c file into the appropriate folder
spawn, 'mv -f model.c Output_'+model_name_i+'/'

;create header files (the .h input files) and place the relevant data in the correct units into them

;distance is in the 0th column, unit conversion from <cm> to <m> required
;shifting is required to avoid edge effects of LIME, like this the range of the shock
;s symmetric about the origin
dist=string((mhd_phys_i[0,nfrom]-0.5*(mhd_phys_i[0,nfrom]+mhd_phys_i[0,nto]))*0.01, $
format='(e10.3)')
for k=1, nvalues-1, 1 do begin
    dist=dist+', '+string((mhd_phys_i[0,nfrom+k]-0.5*(mhd_phys_i[0,nfrom]+mhd_phys_i[0,nto]))*0.01, $
format='(e10.3)')
endfor

;velocity of neutrals is in the 5th column, unit conversion from <cm s-1> to <m s-1> required
velo=string(mhd_phys_i[5,nfrom]*0.01, format='(e10.3)')
for k=1, nvalues-1, 1 do begin
    velo=velo+', '+string(mhd_phys_i[5,nfrom+k]*0.01, format='(e10.3)')
endfor

;temperature of neutrals is in the 7th column, no unit conversion required
temp=string(mhd_phys_i[7,nfrom], format='(e10.3)')
for k=1, nvalues-1, 1 do begin
    temp=temp+', '+string(mhd_phys_i[7,nfrom+k], format='(e10.3)')
endfor

;density of H2=x(H2)*n(H), unit conversion from <cm-3> to <m-3> required
;x(H2) is the relative abundance of H2 with respect to H in arbitrary units
;and it is in the 5th column
;n(H) is the density of H in <cm-3> and it is in the 3rd column
dens=string(mhd_speci_i[5,nfrom]*mhd_speci_i[3,nfrom]*1e6, format='(e10.3)')
for k=1, nvalues-1, 1 do begin
    dens=dens+', '+string(mhd_speci_i[5,nfrom+k]*mhd_speci_i[3,nfrom+k]*1e6, format='(e10.3)')
endfor

;relative abundance of CO with respect to H2=x(CO)*2
;x(CO) is the relative abundance of CO with respect to H in arbitrary units and it is
;in the 16th column
abun=string(mhd_speci_i[16,nfrom]*2, format='(e10.3)')
for k=1, nvalues-1, 1 do begin
    abun=abun+', '+string(mhd_speci_i[16,nfrom+k]*2, format='(e10.3)')
endfor

openw, 1, 'velocity.h'
printf, 1, 'int nval = '+string(nvalues)+';'
printf, 1, 'float dist['+string(nvalues)+'] = {'+dist+'}; //distance in m'
printf, 1, 'float velo['+string(nvalues)+'] = {'+velo+'}; //velocity of neutrals in meters per second'
close, 1

openw, 1, 'temperature.h'
printf, 1, 'int nval = '+string(nvalues)+';'
printf, 1, 'float dist['+string(nvalues)+'] = {'+dist+'}; //distance in m'
printf, 1, 'float temp['+string(nvalues)+'] = {'+temp+'}; //temperature of neutrals in Kelvin'
close, 1

openw, 1, 'density.h'
printf, 1, 'int nval = '+string(nvalues)+';'
printf, 1, 'float dist['+string(nvalues)+'] = {'+dist+'}; //distance in m'
printf, 1, 'float dens['+string(nvalues)+'] = {'+dens+'}; //density of neutrals per cubic meter'

```

```

close, 1

openw, 1, 'abundance.h'
printf, 1, 'int nval = '+string(nvalues)+';'
printf, 1, 'float dist['+string(nvalues)+'] = {'+dist+'}; //distance in m'
printf, 1, 'float abun['+string(nvalues)+'] = {'+abun+'}; //relative abundance in arbitrary units'
close, 1

spawn, 'mv -f velocity.h Output_'+model_name_i+'/'
spawn, 'mv -f temperature.h Output_'+model_name_i+'/'
spawn, 'mv -f density.h Output_'+model_name_i+'/'
spawn, 'mv -f abundance.h Output_'+model_name_i+'/'

;move to the Output folder and run LIME and (automatically) leave the Output folder upon completion
spawn, 'cd Output_'+model_name_i+'; lime model.c'

;define a means of skipping bad runs
counter=0.

while file_test('Output_'+model_name_i+'/image079.fits') eq 0 do begin
  if counter lt 180 then begin
    wait, 60
    counter=counter+1
  endif
endwhile

print, 'Success!'

endfor

end

```

## Appendix C: The model.tmpl File.

```
/*
 * model.tmpl
 */

#include "lime.h"

/*****/

void
input(inputPars *par, image *img)
{
    par->radius = ShockLengthssssssssssssss;
    par->minScale = 1.;
    par->pIntensity = 3000;
    par->sinkPoints = 2000;
    par->dust = "jena_thin_e6.tab";
    par->moldatfile[0] = "co@neufeld.dat";
    par->outputfile = "populations.pop";
    par->sampling = 1;

    int i;

    for (i=0; i<80; i++)
    {
        img[i].nchan = NumberOfChannelssssssssss;
        img[i].velres = 500.;
        img[i].trans = i;
        img[i].pxls = 11;
        img[i].imgres = PixelResolutionssssssssss;
        img[i].theta = 0.0;
        img[i].distance = 100*PC;
        img[i].source_vel = 0;
        img[i].unit = 0;
        img[i].filename = malloc(26*sizeof(char));
        sprintf(img[i].filename, "image%03d.fits", i);
    }
}

/*****/

void
density(double x, double y, double z, double *density)
{
    #include "density.h"
    int i,index;
    double feps,dnst;

    z=-z;

    if(z<dist[0] || z>dist[nval-1] || sqrt(x*x+y*y)>CylinderRadiussssssssss*AU)
    {
        dnst = 0.;
    }
    else
    {
        /*Get the density of H2 by interpolation.*/
        for(i=0;i<=nval-2;i++)
        {
            if(z>=dist[i] && z<dist[i+1])
            {
                index=i;
            }
        }
    }
}
```

```

    }
    feps = (log(z+0.5*(MinOriginalShockDistances+MaxOriginalShockDistances))-log(dist[index]
+0.5*(MinOriginalShockDistances+MaxOriginalShockDistances))) /
(log(dist[index+1]+0.5*(MinOriginalShockDistances+MaxOriginalShockDistances))
-log(dist[index]+0.5*(MinOriginalShockDistances+MaxOriginalShockDistances)));
    if(feps<0.0 || feps>1.0)
    {
        endwin();
        printf("Error in function 'density'\n%i %e %e %e %e\n",index,feps,z,dist[index],dist[index+1]);
        exit(0);
    }
    dnst = (1.0-feps)*log(dens[index]) + feps*log(dens[index+1]);
    dnst = exp(dnst);
}

density[0] = dnst; //para- and ortho-H2 together
}

/*****/

void
temperature(double x, double y, double z, double *temperature)
{
    #include "temperature.h"
    int i,index;
    double feps,gastemp;

    z=-z;

    if(z<dist[0] || z>dist[nval-1] || sqrt(x*x+y*y)>CylinderRadiusssssssssss*AU)
    {
        gastemp = 1.;
    }
    else
    {
        /*Get the gas temperature by interpolation.*/
        for(i=0;i<=nval-2;i++)
        {
            if(z>=dist[i] && z<dist[i+1])
            {
                index=i;
            }
        }
        feps = (log(z+0.5*(MinOriginalShockDistances+MaxOriginalShockDistances))-log(dist[index]
+0.5*(MinOriginalShockDistances+MaxOriginalShockDistances))) /
(log(dist[index+1]+0.5*(MinOriginalShockDistances+MaxOriginalShockDistances))
-log(dist[index]+0.5*(MinOriginalShockDistances+MaxOriginalShockDistances)));
        if(feps<0.0 || feps>1.0)
        {
            endwin();
            printf("Error in function 'temperature'\n%i %e %e %e %e\n",index,feps,z,dist[index],dist[index+1]);
            exit(0);
        }
        gastemp = (1.0-feps)*log(temp[index]) + feps*log(temp[index+1]);
        gastemp = exp(gastemp);
    }

    temperature[0] = gastemp;
    temperature[1] = 15.;
}

/*****/

void

```

```

abundance(double x, double y, double z, double *abundance)
{
    #include "abundance.h"
    int i,index;
    double feps,abnd;

    z=-z;

    if(z<dist[0] || z>dist[nval-1] || sqrt(x*x+y*y)>CylinderRadiusssssssssss*AU)
    {
        abnd = 0.;
    }
    else
    {
        /*Get the relative abundance by interpolation.*/
        for(i=0;i<=nval-2;i++)
        {
            if(z>=dist[i] && z<dist[i+1])
            {
                index=i;
            }
        }
        feps = (log(z+0.5*(MinOriginalShockDistances+MaxOriginalShockDistances))-log(dist[index]
        +0.5*(MinOriginalShockDistances+MaxOriginalShockDistances))) /
        (log(dist[index+1]+0.5*(MinOriginalShockDistances+MaxOriginalShockDistances))
        -log(dist[index]+0.5*(MinOriginalShockDistances+MaxOriginalShockDistances)));
        if(feps<0.0 || feps>1.0)
        {
            endwin();
            printf("Error in function 'abundance'\n%i %e %e %e %e\n",index,feps,z,dist[index],dist[index+1]);
            exit(0);
        }
        abnd = (1.0-feps)*log(abun[index]) + feps*log(abun[index+1]);
        abnd = exp(abnd);
    }

    abundance[0] = abnd;
}

/*****/

void
doppler(double x, double y, double z, double *doppler)
{
    *doppler = 1000.;
}

/*****/

void
velocity(double x, double y, double z, double *vel)
{
    #include "velocity.h"
    int i,index;
    double feps,vlct;

    z=-z;

    if(z<dist[0] || z>dist[nval-1] || sqrt(x*x+y*y)>CylinderRadiusssssssssss*AU)
    {
        vlct = 0.;
    }
    else
    {

```

```

/*Get the velocity by interpolation.*/
for(i=0;i<=nval-2;i++)
{
    if(z>=dist[i] && z<dist[i+1])
    {
        index=i;
    }
}
feps = (log(z+0.5*(MinOriginalShockDistances+MaxOriginalShockDistances))-log(dist[index]
+0.5*(MinOriginalShockDistances+MaxOriginalShockDistances))) /
(log(dist[index+1]+0.5*(MinOriginalShockDistances+MaxOriginalShockDistances))
-log(dist[index]+0.5*(MinOriginalShockDistances+MaxOriginalShockDistances)));
if(feps<0.0 || feps>1.0)
{
    endwin();
    printf("Error in function 'velocity'\n%i %e %e %e %e\n",index,feps,z,dist[index],dist[index+1]);
    exit(0);
}
vlct = (1.0-feps)*log(velo[index]) + feps*log(velo[index+1]);
vlct = exp(vlct);
}

vel[0] = 0.;
vel[1] = 0.;
vel[2] = vlct;
vel[2] = -vel[2] + ShockVelocityssssssssssss;
}

/*****/

```

## Appendix D: The weights.c File Modified for Sampling According to Temperature.

```
/*
 * weights.c
 * weighting according to temperature
 */

#include "lime.h"

int
pointEvaluation(inputPars *par, double ran, double x, double y, double z)
{
    double logminTemp, logmaxTemp, weight1, val[2];

    logminTemp=log10(5.);
    logmaxTemp=log10(2000.);
    temperature(x,y,z,val);
    weight1=(log(val[0])-logminTemp)/(logmaxTemp-logminTemp);

    if(ran < weight1) return 1;
    else return 0;
}
```

## Appendix E: The Detailed LIME Setup for the Robustness Test.

In this appendix the details of the setup used when testing the robustness of LIME are listed.

1. `par->radius` is set to  $5 \cdot 10^{15}$  m;
2. `par->minScale` is set to 1 m;
3. `par->pIntensity` is set to 3000;
4. `par->sinkPoints` is set to 2000;
5. `par->dust` is linked to the data file from Ossenkopf & Henning (1994) for dust with thin ice mantles with a gas density of  $10^6 \text{ cm}^{-3}$  is used;
6. `par->moldatafile[m]` is still linked to the CO data file from Neufeld (in prep.);
7. `par->outputfile` is just arbitrarily up to the user;
8. `par->sampling` is set to 1;
9. `nchan` is set to 61 (according to equation A.1);
10. `velres` is set to  $500 \text{ m s}^{-1}$ ;
11. `trans` is set to `i`;
12. `pxls` is set to 11;
13. `imgres` is set to 3.6" (according to equation A.3);
14. `theta` is set to 0;
15. `distance` is set to 100 pc;
16. `source_vel` is set to  $0 \text{ m s}^{-1}$ ;
17. `unit` is set to 0;
18. `filename` is just arbitrarily up to the user.

The Doppler broadening is still set to  $1000 \text{ m s}^{-1}$ . The parameters for the other four functions are specified similarly to the way they are in Appendix C. The same if and else statement is used to prescribe the cylinder, however instead of any interpolation, a constant value is set and for the case of velocity: `vel[2]=1.e-12*z+5000.` and the other two components set to 0.

In order to perform the two tests at question, the source code of LIME needs to be modified. It essentially comes down to the following. For the radiation dominated mode, all collisional rate coefficients are set to zero right after they are read in from the data file (`molinit.c`). The analogous trick for the collision dominated mode is to set the Einstein *A* coefficients to zero. That works for the level populations, but has the side effect of giving zero intensities in the FITS image cubes. Instead, a few lines are disabled where the radiation field is added to the matrix used in solving the statistical equilibrium (`stateq.c`).



## Appendix F: The Analysis of Trends in the Maximum and Integrated Intensities for the $J = 1 - 0$ Transition.

In this appendix the maximum values and the integrated values of the  $J = 1 - 0$  transition for all the shock models computed are shown. The dependence of the two on the shock velocity and the pre-shock density is explored, as well as that of their ratio. However no clear trends are observed in these. Similar plots can be made for other transitions too, but they do not differ significantly and do not display any clear trends either.

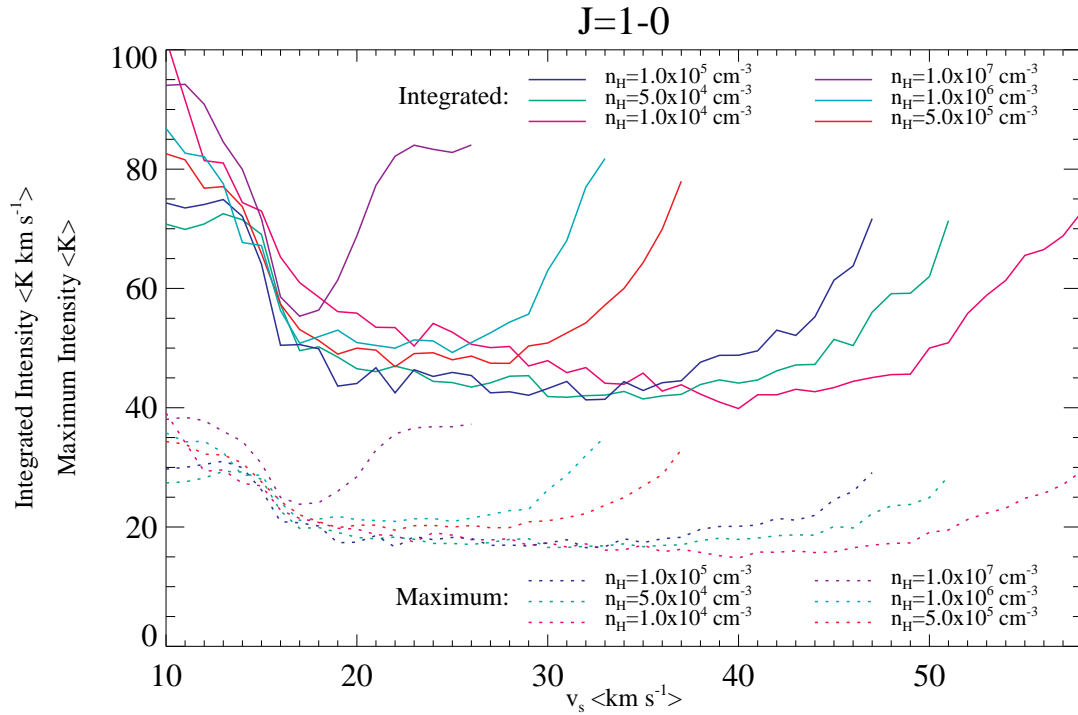


**Fig. F.1.** The maximum intensity and the integrated intensity as a function of the shock velocity for various densities.

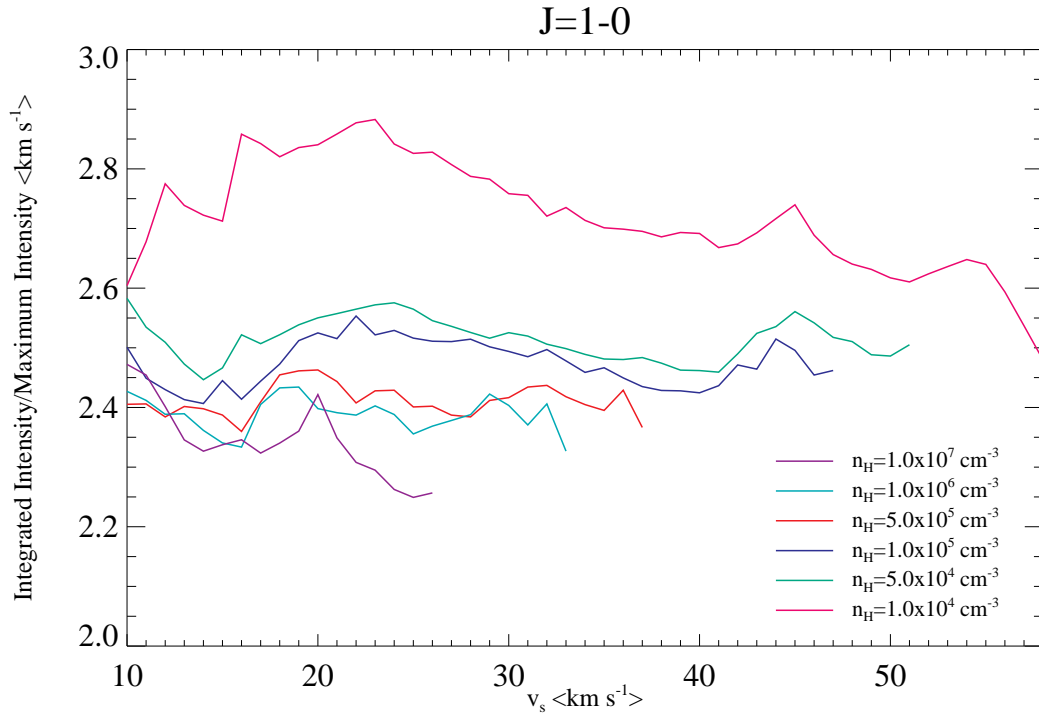


**Fig. F.2.** The ratio of the integrated intensity to the maximum intensity as a function of the shock velocity for various densities.

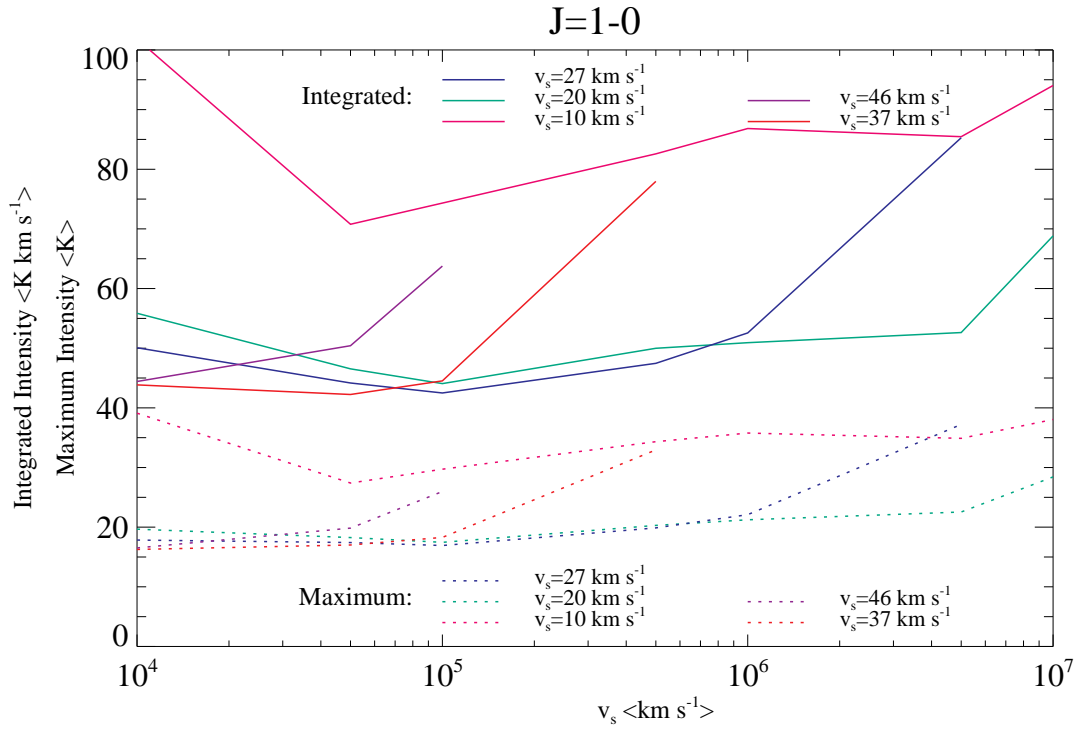


**Fig. F.3.** The maximum intensity and the integrated intensity as a function of the density for five shock velocities.

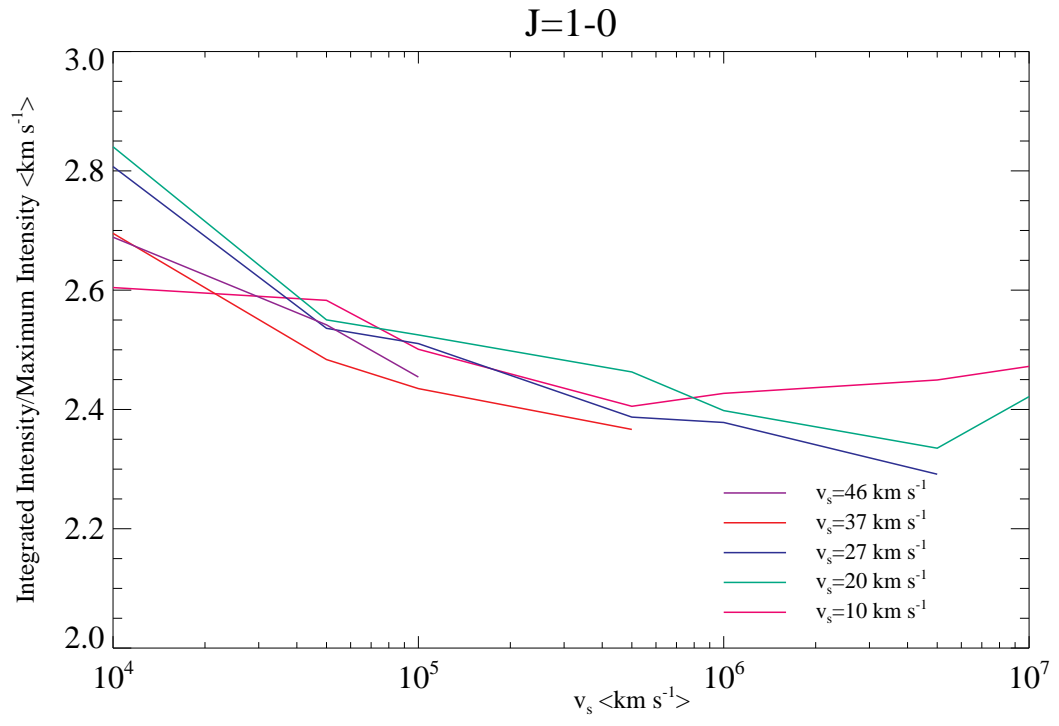


**Fig. F.4.** The ratio of the integrated intensity to the maximum intensity as a function of the density for five shock velocities.

## Appendix G: Additional Comparison Between LIME and LVG Plots.

In this appendix the CO ladders of LIME and LVG are provided under the initial comparison conditions. The logarithmic scale tends to mask the differences. Then the  $J = 5 - 4$  and the  $J = 10 - 9$  CO emission is displayed as computed by LIME and LVG for the C-type shock model with  $r_{op} = 3.0$ ,  $v_s = 10 \text{ km s}^{-1}$ ,  $n_H = 10^4 \text{ cm}^{-3}$  and  $b = 1.0$ . The Doppler  $b$ -parameter was set to  $0 \text{ km s}^{-1}$  and the dust was not taken into account in LIME. Both LIME and LVG perform computations with the same CO data file by Neufeld (in prep.) in this “regular” run test. Also the CO ladders are provided. The same set of figures is then given for the computations under the assumption of a collision dominated medium.

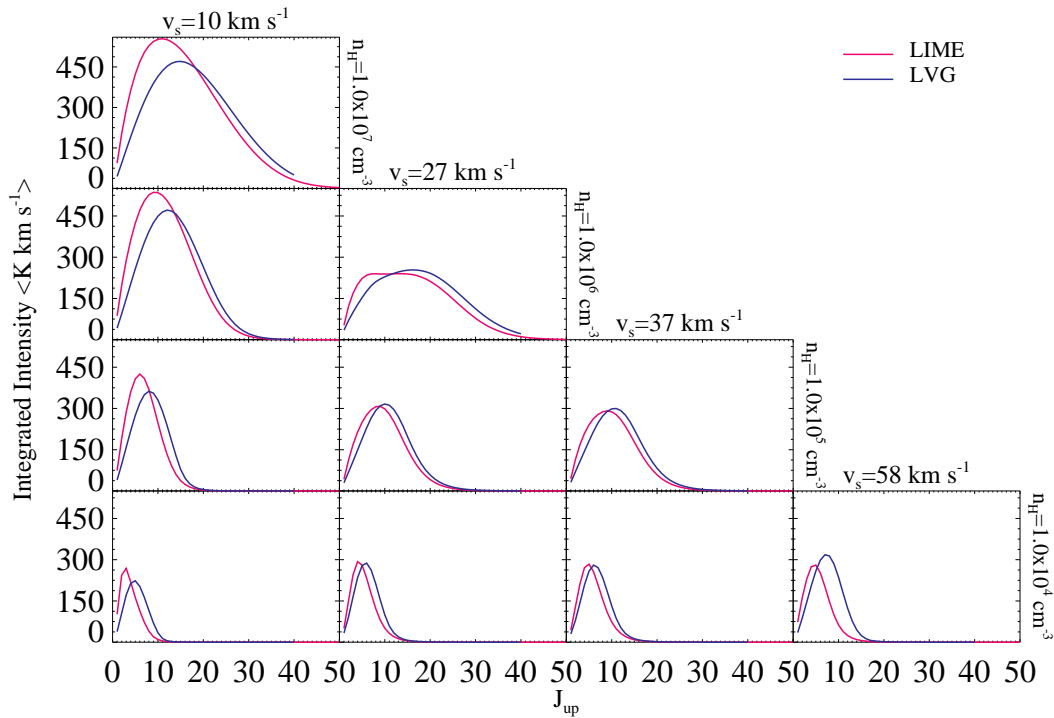


**Fig. G.1.** The CO ladder for ten representative shock models as computed by LIME and LVG.

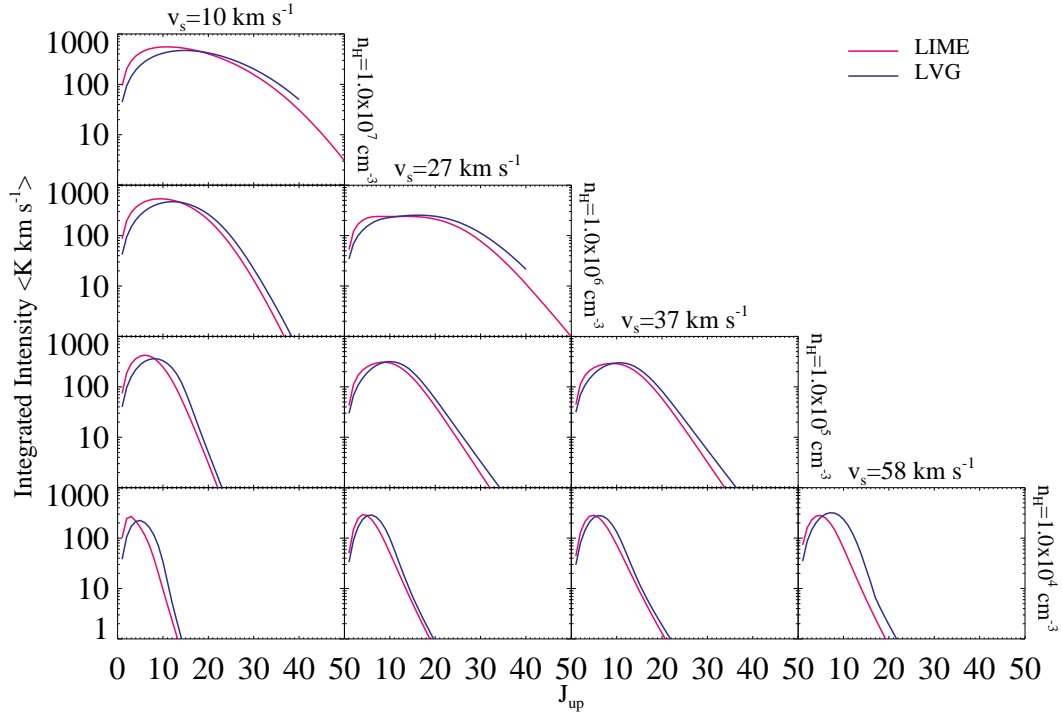


**Fig. G.2.** The CO ladder for ten representative shock models with a logarithmic scale along the ordinate as computed by LIME and LVG.

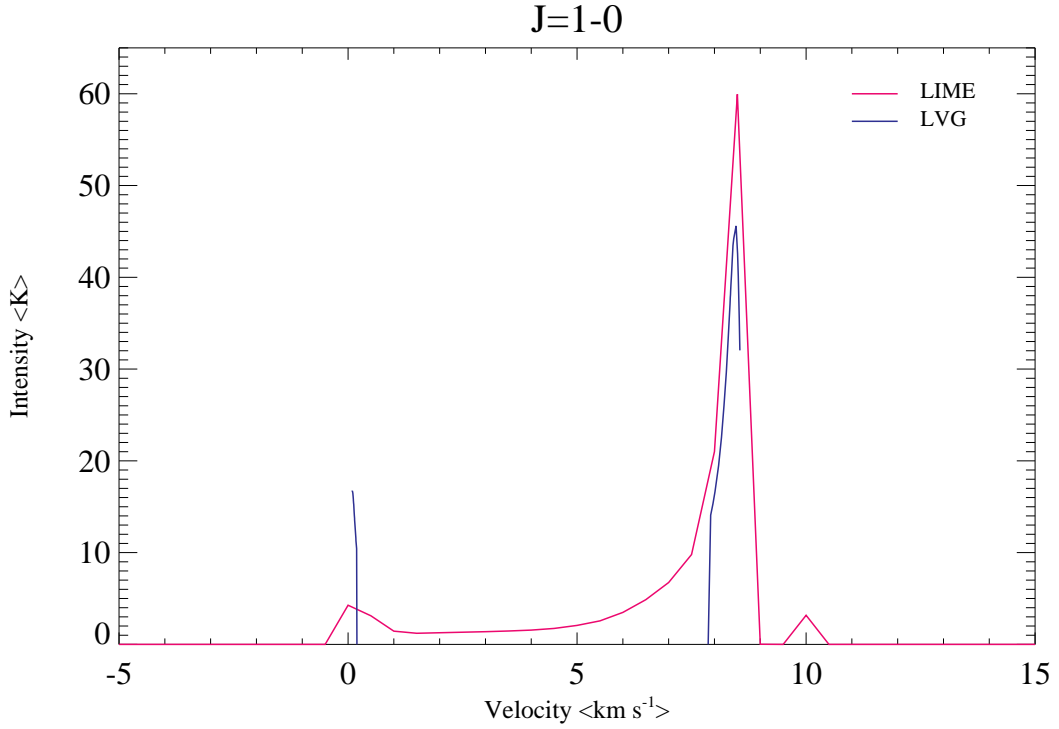


**Fig. G.3.** The  $J = 1 - 0$  line profile for the C-type shock model with  $r_{op} = 3.0$ ,  $v_s = 10 \text{ km s}^{-1}$ ,  $n_H = 10^4 \text{ cm}^{-3}$  and  $b = 1.0$  as computed by LIME and LVG (with no dust and Doppler taken into account, and with both codes operating on the same 80 transition CO molecular data file by Neufeld (in prep.)).

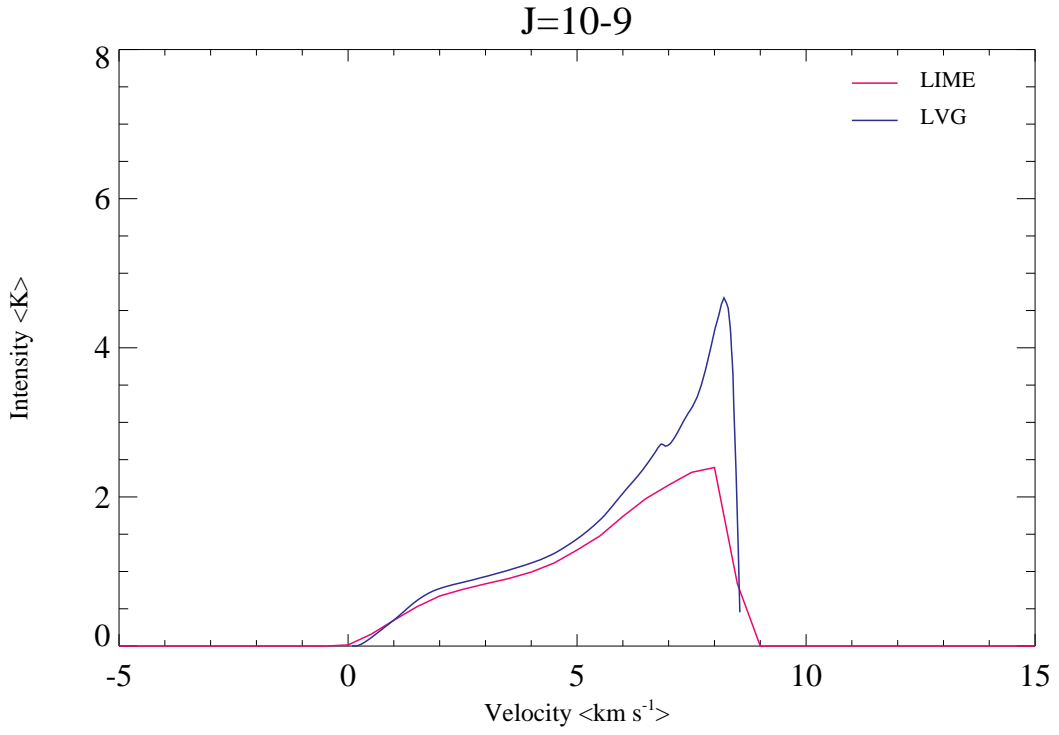


**Fig. G.4.** The  $J = 10 - 9$  line profile for the C-type shock model with  $r_{op} = 3.0$ ,  $v_s = 10 \text{ km s}^{-1}$ ,  $n_H = 10^4 \text{ cm}^{-3}$  and  $b = 1.0$  as computed by LIME and LVG (with no dust and Doppler taken into account, and with both codes operating on the same 80 transition CO molecular data file by Neufeld (in prep.)).

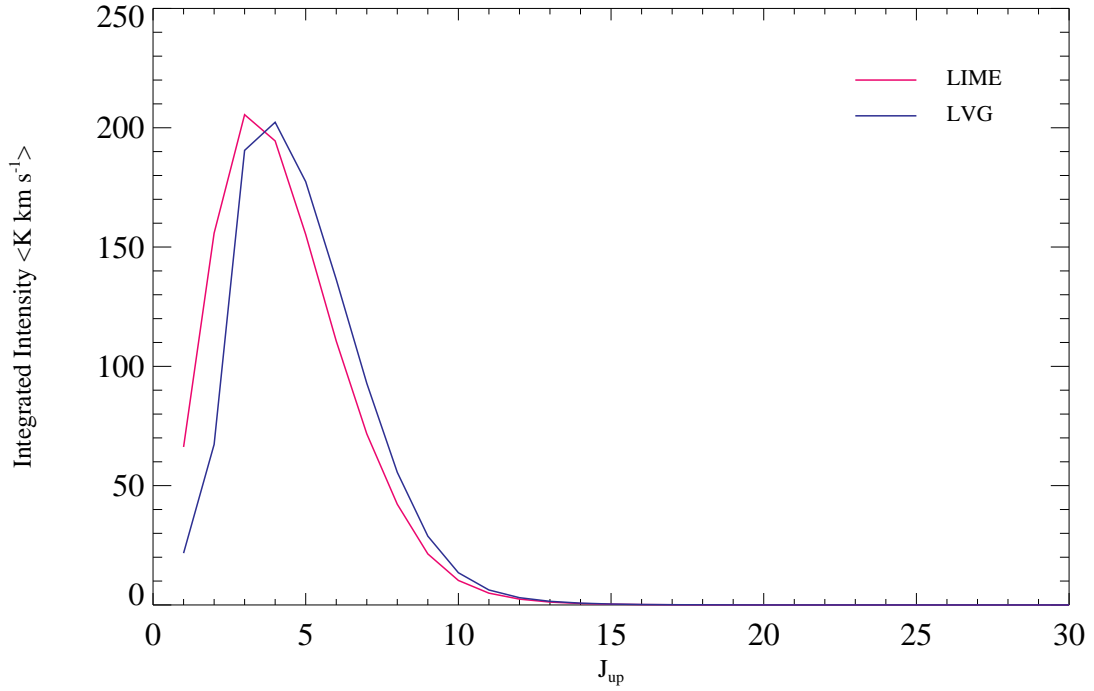


**Fig. G.5.** The CO ladder for the C-type shock model with  $r_{op} = 3.0$ ,  $v_s = 10 \text{ km s}^{-1}$ ,  $n_H = 10^4 \text{ cm}^{-3}$  and  $b = 1.0$  as computed by LIME and LVG (with no dust and Doppler taken into account, and with both codes operating on the same 80 transition CO molecular data file by Neufeld (in prep.)).

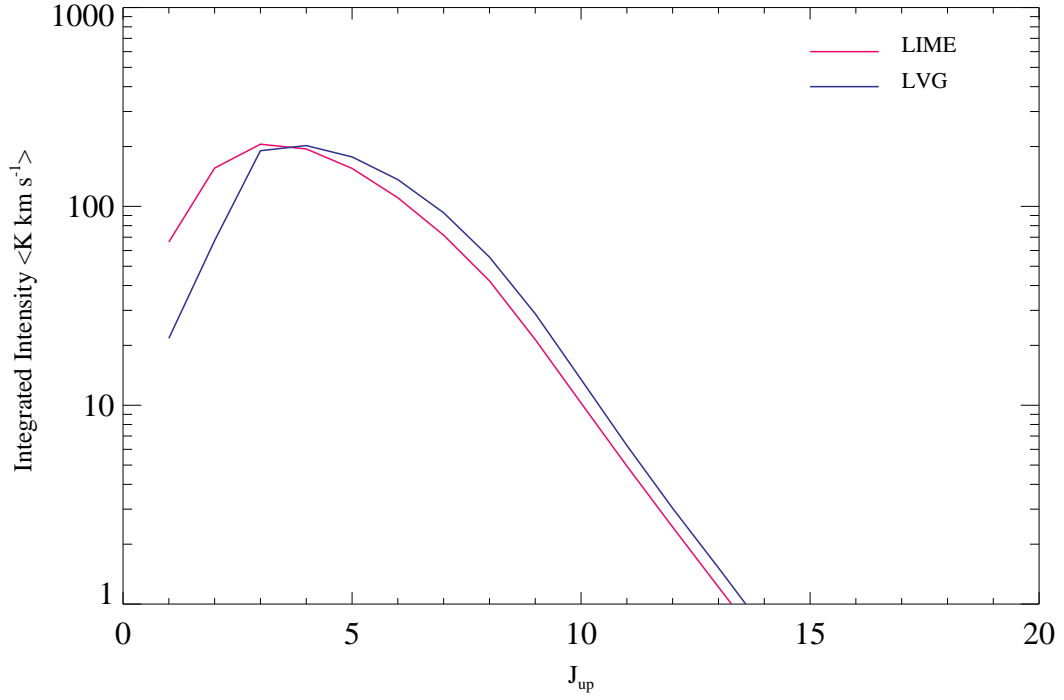


**Fig. G.6.** The CO ladder the C-type shock model with  $r_{op} = 3.0$ ,  $v_s = 10 \text{ km s}^{-1}$ ,  $n_H = 10^4 \text{ cm}^{-3}$  and  $b = 1.0$  as computed by LIME and LVG (with no dust and Doppler taken into account, and with both codes operating on the same 80 transition CO molecular data file by Neufeld (in prep.)) with a logarithmic scale along the ordinate.

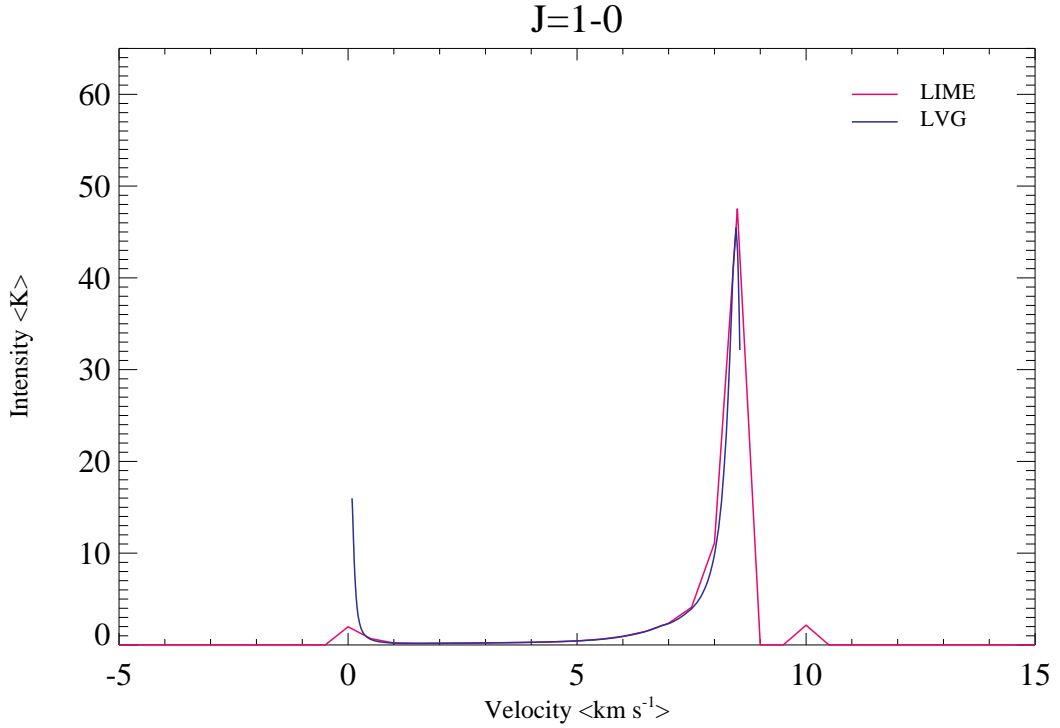


**Fig. G.7.** The  $J = 1 - 0$  line profile for the C-type shock model with  $r_{op} = 3.0$ ,  $v_s = 10 \text{ km s}^{-1}$ ,  $n_H = 10^4 \text{ cm}^{-3}$  and  $b = 1.0$  as computed by LIME and LVG (with no dust and Doppler taken into account, and with both codes operating on the same 80 transition CO molecular data file by Neufeld (in prep.)) under the assumption of a collision dominated medium.

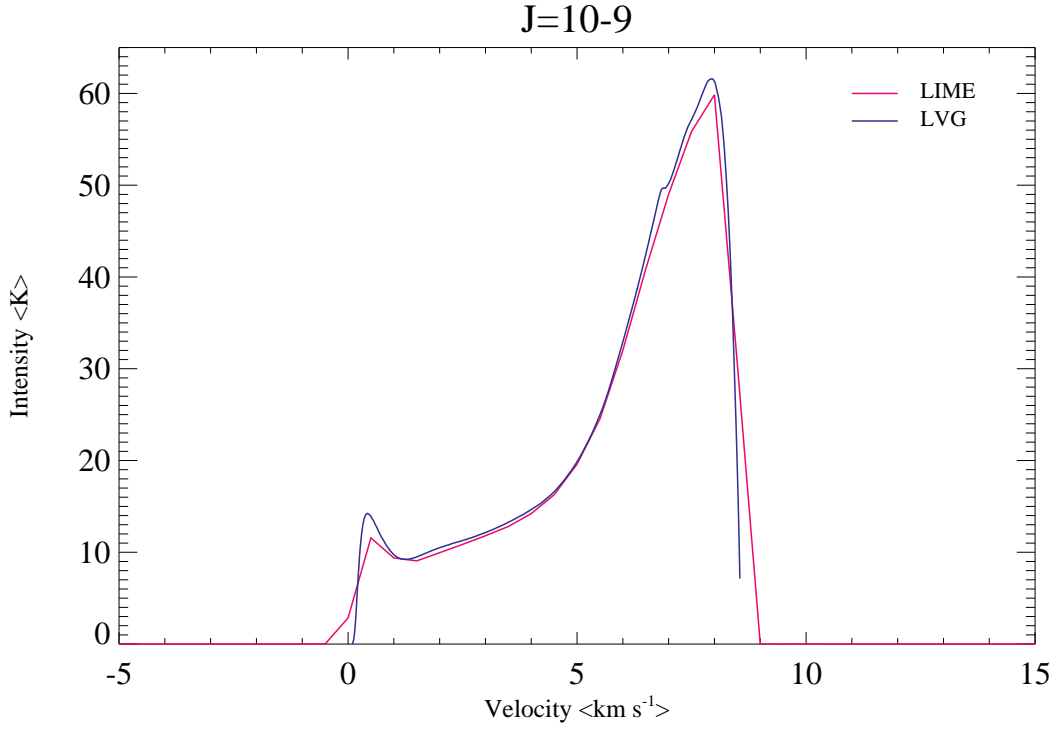


**Fig. G.8.** The  $J = 10 - 9$  line profile for the C-type shock model with  $r_{op} = 3.0$ ,  $v_s = 10 \text{ km s}^{-1}$ ,  $n_H = 10^4 \text{ cm}^{-3}$  and  $b = 1.0$  as computed by LIME and LVG (with no dust and Doppler taken into account, and with both codes operating on the same 80 transition CO molecular data file by Neufeld (in prep.)) under the assumption of a collision dominated medium.

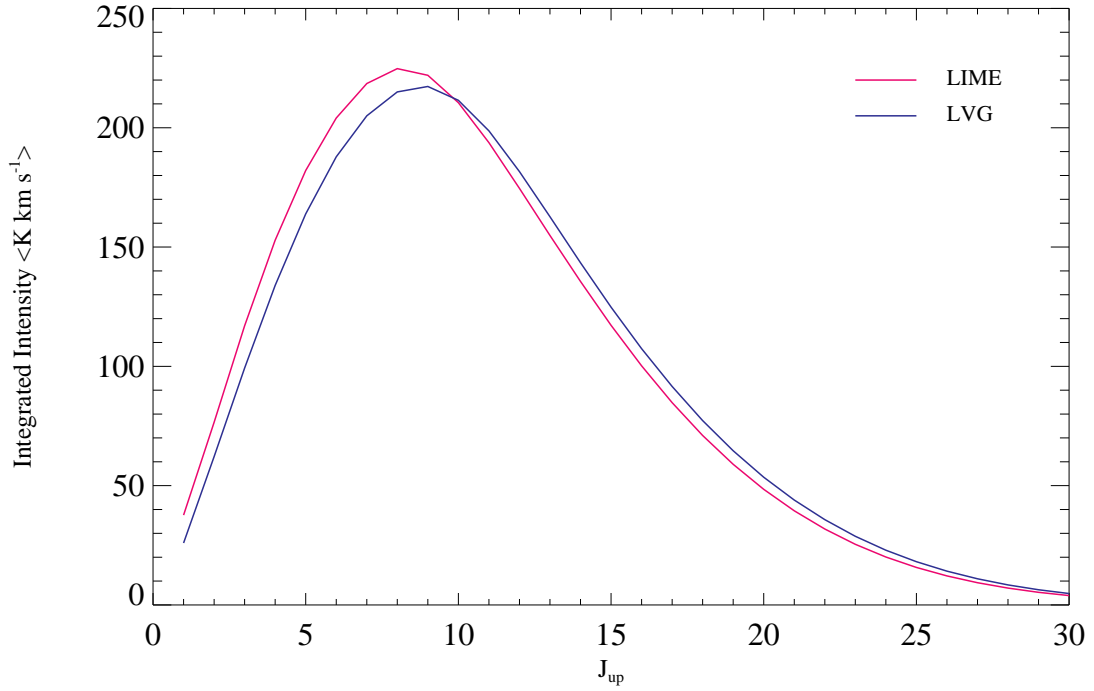


**Fig. G.9.** The CO ladder for the C-type shock model with  $r_{op} = 3.0$ ,  $v_s = 10 \text{ km s}^{-1}$ ,  $n_H = 10^4 \text{ cm}^{-3}$  and  $b = 1.0$  as computed by LIME and LVG (with no dust and Doppler taken into account, and with both codes operating on the same 80 transition CO molecular data file by Neufeld (in prep.)) under the assumption of a collision dominated medium.



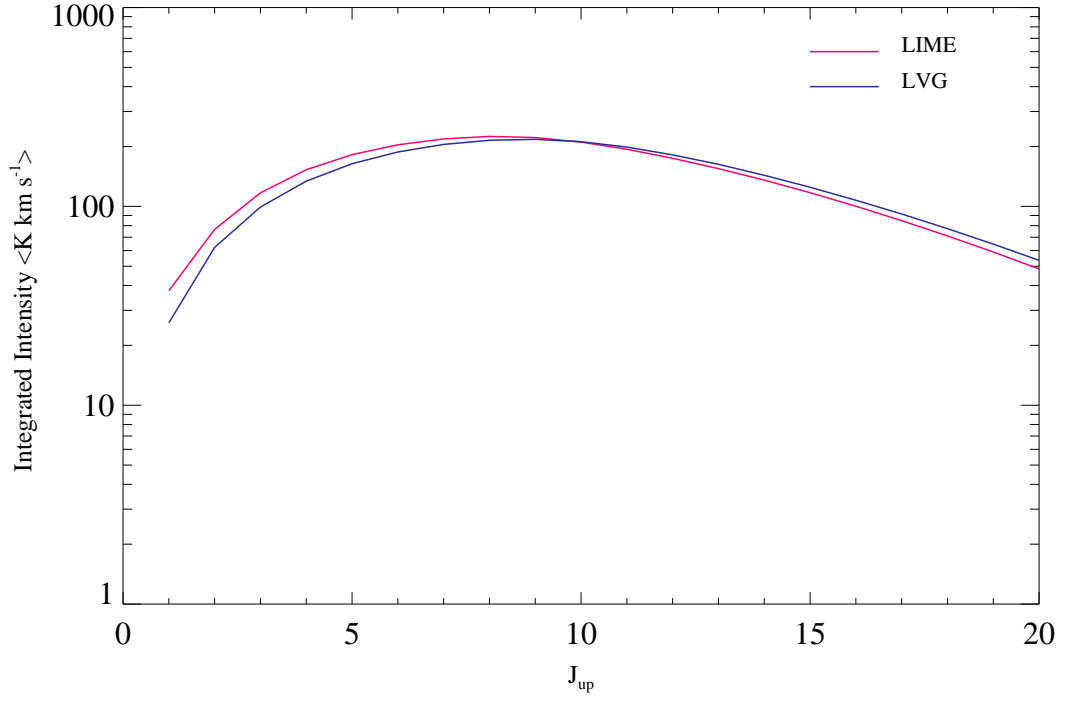


**Fig. G.10.** The CO ladder the C-type shock model with  $r_{op} = 3.0$ ,  $v_s = 10 \text{ km s}^{-1}$ ,  $n_H = 10^4 \text{ cm}^{-3}$  and  $b = 1.0$  as computed by LIME and LVG (with no dust and Doppler taken into account, and with both codes operating on the same 80 transition CO molecular data file by Neufeld (in prep.)) with a logarithmic scale along the ordinate under the assumption of a collision dominated medium.